THZ CHIP-TO-CHIP COMMUNICATION: CHANNEL CHARACTERIZATION AND RFID TAG DESIGN

A Dissertation
Presented to
The Academic Faculty

by

Chia-Lin Cheng

In Partial Fulfillment
of the Requirements for the Degree
Doctor of Philosophy in the
School of Electrical and Computer Engineering

Georgia Institute of Technology

May 2020

THZ CHIP-TO-CHIP COMMUNICATION: CHANNEL CHARACTERIZATION AND RFID TAG DESIGN

Approved by:

Dr. Alenka Zajić, Advisor
School of Electrical and Computer Engineering
Georgia Institute of Technology

Dr. Milos Prvulovic, Co-Advisor
School of Computer Science
Georgia Institute of Technology

Dr. Andrew F. Peterson
School of Electrical and Computer Engineering
Georgia Institute of Technology

Dr. Gregory D. Durgin
School of Electrical and Computer Engineering
Georgia Institute of Technology

Dr. Gordon L. Stüber
School of Electrical and Computer Engineering
Georgia Institute of Technology

Dr. Alexandros Daglis
School of Computer Science
Georgia Institute of Technology

Date Approved: March 13, 2020

To

my family and friends.

ACKNOWLEDGEMENTS

I have been very fortunate to have Prof. Alenka Zajić as my thesis advisor. I would like to express my deepest gratitude for her guidance and generous support. She has taught me the way to conduct, publish, and present research, and has set a role model for me as a leader. She has shown me that solving hard problems with patience and persistence can make great impacts. With all her guidance, I have had an enjoyable and fun journey pursuing my Ph.D. degree at Georgia Tech.

I would like to thank my thesis co-advisor, Prof. Milos Prvulovic for his guidance on my Ph.D. research. He has been very supportive and patient teaching me and explaining the concepts that I was not familiar with. It has been fun and enjoyable to explore the unknown with him.

I would also like to thank Prof. Andrew Peterson for taking the time to serve as the chair of my Ph.D. proposal examination, and thank Prof. Gregory Durgin for taking the time to serve as my Ph.D. thesis reading committee. I have been grateful to the rest of my committee members, Prof. Gordon Stüber, and Prof. Alexandros Daglis for being generous in sharing their expertise and suggestions, which have helped further improve my research.

I have had great lab mates at the Electromagnetic Measurements in Communications and Computing (EMC^2) Lab; Kevin, Fu, Baki, Haider, Seun, Sunjae, Elvan, Frank, Pavel, Sinan, Moumita, Nader, Alireza, Prateek, Ioannis, Mine, Erik, Andrew, Monjur, and Robert. It has been enjoyable to discuss ideas and collaborate with my lab mates, from whom I have learned a lot. I would like to thank them for keeping me company on this journey to the Ph.D.

Finally, I would like to thank my family for being so supportive over the years. I would not have achieved this without their unconditional love and support.

TABLE OF CONTENTS

LIST OF TABLES

LIST OF FIGURES

SUMMARY

Wireless data traffic is increasing exponentially due to the change in the way today's society creates, shares, and consumes information. Following this trend, the required data rates are expected to approach Terabit-per-second (Tbps) range within the next five to ten years. The carrier frequency used for wireless communication has been continuously increased to meet the ever-growing system requirements for high data rates. To achieve the required Tbps data rates, THz frequency bands need to be explored.

In this thesis, we address two problems that need to be solved to enable Tbps data rates: 1) characterize and model wireless channels in data centers and 2) design THz antenna-less RFID tags that can further reduce the device size by not using antennas and have potential to attain ultra high data rates.

Existing wired data centers are facing challenges such as increased assembly cost, maintenance cost, operating cost, service time, and decreased cooling efficiency due to the usage of cables. On the other hand, existing RFID technologies have limited data rates due to limited bandwidth and have inflexible form factor since the device size is mainly dominated by the antennas.

To successfully enable the proposed applications for THz chip-to-chip communication, this thesis focuses on the channel characterization of THz wireless data centers and the development of THz antenna-less RFID tags. The first objective is to characterize channel properties and develop statistical channel models for THz propagation in a data center environment. Various propagation scenarios are investigated, including line-of-sight (LoS) link, non-LoS (NLoS) link using existing materials in a data center to redirect the beam, and obstructed-LoS (OLoS), -NLoS (ONLoS) links with common objects in data centers (cables and server racks' mesh doors) serving as obstruction. We analyze propagation parameters such as pathloss, power delay profile (PDP), root-mean-squared (RMS) delay spread, and shadowing gain in the aforementioned scenarios. Multiple-Input Multiple-

Output (MIMO) measurements are conducted using virtual MIMO arrays. A statistical cluster-based channel model for THz propagation in a data center environment is proposed and validated with measured data. The second objective is to develop a circuit impedance model to explain the antenna-less backscattering mechanism, propose a propagation model, and demonstrate the applications of static and dynamic IDs for the THz antenna-less RFID tags. A circuit impedance model is developed to describe the relation between the total input impedance and the logic resources of the digital circuits. Furthermore, a propagation model for the antenna-less RFID tags is developed for the assessment of link budget and validated with measurements. Several applications are implemented to demonstrate that the antenna-less RFID tag has very flexible carrier frequency selection (5.8 GHz–300 GHz) and bit configuration, where the static ID can transmit up to 36 bits simultaneously with up to 68.7 billion (2^{36}) combinations of unique IDs, and the dynamic ID can achieve a data rate of 100 kbits/sec with a bit error rate (BER) of 0.00000183 (10^{-6}).

Our work provides other researchers guidelines on design approach and system planning for THz wireless data centers and THz antenna-less RFID tags.

CHAPTER 1
INTRODUCTION

1.1 Motivation

The ever-growing demand on the capacity of wireless communication indicates that data rates will reach Terabit-per-second (Tbps) in the coming years. One solution is to improve the spectrum efficiency by using advanced digital modulation schemes, such as Orthogonal Frequency Domain Multiplexing (OFDM) as well as Multiple-Input-Multiple-Output (MIMO) radio technology. However, these techniques will require higher link linearity, larger link dynamic range, and more expensive and complex transceiver architectures. Furthermore, the scarcity of the available bandwidth imposes an upper bound on the achievable data rate according to the Shannon's channel capacity theorem [1]. Alternatively, to overcome the channel congestion in the long run, there have been increasing interests in extending the carrier frequency for ultra-fast wireless communication into higher frequency bands. Terahertz (THz) bands (300 GHz–10 THz) provide abundant unregulated bandwidth to realize Tbps high speed links.

This thesis addresses two problems needed to be solved to enable Tbps data rates: 1) characterize and model wireless channels in data centers and 2) design THz antenna-less RFID tags that can further reduce the device size by not using antennas and have potential to attain ultra high data rates.

Existing wired data centers are facing challenges such as increased assembly cost, maintenance cost, operating cost, service time, and decreased cooling efficiency due to the usage of cables. On the other hand, existing RFID technologies have limited data rates due to limited bandwidth and have inflexible form factor since the device size is mainly dominated by the antennas.

Along with the unprecedented opportunities, THz communication brings unique challenges that require to reconsider traditional propagation mechanisms. The extremely wideband and directional nature of the THz links lead to substantially new propagation and interference compositions in wireless systems with multiple reflected, diffracted, and scattered beams that cause complex received signal waveform. In addition, a challenge that still tampers the feasibility of THz communication is the attenuation of the THz signal with distance. Therefore, it is of critical importance to characterize channels' radio propagation properties at THz frequencies. To enable successful designs of the proposed solutions for THz chip-to-chip communication, this thesis focuses on channel characterization and modeling for THz wireless data centers and the design and propagation modeling of THz antenna-less RFID tags.

Wireless links in data centers can alleviate cable management, maintenance, and packaging constraints, as well as reduce latency by providing direct communication between multiple chips [2, 3, 4, 5, 6, 7, 8, 9, 10, 11, 12, 13, 14]. The data center environment is unique in its densely packed compartmentalized layout with rows of metallic server racks aligned in parallel and high performance computing servers with metal enclosures vertically stacked up in each rack. Exposed cable clusters, e.g., power cables, exist between the server racks and server machines [5, 15]. This constitutes a unique propagation channel, whose properties need to be explored. However, a comprehensive characterization and modeling of THz propagation channels, which includes various obstructions in a data center is not available. The first objective of this thesis is to characterize channel properties and develop statistical channel models for THz propagation in a data center environment.

The proposed THz antenna-less RFID tag is based on a new backscatter radio generated from switching of transistors in digital electronics, which does not need to use antennas or any RF front-end circuits thereby further reducing the device's form factor. In addition, the THz antenna-less RFID tag can be interrogated at a wide range of carrier frequencies across sub-6 GHz, millimeter-wave (mm-wave), and THz bands, which provides flexible

configurations and abundant available bandwidth for ultra high data rate applications. Various applications can be implemented on the THz antenna-less RFID tag, including static and dynamic IDs. The second objective is to develop a circuit impedance model to explain the antenna-less backscatter mechanism, propose a propagation model for the antenna-less backscatter communication, and demonstrate a variety of applications of the THz antenna-less RFID tags.

1.2 Characterization and Modeling of Propagation Phenomena Relevant for 300 GHz Wireless Data Center Links

In traditional data centers, information exchange between servers mainly relies on wires and optical fiber cables. The use of the wires and cables increases the cost of assembly, maintenance, and operation, and service time [5, 10, 6]. Wired topologies impact the scalability and flexibility of the overall data center [12, 8]. Furthermore, cable bundles between server racks can block the cooling airflow and lead to inefficient cooling [16].

THz wireless communication has several key advantages that would alleviate some of the aforementioned problems and facilitate wireless data centers: 1) sufficient available bandwidth [14, 13]—an IEEE 802.15.3d [17] standard for THz communication proposes a data rate up to 100 Gbit/s at 252–325 GHz using eight different bandwidths between 2.16 GHz and 69.12 GHz; 2) smaller antennas and antenna spacing at THz frequencies enables miniaturization of phased arrays for beamsteering to provide more multiple-input multiple-output (MIMO) channels within the same array aperture to reach Tbits/s data rates; 3) directionality of propagation at THz frequencies results in reduced interference and increased isolation [18, 19]; 4) data centers provide controllable environmental conditions such as a low moisture atmosphere and limited nodes mobility, which can be favorable for THz wave propagation.

The development of THz wireless system in data centers would require the characterization and modeling of the propagation channel in which such a device will operate. To

understand the THz propagation channel in a data center environment, we first conduct channel sounding in a mock-up data center model as a starting point, which allows for more flexibility exploring a variety of potential propagation scenarios, including rack-to-rack (R2R) link with optical lenses that enable long-range communication across multiple racks, and blade-to-blade (B2B) vertical link that provides short-range communication between servers within the same rack. Besides the line-of-sight (LoS) link, we explore the impact of obstructions such as cables, metal cabinets, and mesh structures on THz propagation, as well as feasibility of using existing metal objects as reflectors for non-LoS (NLoS) links. Furthermore, we have observed that the turbulence from cooling airflow can cause cables to vibrate, and thus lead to Doppler shift in the THz bands. Regarding this interesting observation, a two-dimensional (2-D) geometrical propagation model that includes moving scatterers is developed to model the Doppler power spectrum (DPS).

1.3 Characterization of 300 GHz Propagation in a Data Center Environment

The data center environment is unique in its densely packed compartmentalized layout with rows of metallic server racks aligned in parallel and high performance computing servers with metal enclosures vertically stacked up in each rack. Exposed cable clusters, e.g., power cables, data cables, and auxiliary cables, exist between the server racks and server machines [5, 15]. This constitutes a unique propagation channel, whose properties need to be explored.

Several publications in the literature have explored the use of THz wireless links in data centers to achieve dynamic operation and higher reconfigurability [13, 20, 21, 14, 22, 23]. Moreover, THz frequencies promise a higher data rate with its large bandwidth and lower interference (due to the directional antennas) [24, 25, 26, 27, 28, 29]. Simulation-based work in [14, 22] presented a stochastic channel model along with its simulation results for a THz wireless data center. However, measurement results were not provided. Measurement-based work in [23] presented a THz measurement campaign conducted in a data center.

Results showed that path attenuation is comparable to Friis theoretical values and that THz wireless communication in a data center is possible. However, the measurement campaign did not investigate the propagation scenario with exposed cables serving as obstruction, which have been observed in some of the existing data centers [5, 15].

As seen from the above literature survey, there is a lack of a comprehensive characterization of THz propagation channels that includes various obstructions in a data center. In response, this thesis presents details from the THz channel measurement campaign conducted in a data center environment with consideration for propagation scenarios including LoS link, NLoS link using existing materials in a data center to redirect the beam, and obstructed-LoS (OLoS)/obstructed-NLoS (ONLoS) links with common objects in data centers (cables and server racks' mesh doors) serving as obstruction.

1.4 Cluster-Based Modeling for 300 GHz Propagation in a Data Center Environment

In the previous measurement campaign conducted in a data center, we have observed that multipath components (MPCs) naturally group into clusters in some of the measurements conducted. Therefore, a cluster-based propagation model for THz propagation in a data center environment is proposed in such scenarios. Cluster-based models have been widely used for indoor propagation channels across a wide range of frequency spectra, from microwave (cellular), ultra-wideband (UWB), mm-wave, up to THz bands [30, 31, 32, 33, 34, 35, 36, 37, 38, 39]. Clustering in the delay domain directly affects the delay spread, which is important in determining the need for employing channel protection techniques, e.g., channel equalization, channel coding, or channel diversity to overcome the dispersive effects of multipaths [40]. Regardless of such wide applicability and the aforementioned importance, no cluster-based model has been developed for THz propagation channels in data center environments. Our proposed clustering model is validated with measured data collected from Chapter 1.3, and the corresponding inter- and intra-cluster parameters and

their relevant statistics are presented.

1.5 Impedance Estimation of Switching Transistors in Digital Electronics for THz Antenna-Less RFID Tags

Traditional backscatter communication refers to a radio channel where a reader sends a continuous carrier wave (CW) signal to a tag and retrieves information from a modulated wave scattered back from the tag. During backscatter operation, the input impedance of a tag antenna is intentionally mismatched by two-state RF loads (Z_0 and Z_1) to vary the tag's reflection coefficient and radar cross section (RCS) and to modulate the incoming CW [41, 42]. Mm-wave RFIDs (MMID) [43, 44, 45, 46, 47] and THz RFIDs [48, 49, 50] have been developed due to the wider available bandwidth at higher frequencies that allows high data rates and superior spatial resolution for short-range communication and localization. However, the form factor of existing RFID tags has limited room for further miniaturization since they all need to use antennas, which are the largest parts of the tag [46].

To further miniaturize the backscatter communication systems and enhance the coding capacity, a new backscatter architecture that can operate without antennas and is compatible with a wide range of interrogating carrier frequencies is needed. We introduce the THz antenna-less RFID tag based on a new backscatter radio generated from switching of transistors in digital electronics, which does not need to use antennas or any RF front-end circuits thereby further reducing the device's form factor. Moreover, the proposed antenna-less RFID tags are compatible with a wide range of interrogating carrier frequencies from sub-6 GHz up to 300 GHz, and can be implemented on existing electronics without additional cost. Since this is a new type of backscatter communication, the backscatter mechanism needs to be understood and modeled. Therefore, we develop a circuit impedance model to explain the modulation mechanism of the new backscatter radio and to describe the relation between the total input impedance and the logic resources of the digital circuits.

1.6 Propagation Model for Antenna-Less Backscatter Radio

A complete propagation model for traditional backscatter radio systems is required to assess link budget, which is important for evaluating the feasibility and reliability of a wireless link, and has been demonstrated in [42]. However, the existing backscatter propagation model does not provide the estimation of the modulation loss resulting from the switching activity of the digital electronics, and thus cannot be directly applied to the proposed antenna-less backscatter radio link. To address this need, we introduce a new propagation model for the antenna-less RFID tag. The proposed propagation model consists of modulation loss factor (due to the switching of transistors) that is derived from the proposed circuit impedance model, and can be used to estimate link budget for the antenna-less backscatter radio. The proposed propagation model is validated with measured data.

1.7 Static and Dynamic RFIDs at 5.8 GHz, 17 GHz, 26.5 GHz, and 300 GHz

The design methodology of the static and dynamic IDs has been proposed, and the applications of the proposed static and dynamic multi-bit IDs across various interrogating frequencies have been demonstrated. The "static" term means that the designed bit pattern does not change over time, information stored on the tag depends on total number of bits. In contrast, the "dynamic" term means the designed bit pattern changes over time. Compared to the static ID, here an individual bits are turned on and off over time at a switching frequency (f_s) to transmit information. As a result, information stored on the tag is not limited by total number of bits but depends on f_s and total transmitting time. To demonstrate that the proposed RFID tag is compatible with a wide range of carrier frequencies, we have tested the following interrogating frequencies: 1) 5.8 GHz, a frequency typically used for RFID communications, 2) 17.46 GHz, a frequency that we have identified to have the highest signal-to-noise ratio (SNR), 3) 26.5 GHz, a frequency that can be used for 5G wireless communications, and 4) 300 GHz, a frequency that belongs to the IEEE 802.15.3d [17]

standard for THz communication. The performance of the proposed antenna-less RFID tags is comparable to state-of-the art RFID tags.

1.8 Research Contributions

- Characterization of propagation phenomena relevant for 300 GHz wireless data center links [51, 52, 53, 28, 54].
- Development of 2-D geometrical propagation model for Doppler power spectrum (DPS) at 300 GHz [55].
- Characterization of 300 GHz propagation in a data center environment [56, 55].
- Development of cluster-based model for 300 GHz propagation in a data center environment [56].
- Impedance estimation of switching transistors in digital electronics for THz antenna-less RFID tags [57].
- Development of propagation model for antenna-less backscatter radio.
- Development of static and dynamic IDs for antenna-less RFID tags at 5.8 GHz, 17 GHz, 26.5 GHz, and 300 GHz [57, 58].

1.9 Thesis Outline

The remainder of this thesis is organized as follows: Chapter 2 reviews the important concepts of propagation modeling and provides a brief background of wireless data centers and backscatter communication. Chapter 3 presents the results of measurements of 300 GHz R2R/B2B LoS and NLoS scenarios in a mock-up model of data center, and describes our two-dimensional (2-D) geometrical propagation model for Doppler power spectrum (DPS) at 300 GHz. Chapter 4 presents the results of THz channel measurement campaign conducted in a data center environment with consideration for propagation scenarios including

LoS link, NLoS link using existing materials in a data center to redirect the beam, and OLoS/ONLoS links with common objects in data centers (cables and server racks' mesh doors) serving as obstruction. Chapter 5 describes our cluster-based propagation model for THz propagation in a data center environment along with experimental validation with the measured data collected from Chapter 4. Chapter 6 describes our circuit impedance model that explains the modulation mechanism of the antenna-less backscatter radio. Chapter 7 describes our propagation model that can be used to estimate link budget for the antenna-less backscatter radio. Chapter 8 presents the design methodology and the measurement results of the proposed static and dynamic IDs at 5.8 GHz, 17 GHz, 26.5 GHz, and 300 GHz. Finally, Chapter 9 concludes the thesis by summarizing our research contributions and addressing future research directions.

CHAPTER 2
BACKGROUND

Successful designs of THz wireless data centers and THz antenna-less RFID tags for THz chip-to-chip communication require a detailed understanding of propagation properties at THz frequencies and existing development of wireless data centers and backscatter communication. In this chapter, we briefly review important concepts of wireless channel characterization and modeling.

2.1 Channel Characterization

One of the main objectives in channel characterization and modeling is to estimate the variation of the received signal strength over time. Unstable received power, either too weak or too strong, may lead to communication failure. Fading describes the variation of the received signal strength over time caused by changes in the transmission medium or path. Fading can be classified into large scale fading and small scale fading. Large scale fading, such as pathloss and shadow fading (shadowing), are dominant when the changes of distance between the transmitter (Tx) and the receiver (Rx) are greater than several tens of the carrier wavelength. Large scale fading is dependent on location with respect to obstacles and is crucial in predicting the cell coverage area and the likelihood of outage. On the contrary, small scale fading is caused by multipath propagation and movement within small distances. This effect plays an important role in determining link level performance in terms of bit error rates, average fade duration, etc.

2.1.1 Pathloss and Shadowing

Pathloss is the attenuation in the transmitted signal as it propagates from the Tx to Rx. This attenuation may be caused by effects such as free-space loss, reflection, diffraction, scatter-

ing, and absorption. The simplest pathloss model assumes line-of-sight (LoS) link between the Tx and Rx and propagation in free space. Under these assumptions, the received signal power is given as [59]

$$P_R \;=\; P_T \cdot G_T \cdot G_R \cdot \left(\frac{\lambda}{4\pi d}\right)^2, \tag{1}$$

where P_T is the transmitted power, G_T and G_R are the transmit and receive antenna gains, respectively, λ is the carrier wavelength, and d is the distance between the Tx and Rx. In reality, the assumptions of LoS link and free space propagation between the Tx and Rx do not always hold. Therefore, several different models such as the Okumura-Hata, Ikegami, Lee, etc., have been proposed to model pathloss in different propagation environments such as urban, rural, and indoor areas [59]. In this proposed work, we model the pathloss by the single-frequency floating-intercept (FI, alpha-beta, or the 3rd Generation Partnership Project 3GPP) model due to better susceptibility to measurement error [28]. The FI pathloss model is given as follows [59]:

$$PL^{FI}(d) = \alpha + 10 \cdot \beta \cdot \log_{10}\left(\frac{d}{d_0}\right) + X_\sigma^{\mathrm{FI}}, d \geq d_0, \tag{2}$$

where $PL^{FI}(d)$ is the pathloss in dB as a function of d, α is a floating intercept in dB that represents the free-space pathloss at the reference distance d_0. According to [1], d_0 should always be in the far-field of the antenna so that the near-field effects do not alter the reference pathloss. Coefficient β is the pathloss exponent (PLE) that characterizes the pathloss dependency on d. The PLE in free space is 2, whereas for urban area and waveguide-like environment, generally the PLEs are in the range of 2.7–3.5 and less than 2, respectively. X_σ^{FI} is the large-scale shadowing that can be modeled as a zero-mean Gaussian distributed random variable with standard deviation σ in dB. Shadowing results from random variations of the received power at a given distance caused by the presence of obstacles such as buildings and trees given an outdoor environment. These fluctuations

of the received power are experienced in the received local mean powers, that is, short-term averages are performed to remove fluctuations due to small scale fading. To estimate the pathloss model parameters α, β, and σ, the least-squares linear fitting is performed through the measured pathloss data sets such that the root-mean-square (RMS) deviation from the mean pathloss is minimized. Detailed descriptions of different pathloss models can be found in [60, 59, 28]. Experimental results show that shadowing can be modeled as a log-normal random variable given by [59]

$$f_{\Omega_p}(x) = \frac{10}{x\sigma_\Omega\sqrt{2\pi}\ln 10}\ \exp\left[-\frac{(10\log_{10}x - \mu_{\Omega_p(\mathrm{dBm})})^2}{2\sigma_\Omega^2}\right], \tag{3}$$

where Ω_p denotes the mean squared envelope level, μ_{Ω_p} is the area mean expressed in dBm and σ_Ω is the standard deviation of the shadowing.

2.1.2 Multipath Fading and Delay Spread

The presence of local scattering objects often obstructs a direct wave path between the Tx and Rx, which leads to a non-line-of-sight (NLoS) propagation path between the Tx and Rx. As a result, the waves propagate via reflection, diffraction, and scattering and arrive at the Rx from different directions with different delays. A phenomenon of multiple waves combining vectorially at the Rx antenna to produce a complex received signal is called multipath fading or small scale fading. A Rayleigh distributed multipath fading describes the fading with diffuse wave components in NLoS propagation caused by the scatterers in the environment. In contrast, a Rician distributed multipath fading represents the fading where a LoS or a dominant specular component also arrives at the Rx. The channel with multipath fading can be modeled by a linear time-variant filter that has the complex low-pass impulse response [59]

$$h(t,\tau) = \sum_{l=1}^{L} g_l(t)\cdot\delta(\tau-\tau_l), \tag{4}$$

where L is the total number of resolvable multipath components, and $g_l(t)$ is the time-varying complex faded envelope associated with the l^{th} resolvable multipath component arriving with an average time delay τ_l. Each time-varying complex faded envelope $g_l(t)$ is either Rayleigh or Rician faded.

Time selectivity and frequency selectivity are two important properties of the channel impulse response. Time selectivity refers to the variation of the channel impulse response over time. This is caused by the motion of the Tx, Rx, and/or the scatterers. When viewed in the frequency domain, time selectivity appears as Doppler shifts in the transmitted signal with a broaden signal spectrum, which is also called frequency dispersion. Based on the rate with which the channel impulse response changes relative to the signal transmission rate, channels may be classified as fast fading or slow fading. Fast fading implies that the magnitude and phase of the channel impulse response change rapidly within the transmitted symbol duration, while slow fading implies that the channel impulse response is approximately constant within a symbol duration. A good measure of channel selectivity is given by the channel coherence time, or equivalently, the Doppler spread, i.e., the time duration for which the channel can be considered as approximately time-invariant. Time selectivity is not relevant in the proposed work since the Tx and Rx as well as any scatterers in the channel are stationary, i.e., the channel is time-invariant.

Frequency selectivity refers to variation of the channel impulse response over frequency. Multipath components that arrive with different time delays cause frequency selectivity. Based on the degree of frequency selectivity, channels may be classified as frequency-flat or frequency-selective. If the variation of amplitude and phase of the channel impulse response of the transmitted signal remain approximately identical over frequencies, the channel is called frequency-flat. When frequency-flat multipath fading occurs, the signal across entire frequency spectrum experiences similar amplitude changes, rising or falling over a period of time. On the other hand, when the variation of amplitude and phase of the channel impulse response changes over frequencies, the channel is

called frequency-selective. When frequency-selective multipath fading occurs, relatively deep nulls may be experienced at the Rx, and this can lead to reception problems. Simply maintaining the overall amplitude of the received signal will not overcome the effects of frequency-selective fading; implementation of equalization may be needed. Some digital signal formats, e.g., orthogonal frequency-division multiplexing (OFDM), are able to spread the data over a wide frequency bands such that only a portion of the data is lost by any nulls, which can be reconstituted using forward error correction techniques. In this way, the effects of frequency-selective multipath fading can be mitigated.

Multipath fading is characterized by the RMS delay spread (τ_{rms}), which estimates the richness of multipath. τ_{rms} is calculated by taking the square root of the second central moment of the normalized squared magnitude of the channel impulse response, i.e.,

$$\tau_{rms} = \sqrt{\frac{\sum_{k=1}^{L} |h(t,\tau_k,d)|^2 \tau_k^2}{\sum_{k=1}^{L} |h(t,\tau_k,d)|^2} - \tau_m^2}, \tag{5}$$

where L is the number of multipath components; τ_k is the excess delay of the k^{th} path relative to the first arrival; $|h(t,\tau_k,d)|^2$ is the squared magnitude of the channel impulse normalized by the sum of PDPs over delay bins; τ_m is the mean excess delay defined as

$$\tau_m = \frac{\sum_{k=1}^{L} |h(t,\tau_k,d)|^2 \tau_k}{\sum_{k=1}^{L} |h(t,\tau_k,d)|^2}. \tag{6}$$

The coherence bandwidth (B_c) represents the bandwidth over which the channel's frequency response remains approximately constant and is directly related to the τ_{rms} ($B_c \propto 1/\tau_{rms}$). In this proposed work, the B_c is estimated as [59]

$$B_c \approx \frac{1}{2\pi\tau_{rms}}. \tag{7}$$

The channel is considered frequency-flat if the transmission is narrowband with respect to the channel's B_c. Otherwise, the channel is frequency-selective.

2.2 Statistical Channel Modeling

Regarding simulation and testing of THz wireless systems, statistical channel models are ideal since they provide an efficient and generalized approach and reflect the essential properties of propagation channels [59].

2.2.1 Path Gain

In wide-band channels, the path gain (i.e., negative of pathloss) is a function of both the distance and the frequency. The frequency-dependent path gain is defined as [61]

$$G_p(d, f) = E\left[\int_{f-\Delta f/2}^{f+\Delta f/2} \left|H(\tilde{f}, d)\right|^2 d\tilde{f}\right], \tag{8}$$

where $H(f, d)$ is the channel transfer function, and Δf is chosen such that the material properties, e.g., diffraction coefficients, dielectric constants, etc. can be considered constant within that bandwidth. The total path gain is obtained by integrating over the entire bandwidth of interest.

2.2.2 Multipath Components (MPCs)

It has been observed in many channel investigations that MPCs tend to arrive in clusters. Cluster-based statistical channel models have been widely used for indoor propagation channels across a wide range of frequency spectra, from microwave (cellular), ultra-wideband (UWB), mm-wave, up to THz bands [30, 31, 32, 33, 34, 35, 36, 37, 38, 39]. Clustering in the delay domain directly affects the delay spread, which is important in determining the need for employing channel protection techniques, e.g., channel equalization, channel coding, or channel diversity to overcome the dispersive effects of MPCs [40].

The Saleh-Valenzuela (SV) model [30] is a widely-used cluster-based approach, which describes the impulse response as

$$h(t) = \sum_{l=1}^{L} \sum_{k=1}^{K_l} \beta_{k,l} \exp(j\phi_{k,l}) \delta(t - T_l - \tau_{k,l}), \tag{9}$$

where L is the number of clusters, K_l is the number of rays (MPCs) in the l^{th} cluster. $\beta_{k,l}$ is the tap weight of the k^{th} component in the l^{th} cluster. The phase $\phi_{k,l}$ is a uniformly distributed random variable in the range [0, 2π). T_l is the time of arrival of the l^{th} cluster, $\tau_{k,l}$ is the delay of the k^{th} component relative to the time T_l, and $\delta(\cdot)$ denotes the Dirac delta function. The S-V model assumes that the distributions of the cluster and ray arrival times may be described by stochastic Poisson processes, which implies that the distribution of inter-arrival time of clusters ($T_l - T_{l-1}$) can be described by an independent exponential probability density function (PDF) as follows,

$$p(T_l|T_{l-1}) \quad = \quad \Lambda \cdot e^{-\Lambda(T_l - T_{l-1})}, l > 0, \tag{10}$$

where Λ is the mean cluster arrival rate, and that the distribution of inter-arrival time of rays ($\tau_{k,l} - \tau_{(k-1),l}$) can be expressed by the following PDF,

$$p(\tau_{k,l}|\tau_{(k-1),l}) \quad = \quad \lambda \cdot e^{-\lambda(\tau_{k,l} - \tau_{(k-1),l})}, k > 0, \tag{11}$$

where λ is the mean ray arrival rate. The PDP of the S-V model in dB can be expressed as [62],

$$\mathrm{PDP}(\tau) = \sum_{l=1}^{L} \sum_{k=1}^{K_l} \left[10 \log_{10} \overline{\beta_{1,1}^2} - \overbrace{\frac{T_l}{\Gamma}(10 \log_{10} e)}^{\mathrm{P}(T_l)} - \overbrace{\frac{\tau_{k,l}}{\gamma}(10 \log_{10} e)}^{\mathrm{P}(\tau_{k,l})} \right] \cdot \delta(\tau - T_l - \tau_{k,l}), \tag{12}$$

where $\overline{\beta_{1,1}^2}$ is the local mean power of the 1^{st} ray ($k = 1$) in the 1^{st} cluster ($l = 1$). Γ and γ are the cluster power and ray power decay rates, respectively.

2.3 Wireless Data Centers

Data centers have become a critical component of cloud computing and storage. A fundamental need inside the data centers is reliable and high-speed connectivity between racks and blades [5]. Both metal wires and optical waveguides have been traditionally used in data centers, but they are increasing assembly cost, maintenance cost, operating cost, service time, and decreasing cooling efficiency, etc. [63, 5, 6, 7, 8, 9, 10, 11, 12, 13, 14]. According to [64], cabling cost may take up to 3–8% of the overall infrastructure budget. Cable bundles between server racks and blades can lead to airflow blockages which may increase power consumption for cooling or cause failure of components [65, 66].

One possible solution for the aforementioned problems is to use wireless communication in data centers. This solution will not only alleviate cable management, serviceability, and packaging constraints, but also reduce latency by providing direct communication [3, 4, 5, 6, 7, 8, 9, 10, 11, 12, 13, 14], e.g., from one rack to the rack in the next aisle, as opposed to the traditional approach of routing cables above racks or down to the floor where they are connected to a router/switch. [5] addressed the benefits and challenges of deploying wire-

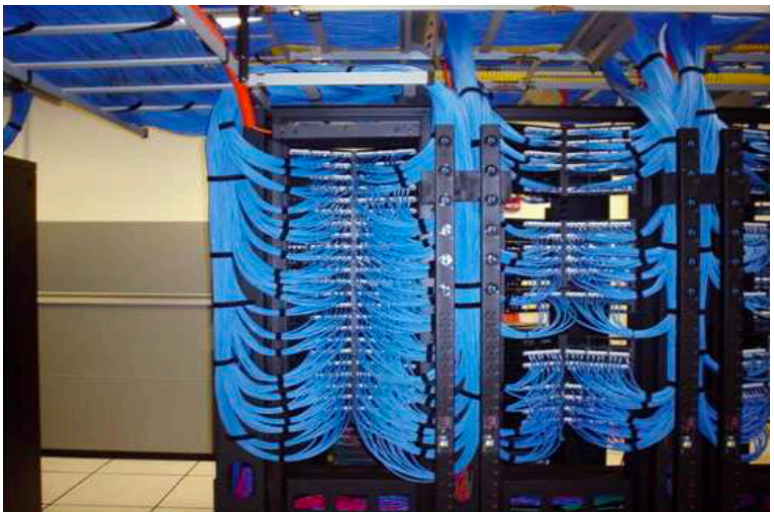

Figure 1: Cabling setup in a data center [5]: cable bundles require significant effort and cost to setup and still may cause airflow blockages and inefficient cooling.

less interconnects operating in the 60 GHz unlicensed spectrum to replace some or all of the wires for connectivity in data centers. A combination of large bandwidth and high allowable effective radiated power implies that speeds of multi-Gbps can be achieved reliably. Further, the highly directional beam at 60 GHz results in reduced interference, increased isolation, and hence improved security. Finally, since the wavelength at these frequencies is around five millimeters, antenna sizes are correspondingly small, which makes it possible to integrate the entire transceivers, including the antennas, onto a single small chip. [10] showed that multiple wireless links with 60 GHz directional antennas in a data center could run concurrently at multi-Gbps rates on the top-of-rack switches. In addition, [7, 8] proposed 3D beamforming for wireless data centers, where 60 GHz signals bounce off data center ceilings, thus establishing indirect LoS link between any two racks in a data center. A 3D beamforming testbed was built to demonstrate its ability to handle both link blockage and link interference, thus improving link range and number of concurrent transmissions in a data center. Novel rack designs and a network topology inspired by Cayley graphs were proposed [11] to provide a dense interconnect for 60 GHz wireless data centers and to achieve higher aggregate bandwidth, lower latency, and substantially higher fault tolerance than a conventional wired data center while improving ease of construction and mainte-

nance. Various data center interconnects such as 3-tier and fat-tree can be emulated on the IEEE 802.15.3c wireless networking standard at 60 GHz [3].

A key challenge for wireless communication in data centers is that the required data rates in existing systems are already in the hundreds of gigabits per second [25]. However, all the mentioned work on wireless data centers is based on 60 GHz channels with limited bandwidth, and thus can hardly satisfy the high data rates required in modern data centers. New frequency spectra with more available bandwidth, e.g, THz frequency bands, need to be explored. THz wireless communication has several key advantages that can be combined to achieve the required data rates and to facilitate wireless data centers: 1) sufficient available bandwidth [14, 13]—an IEEE 802.15.3d [17] standard for THz communication proposes a data rate up to 100 Gbit/s at 252–325 GHz using eight different bandwidths between 2.16 GHz and 69.12 GHz; 2) smaller antennas and antenna spacing at THz frequencies enables miniaturization of phased arrays for beamsteering to provide more multiple-input multiple-output (MIMO) channels within the same array aperture to reach Tbits/s data rates; 3) directionality of propagation at THz frequencies results in reduced interference and increased isolation [18, 19]; 4) data centers provide controllable environmental conditions such as a low moisture atmosphere and limited nodes mobility, which can be favorable for THz wave propagation. The frequency-dependent pathloss at THz corresponding to various frequencies and relative humidity levels was presented in [67, 20]. Highly directional antennas can be used to overcome the molecular absorption losses at the THz frequency bands [68]. In addition, optimal carrier frequency selection strategies can reduce pathloss and improve throughput [13], e.g., there are several transmission windows around 300 GHz with low atmospheric losses.

To develop THz wireless data centers for THz chip-to-chip communication, THz propagation needs to be characterized in a data center environment. Since data center data exchange demands high reliability, the effects of blockage of cables, humans, and small-scale mobility (e.g. rack vibrations) on THz propagation also need to be studied. Blockage

of cables is discussed in this thesis. Human blockage could cause additional attenuation around 35 dB at 300 GHz [69]. The scattering effect is another important propagation property that needs to be considered for THz communication as a wavelength approximates the surface roughness of the reflecting medium [70]. [71] provided detailed modeling of the diffuse scattering loss and shows that THz wireless links can be established via scattered paths. While the concept of THz wireless data centers has been mentioned in [21, 13, 14, 20] and stochastic channel models for THz wireless data centers have been reported in [14], a comprehensive characterization and modeling of THz propagation channels, which includes various obstructions in a data center, is not available.

2.4 Backscatter Communication

Backscattering communication, such as radio-frequency identification (RFID), has been widely used in everyday life. RFID is typically used in supply chain management, asset tracking, data exchange, telemetry, access control, etc. [72, 73, 74, 43, 75, 76, 77, 78, 79, 80] and has a market that is worth several billion dollars today and is expected to grow $>$ 10 % per year [81]. There are two main classes of RFID tags: *chip-based*, which uses an integrated circuit (IC) chip to store tag information [82, 83, 84, 79], and *chipless*, which uses the electromagnetic signature of the all-passive tag substrate to store the information [50, 85, 86]. The RFIDs can also be classified as passive, semi-passive, and active depending on whether the tag uses electromagnetic sources for power and communication, uses battery power for only its IC circuits, or uses battery power for both IC circuits and communication.

Traditional backscatter communication refers to a radio channel where a reader sends a continuous carrier wave (CW) signal and retrieves information from a modulated wave scattered back from a tag. During backscatter operation, the input impedance of a tag antenna is intentionally mismatched by two-state RF loads (Z_0 and Z_1) to vary the tag's reflection coefficient and radar cross section (RCS) and to modulate the incoming CW [41,

42]. Due to severe power constraints on the RFID tag, complete link budget for backscatter

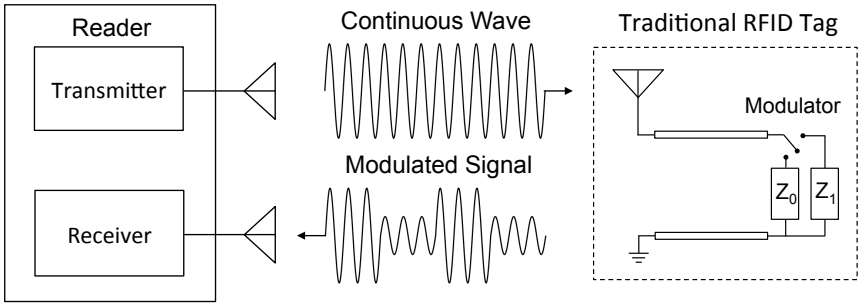

Figure 2: Traditional RFID tag.

radio and RFID systems was demonstrated by a practical ultra high frequency (UHF, in the range of 300 MHz–3 GHz) RFID [42] to give a thorough knowledge of the backscatter channel and to maximize backscatter communication system performance. [87, 88] presented 5.8 GHz semi-passive RFID tags that significantly increases the range of backscatter radio links by exploiting the quantum tunneling effect.

In recent years, mm-wave RFID (MMID) has been proposed due to its compact form factor, narrow-beamed highly directional reader antennas that enable precise angular localization, and wider available bandwidth that allows high data rates and superior spatial resolution for short-range communication and localization [43, 44, 45, 46, 47]. Three feasible applications for MMID at 60 GHz were introduced [43], including 1) wireless mass memory; 2) automatic identification systems with pointing functionality; 3) transponder communication with automotive radar. [45] proposed the first 5G-compatible implementation of a long-range, energy-autonomous MMID sensor at 28 GHz for IoT applications. [44] introduced a novel way to implement passive RFID at 10 GHz by using a Schottky diode as the mixing element to convert the RFID reader signal from mm-waves to RFID carrier frequency. [47] demonstrated a complete 34 GHz RFID ranging system that can improve ranging resolution, data throughput for RFID communication, and multi-user capability without accepting range limiting RF power restrictions in ultra-wideband (UWB, in the range of 3.1–10.6 GHz) systems. A fully functional MMID system at 72.5 GHz was

proposed [46] to significantly reduce the transponder size and achieve wider communication bandwidth with the use of mm-wave frequencies. However, the miniaturization of the transponder is still limited since antennas, which are the largest parts of the transponder [46], are still needed.

Beyond MMID, THz backscatter communication offers compact device size in the sub-millimeter scale and huge bandwidth that provides large coding capacity [48, 49, 50]. THz RFID tags based on stack of dielectric layers were presented [49, 50], where the forbidden band gap (FBG) behavior of the dielectric layers is utilized to create binary data encoding in the frequency range from 150 to 600 GHz. [48] proposed a THz chipless RFID localization system that can reach mm-level localization and suggested that huge bandwidth available at the THz band offers a potential opportunity to maximize the coding capacity using frequency coding. Compared to MMID, THz backscatter communication provides more bandwidth and can reach even higher data rates. However, the form factor of existing electronics-based RFID tags from UHF, UWB, mm-wave, up to THz bands has limited room for further miniaturization since they all need to use antennas, which are the largest parts of the transponder [46]. New backscatter architecture that can operate without antennas and is compatible with a wide range of interrogating carrier frequencies needs to be developed, e.g., THz RFID tags that do not need antennas and RF front-end circuits such that the device size can be further miniaturized and the coding capacity can be enhanced.

CHAPTER 3

CHARACTERIZATION AND MODELING OF PROPAGATION PHENOMENA RELEVANT FOR 300 GHZ WIRELESS DATA CENTER LINKS

3.1 Overview

Chapter 2.3 discussed the state of the art in channel characterization and modeling in wireless data centers. While the concept of THz wireless data centers has been mentioned in [21, 13, 14, 20] and stochastic channel models for THz wireless data centers have been presented in [14], a comprehensive characterization and modeling of THz propagation channels, which includes various obstructions in a data center is not available.

To understand the THz propagation channel in a data center environment, we first conduct channel sounding in a mock-up data center model as a starting point, which allows for more flexibility exploring a variety of potential propagation scenarios, including R2R links with optical lenses that enable long-range communication across multiple racks, and B2B vertical links that provide short-range communication between servers within the same rack. This chapter presents detailed results of characterization of 300 GHz channels in seven different wireless data center scenarios: 1) R2R line-of-sight (LoS); 2) R2R obstructed-LoS (OLoS) with obstructions of cables, metal cabinets, and mesh structures; 3) R2R reflected-non-LoS (RNLoS) links, where an aluminum reflector is used to redirect signals in NLoS links; 4) R2R obstructed-RNLoS (ORNLoS) where cables are placed between the transmitter (Tx)/receiver (Rx) and the reflector as obstructions; 5) B2B RNLoS, where two metal reflectors are used to direct waves vertically across servers; 6) B2B ORNLoS, where the B2B RNLoS link is obstructed by cables; 7) B2B LoS, where the Tx and Rx are horizontally placed on a rack server. In the R2R LoS scenario, an optical lens was used to extend the Tx-Rx separation distance. This led to a waveguide effect in the chan-

nels measured thereby resulting in a path loss exponent (PLE) of 1.48 with a shadowing gain of 0.7 dB. When obstructions of cables are present, the ORNLoS link outperforms the OLoS link with 2.5 dB lower shadowing gain and weaker multipath. The reflector in the RNLoS link has reflection coefficients very close to 1 for all incident angles. For the B2B scenario, a dual-reflector THz transceiver rack system is proposed to enable wireless links across vertically stacked servers and allow easy maintenance and repair of servers. The measured path loss closely follows the Friis values in the LoS link and in the RNLoS link with hollow vertical ground plane. When obstructions of cables are present, the ORNLoS link experiences 5–10 dB higher path loss and on average 0.25 GHz lower coherence bandwidth than the RNLoS link. Measured statistical channel properties show that the shadowing gain caused by cable clusters follows the log-normal distribution. Furthermore, we have observed that the turbulence from cooling airflow can cause the cable to vibrate, and thus lead to Doppler shift in the THz bands. Therefore, we develop a 2-D narrowband geometrical propagation model that includes moving scatterers to model the Doppler power spectrum (DPS) at 300 GHz. The proposed 2-D geometrical channel model is validated with measured data. Results show that a maximum Doppler frequency is observed as 56.1 Hz.

The remainder of the chapter is organized as follows. Section 3.2 presents the THz channel sounding system, antennas, and Polytetraflu-oroethylene (PTFE) optical lens configuration used in the measurement campaign. Section 3.3 describes the measurement environment and scenarios. Sections 3.4 and 3.5 present measurement and analysis results for R2R and B2B links, respectively. Section 3.6 describes the proposed 2-D geometrical model and model validation. Finally, Section 3.7 provides some concluding remarks.

3.2 Measurement Setup

A frequency-domain channel sounder setup was used for performing the experiment. At the heart of the measurement setup is a Keysight N5224A PNA vector network analyzer (VNA)

and Virginia Diodes, Inc. (VDI) transceivers (Tx210/Rx148) [89], which operate over a bandwidth of 20 GHz (300–320 GHz) with 801 frequency tones. The THz carrier signal is generated from electronic sources using voltage-controlled oscillators and subsequent frequency multipliers. An input signal in the range of 10 MHz–20 GHz with a power level (P_{in}) of 0 dBm is generated by the VNA and fed into the VDI Tx210 (shown in Fig. 3 (a)). Inside the Tx210, a Herley-CTI phase-locked dielectric resonator oscillator (PDRO with 100 MHz reference crystal oscillator) [90] generates a 25 GHz signal, which is amplified and its frequency doubled using Norden N08-1975 [91], and then tripled by VDI WR6.5X3 [92]. This signal is then fed into a sub-harmonic mixer WR2.8SHM [93] that doubles the carrier frequency and mixes it with the baseband signal (10 MHz–20 GHz) generated from the VNA. The signal is then transmitted by the horn antenna in the THz range of 280–320 GHz. At the Rx (shown in Fig. 3 (b)), same components are used to down-convert the signal, except that the PDRO is tuned to 24.2 GHz, which leads to a down-conversion of the received signal to an intermediate frequency (IF) of 9.6 GHz. The upper sideband of the down-converted signal is then recorded by the VNA in the frequency range of 9.61–29.6 GHz. A block diagram of the measurement system and data processing procedure is shown in Fig. 3 (c), and the corresponding measurement parameters are summarized in Table 1.

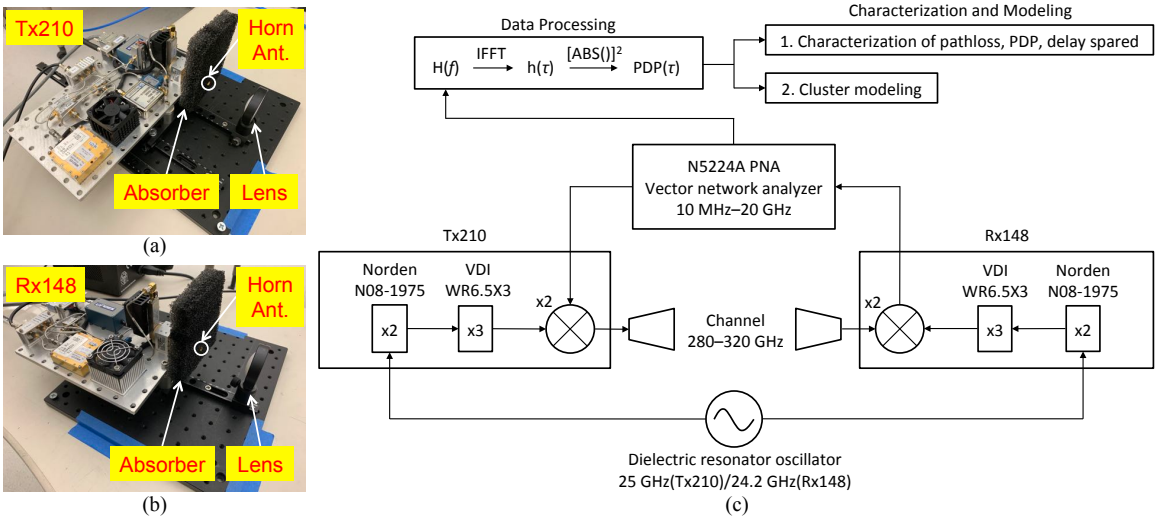

Figure 3: (a) Tx and (b) Rx configurations, (c) block diagram of the measurement system and data processing procedures.

Table 1: Measurement Parameters

Parameter	Symbol	Value
Measurement points	N	801
Intermediate frequency bandwidth	Δf_{IF}	20 kHz
Average noise floor	P_N	-90 dBm
Input signal power	P_{in}	0 dBm
Start frequency	f_{start}	10 MHz
Stop frequency	f_{stop}	20 GHz
Bandwidth	B	19.99 GHz
Time domain resolution	Δt	0.05 ns
Maximum excess delay	τ_m	20 ns

Vertically polarized pyramidal horn antennas [94] with gain that varies from 22 to 23 dBi from 300 to 312 GHz were used for this measurement campaign. The nominal half-power beamwidth (HPBW) of the horn antenna is about 10° in azimuth and elevation.

Plano-convex Polytetrafluoroethylene (PTFE/Teflon) lenses [95] with a focal length of 7.5 cm and a diameter of 5 cm are used to collimate the THz beam and provide extra gain for the scenarios in Sections 3.3.1–3.3.4. The relative position of the lenses and the Tx/Rx are shown in Fig. 4. Note that the distance between the horn and the lens is fixed at 6 cm.

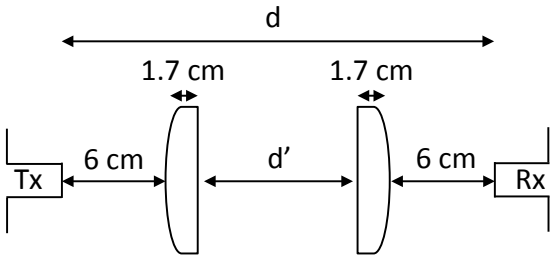

Figure 4: Polytetrafluoroethylene (PTFE) lens configuration.

Please note that we included the lenses as part of the channel rather than part of the measurement system, i.e., the gain of the lenses is included in the measurements, since channel characteristics such as multipaths have been identified as the results of reflections from the lenses. Additionally, the gain information of the PTFE optical lenses is not available.

3.3 Measurement Environment

We envision that future THz wireless data centers will leverage the integration of blade-to-blade (B2B) and rack-to-rack (R2R) links such that B2B links provide short-range communication between servers within the same rack, while R2R links enable long-range communication across multiple racks, and that future THz wireless data center will be equipped with optical lenses and THz transceivers that are miniaturized and integrated into the server chassis. The measurement designs and results provided in this paper are the starting point and proof-of-concept for realistic performance evaluations and designs and prototyping of THz communications systems in wireless data center environments. Note that "blade" represents a server mounted on a rack, and the B2B link represents communication link among different servers placed in vertical and horizontal positions on one rack.

3.3.1 R2R LoS Link

In the R2R link [6], Tx and Rx are mounted on top of server racks to enable wireless communication between racks. Fig. 5 (a) presents the measurement setup for R2R LoS link, where THz Tx/Rx and lenses are placed on top of two separate metal cabinets, acting as server racks in a data center. Measurements were taken at Tx-Rx distances of 40–210 cm in 5 cm increments. The maximum distance of 210 cm is constrained by the length of the synchronization cable that connects the Tx and Rx. We use the R2R LoS scenario both as a potential data center link as well as validation of our measurement setup in the R2R obstructed-LoS scenario.

3.3.2 R2R OLoS Link

In this section, we study a scenario where the wireless link is obstructed by cables, server racks and their mesh structures, which are common objects in data centers. According to [6, 65], long cables in data centers require overhead cable trays, where cables may be

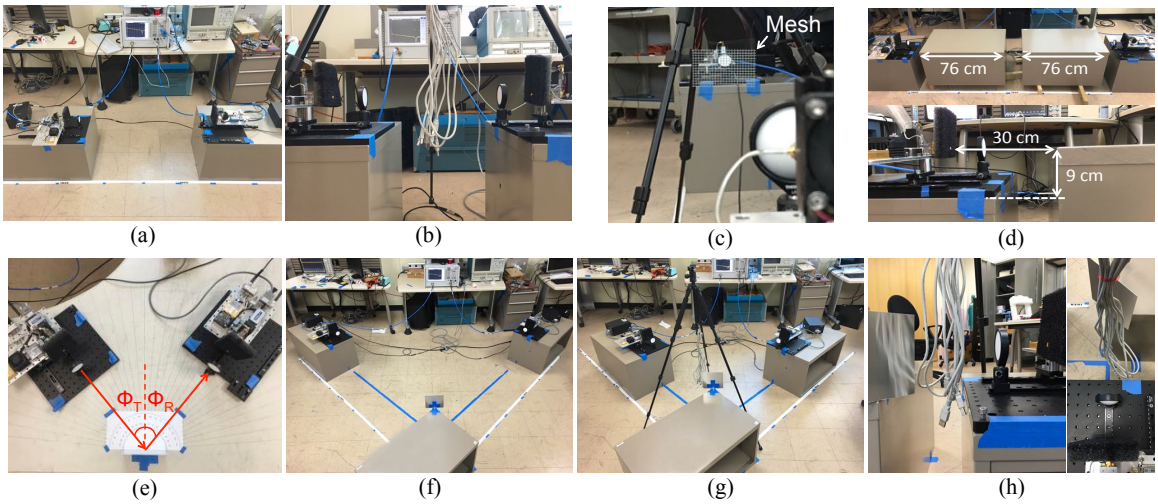

Figure 5: Measurement scenarios of the R2R link: (a) LoS; OLoS with (b) cables, (c) mesh, and (d) metal cabinets serving as obstructions; (e) RNLoS reflection coefficient measurement; (f) RNLoS; (g)/(h) ORNLoS with cables serving as an obstruction.

exposed to the R2R link between the overhead cable trays and the racks. The measurement setup for R2R OLoS link with cables as obstruction is presented in Fig. 5 (b). Following the same setup in Section 3.3.1, the LoS channel is now obstructed by a cluster of cables hung in the air from a tripod. We use a tripod to hold cables such that cables can be fixed at the same position (midpoint between Tx/Rx) while Tx/Rx were being moved. The R2R OLoS measurements with cables as obstruction have been recorded at distance of 40–210 cm with 10 cm increments. Furthermore, in a data center for an R2R scenario with a maximum distance of 210 cm, there will be multiple server racks between the Tx and Rx. Multiple metal cabinets and their mesh structures might have an influence on the channel. We have investigated R2R links with metal cabinets and mesh structures placed between the Tx and Rx that partially block the channel. The measurement setups for R2R OLoS link with mesh structures and metal cabinets as obstructions are presented in Figs. 5 (c) and (d), respectively. Measurements have been recorded at distance of 210 cm.

3.3.3 R2R RNLoS Link

R2R RNLoS links are proposed to increase transmission range and allow Tx/Rx to bypass obstructions and establish direct links without multi-hop relays [6]. Most of the existing RNLoS links in wireless data centers [6, 7, 8, 9, 14] use the entire ceiling in server rooms as reflectors, which increases cost and occupies huge space. Our configuration in Fig. 5 (f) shows that a palm-sized compact reflector would be sufficient for R2R RNLoS links in THz wireless data centers due to the very focused THz beam. If more links are required, we may increase the size of the reflector or cover the ceiling/wall with reflecting material and use them as reflectors [6, 7, 8, 9, 14]. Note that the dimension of the reflector needs to accommodate lens size. We design an aluminum square-shape reflector with length of 15 cm (roughly twice the lens diameter). R2R RNLoS measurements are recorded at Tx horn-to-reflector-to-Rx horn distance 40–210 cm with 5 cm increments with equal Tx/Rx-to-reflector distances and equal transmitting and receiving angles (ϕ_T/ϕ_R) at 45°. We use the R2R RNLoS scenario as validation of our measurement setup for the R2R RNLoS that we later used for the obstructed-RNLoS scenario. Furthermore, we also characterized the reflection coefficient and the angular misalignment tolerance range of the aluminum reflector used in the R2R RNLoS link with the measurement setup in Fig. 5 (e). In the reflection coefficient measurement, to ensure specular reflection, the angle of incidence (ϕ_T) is set equal to the angle of reflection (ϕ_R) in the range from 20° to 85° in 5° increments with Tx horn-to-reflector-to-Rx horn distance fixed at 90 cm. This setup is chosen to test the stability of the reflector's reflection coefficient in various Tx/Rx angular setups since in reality the R2R RNLoS link may not be able to position the reflector at exact $\phi_T = \phi_R = 45°$, e.g., obstructions or location of the racks may vary. In the angular misalignment measurement, ϕ_T is fixed at 45° while ϕ_R varied from 5° to 85° in 5° increments with Tx horn-to-reflector-to-Rx horn distance fixed at 90 cm. This setup is chosen to test the angular misalignment tolerance range.

3.3.4 R2R ORNLoS Link

Figures 5 (g) and (h) present the measurement setup for the R2R ORNLoS link with cables as obstruction. Similar to Section 3.3.3, here we position a tripod with obstructing cables between the Tx and the reflector. R2R ORNLoS measurements are recorded at distance of 40–210 cm with 10 cm increments.

3.3.5 B2B RNLoS Link

In the B2B RNLoS scenario, rack-mounted reflectors are used to enable wireless links across vertically stacked servers. Optical lenses are not applied due to shorter communication range and limited space in a B2B environment. Fig. 6 (a) and Figs. 7 (a)–(d) present schematics and the measurement setup of the B2B RNLoS link. Note that the rack in Fig. 7 is a mock-up of a real server rack. Tx is placed at the lower blade (blade 2) and Rx is placed at the upper blade (blade 1), both of which are facing toward the vertical metal panel of the cabinet. To enable a link between Tx and Rx, we position two rack-mounted reflectors in a similar manner as in a periscope, i.e., two reflectors are positioned at 45° to the direction where Tx and Rx are pointed to, such that the transmitted signal can reach the Rx via a vertical channel between two vertically aligned reflectors. Using metal reflectors for communication between two blades can be extended to multiple blades by having longer metal reflectors. Many of the datacenter racks come with a metal enclosure that can be leveraged as a reflector. Data exchange at each server node is typically point-to-point communication, where a switch will be used to connect multiple servers onto the network. Interference may need to be handled for the coexistence of multiple B2B links. Fortunately, due to the narrow beamwidth at THz frequencies, interference can be better managed compared to lower frequencies. One advantage of using rack-mounted reflectors as compared to waveguides is that it allows easy maintenance and repair of blades. In addition, we want to test the possibility of using reflectors for NLoS type of link inside a server rack since there may be obstacles inside server compartments blocking the propagation path, which require

redirecting the THz beam. Reflectors will provide more flexibility for realizing NLoS type of links inside a server rack. In Fig. 6 (a), d1 = d3 are the Tx/Rx-to-reflector distance, d2 = 15 cm is the distance between the Tx- and Rx-reflectors (roughly twice/four times of the height of the 2U/1U rackmount servers [96]), d4 = 4 cm is the gap between rack's vertical ground plane and the edge of the reflector, d5 = 2.2 cm is the distance between the horizontal ground plane and the horn center. We have found that reflection can be generated from both vertical and horizontal ground planes inside the rack (paths 1, 2, and 3 in Figs. 6 (b) and (c)) and can lead to significant path loss variation as distance increases. To better understand the reflection in a B2B environment, we conducted our experiments with three vertical ground plane designs in a server compartment: 1) solid metal (Fig. 8 (a)), 2) hollow (Fig. 8 (b)), and 3) mesh (Fig. 8 (c)) structures. Since we want to focus on analyzing reflection from the vertical ground plane, we limit the total distance (d = d1 + d2 + d3) to within 49 cm such that the reflection interference from blade 2's horizontal ground plane (path 3 in Fig. 6 (c)) can be minimized. The server rack we use has a dimension of 130 cm x 75 cm x 45 cm. The opening window of the vertical ground plane (Fig. 8) has a size of 12 cm x 10 cm. The Tx/Rx reflectors are made of aluminum and have dimensions of 15 cm x 5 cm. Note that the size of reflectors should accommodate the height and the beamwidth of the Tx/Rx antennas, and that the alignment of Tx/Rx reflectors is critical since the received signal is extremely sensitive to the positioning of the reflectors. We briefly discuss the consequences of misaligned reflectors in the following paragraphs. The B2B RNLoS measurements have been recorded as the total horn-to-horn distance (d = d1 + d2 + d3) varied from 20 cm to 49 cm with 1 cm increments (both d1 and d3 change and d1 = d3).

3.3.6 B2B ORNLoS Link

Our measurement setup for the B2B ORNLoS link is presented in Fig. 8 (d). Similar to the setup in Section 3.3.5, here we place the obstructing cables supported by a tripod through the opening window of the vertical ground plane between the Tx- and Rx-reflectors. B2B

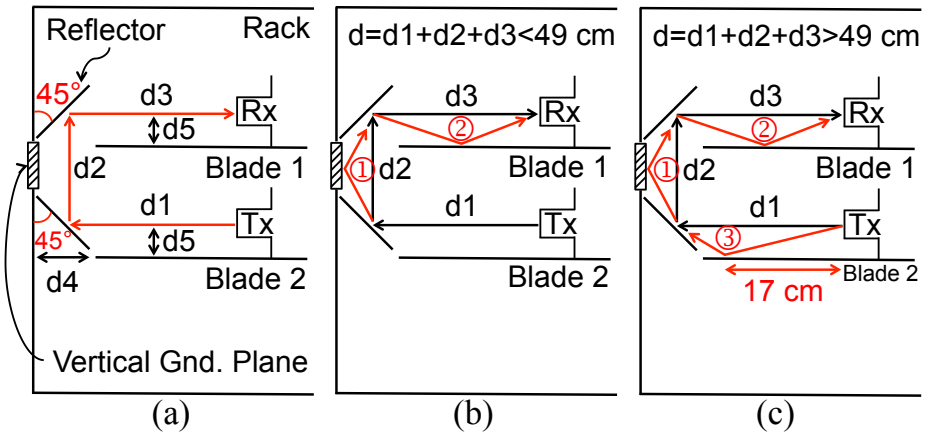

Figure 6: (a) Schematics of B2B RNLoS measurement setup. Analysis of reflection interference in B2B environment at (b) d $<$ 49 cm and (c) d $>$ 49 cm.

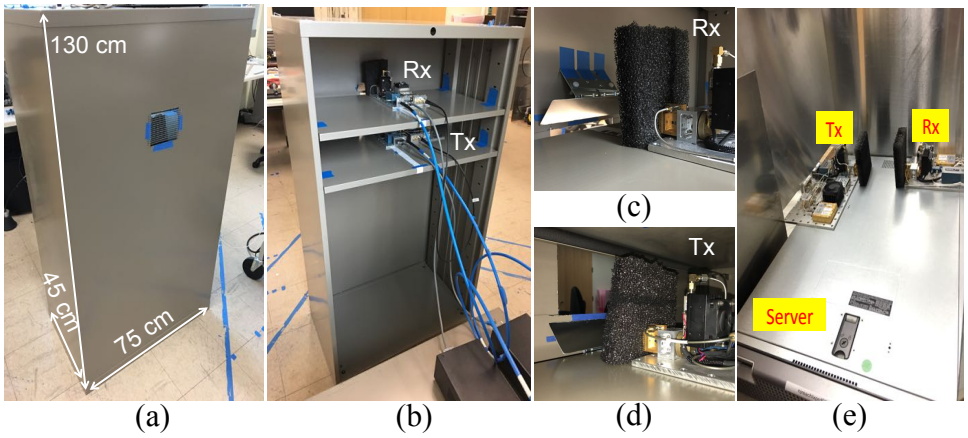

Figure 7: Measurement setup of the vertical B2B link: (a) back and (b) front sides of the rack, (c) Rx and Rx-reflector at the upper blade, (d) Tx and Tx-reflector at the lower blade; (e) measurement setup of the B2B LoS link.

ORNLoS measurements are recorded at distance of 20–49 cm with 1 cm increments.

3.3.7 B2B LoS Link

Our measurement setup for the B2B LoS link is presented in Fig. 7 (e), where the Tx and Rx are placed on a rack server and aligned horizontally as common blade servers are placed on a rack. Aluminum plates are placed around the rack server to mimic a rack compartment environment. The B2B LoS measurements have been recorded at distance of 12, 14, 16, and 18 cm. Tx-Rx distances are selected such that they are greater than the thickness of

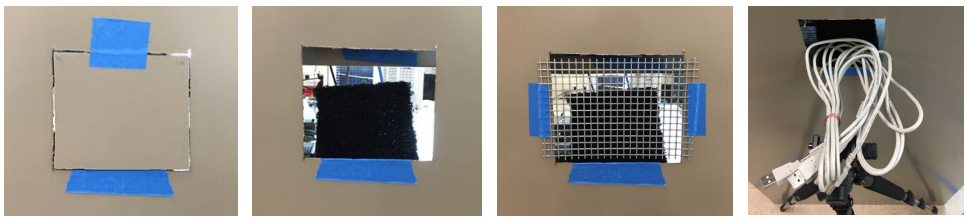

(a) (b) (c) (d)

Figure 8: Vertical ground plane designs in B2B server compartments: (a) solid metal, (b) hollow structure, and 3) mesh structure; (d) hollow structure with cables as obstruction.

one blade server (4.4 cm for one blade according to [96]) or multiple blade servers.

3.3.8 B2B OLoS Link With Vibrating Cables Serving as Obstruction

The existence of loosely bundled cables in data centers between server racks and compartments [15] could have impacts on rack-to-rack communication. This is an especially important case where the turbulence from cooling airflow in the data center can cause the cable to vibrate, and thus lead to Doppler shift in the THz bands. To characterize the aforementioned Doppler shift in this type of data center scenario, we consider a fixed wireless scenario in which the Tx and Rx were stationary with the cable(s) serving as the moving scatterer [97, 98, 99, 100]. A narrow-band measurement was performed in a setup illustrated in Fig. 9, where a cooling fan was placed underneath the cable cluster to create the turbulence, and Tx-Rx distance is 40 cm. The fan was placed 30 cm below the Tx/Rx to ensure its enclosure did not interfere with the propagation channel.

3.4 R2R Results and Analysis

3.4.1 Characterization of R2R LoS and R2R RNLoS Links

Here we characterize the relationship between Tx-Rx distance and path loss, PDPs, and B_c in the R2R LoS and R2R RNLoS scenarios as introduced in Figs. 5 (a), (f) and Sections 3.3.1 and 3.3.3.

Figures 10 (a) and (b) present the measured path loss with Tx-Rx distances at 50–210

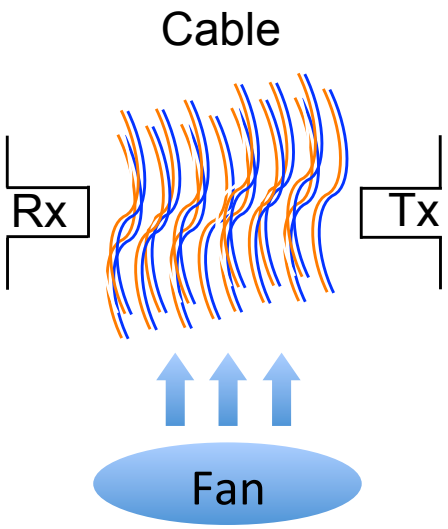

Figure 9: Illustration of the B2B OLoS link with vibrating cables serving as obstruction.

cm in R2R LoS and R2R RNLoS scenarios, respectively. Similar path loss values that range

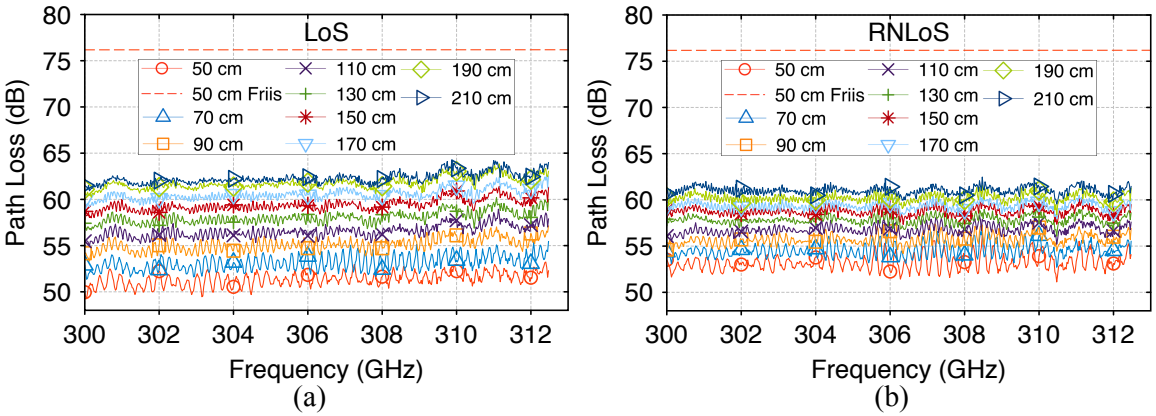

Figure 10: Measured path loss curves in (a) R2R LoS and (b) R2R RNLoS scenarios at distance of 50, 70, 90, 110, 130, 150, 170, 190, 210 cm along with Friis theoretical path loss at distance of 50 cm.

between 50–64 dB have been observed in the LoS and RNLoS links at distances between 50–210 cm. Friis theoretical path loss at distance of 50 cm is also presented in Figs. 10 (a) and (b) to demonstrate that more than 25 dB additional gain can be obtained with the use of optical lenses. Note that due to the very focused beam created by the lenses, the channel characteristics (e.g. multipath, ripples in transfer function) in the R2R scenarios are dominated by the effects of the lenses rather than the surrounding environment. As a

result, we will include the lenses as part of the propagation channel rather than part of the measurement system. We can observe that periodic ripples in the measured path loss curves are the strongest at near distances and slowly attenuate as distance increases. The reason is that ripples result from multiple reflections between horns and lenses, and the reflections gradually decay as distance increases. Note that the periodic path loss ripples are not caused by the antenna gain diagram since antenna's peak-to-peak gain variations over frequency are only around 0.6 dB while the measured path loss ripples have peak-to-peak values up to 4 dB.

Figure 11 presents a comparison of FI path loss models and the measured mean path loss for the R2R LoS and R2R RNLoS scenarios at distance of 40–210 cm. Detailed path loss model parameters are summarized in Fig. 11. It can be observed that the R2R RNLoS

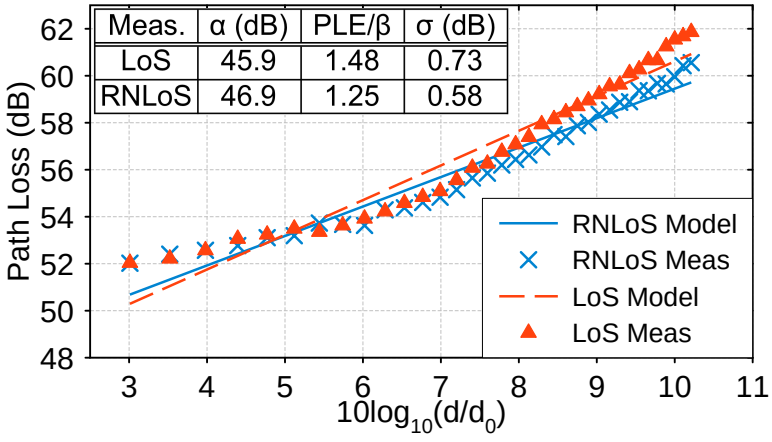

Figure 11: Measured mean path loss for the R2R LoS (red triangles) and R2R RNLoS (blue cross signs) scenarios and FI path loss models for the R2R LoS (red dash line) and the R2R RNLoS (blue solid line) scenarios at distance of 40–210 cm and $d_0 = 20$ cm.

link has similar path loss values as the R2R LoS link. We can also observe that both the R2R LoS and the R2R RNLoS links act as waveguides with PLEs of 1.48 and 1.25 due to the use of optical lenses. Interestingly, we found that both R2R LoS link (red triangles in Fig. 11) and R2R RNLoS link (blue cross signs in Fig. 11) seem to have two trends of slopes (PLE): one from 3 to 6 dB of x-axis and the other from 6 to 10 dB of x-axis. From 3 to 6 dB of x-axis, both R2R LoS and R2R RNLoS links have similar slopes of around

0.5. From 6 to 10 dB of x-axis, the R2R LoS link has a slope of around 2, whereas the slope is around 1.6 in the R2R RNLoS link. We conclude that two trends of slopes in the R2R LoS and R2R RNLoS links result from the divergence of the beam given the fact that the collimated beam created by the lenses is not perfectly parallel. At distance between 40 cm and 80 cm (from 3 to 6 dB of x-axis), the diverging of the collimated beam is less significant and thus the R2R LoS link and the R2R RNLoS link have similar path loss values and slopes. In contrast, at distance between 80 cm and 210 cm (from 6 to 10 dB of x-axis), the collimated beam diverges to an extent such that the received signal starts to decay at a faster rate for both R2R LoS and R2R RNLoS links. Specifically, for the R2R LoS link, the received signal decays at a rate similar to free space with a path loss slope (PLE) of around 2, while for the R2R RNLoS link, a lower PLE of around 1.6 is observed, which is due to the fact that reflector helps to "collect" the diverged waves and transmit back to the Rx, resulting in lower path loss values.

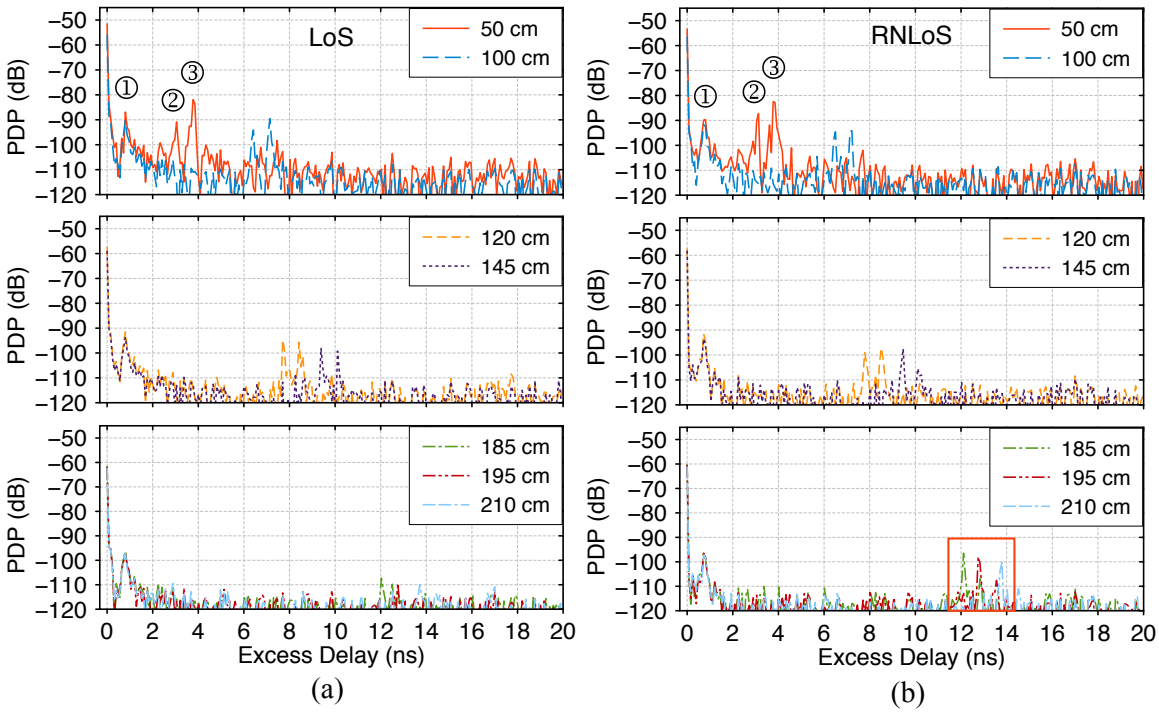

Figure 12: Measured PDPs for (a) R2R LoS and (b) R2R RNLoS scenarios at distance of 50, 100, 120, 145, 185, 195, 210 cm.

Figure 12 shows the measured PDPs for R2R LoS and R2R RNLoS scenarios at distance of 50–210 cm. We categorize multipaths into three clusters as shown in Figs. 12 (a) and (b). Cluster 1 results from reflections between (Tx lens and Tx horn) and (Rx lens and Rx horn), where a time delay of 0.8 ns corresponds to four times of lens-horn distance. Note that cluster 1's time delay does not change as distance increases because the horn-lens distance is always 6 cm (please refer to Fig. 4). Cluster 2 results from reflections between Tx lens and Rx horn and between Rx lens and Tx horn. Take the R2R LoS 50 cm PDP curve (red curve in Fig. 12 (a)) for example, cluster 2 has a delay about 3 ns corresponding to an additional delay path of 90 cm that is roughly twice the distance from the Rx horn to the Tx lens plus multiple reflected paths within the Rx lens. Cluster 3 is due to Rx horn-to-Tx horn reflection. Take the R2R LoS 50 cm PDP curve (red curve in Fig. 12 (a)) for example, it can be observed that cluster 3 has a delay around 3.7 ns corresponding to an additional delay path of 111 cm that is roughly twice the distance from the Rx horn to the Tx horn plus multiple reflected paths within the Rx lens and the Tx lens. Since the surrounding area of the Tx and Rx horns are covered with absorbers, we can conclude that the tips and internal surfaces on the horns are the cause of horn-related multiple reflections. From Figs. 12 (a) and (b), we can observe that as distance gradually increases, clusters 2 and 3 in the R2R LoS link and cluster 3 in the R2R RNLoS link gradually decayed below the noise floor (cluster 3 decreased at a faster rate than cluster 2), while cluster 2 in the R2R RNLoS link remained visible. As distance increases to 185–210 cm, only cluster 1 in the R2R LoS link remained as shown in Fig. 12 (a). On the contrary, both clusters 1 and 2 in the R2R RNLoS link remained observable at around 12–14 ns at distance up to 210 cm as shown in Fig. 12 (b). The comparison in Figs. 12 (a) and (b) shows that the reflector in R2R RNLoS link preserved reflections between Tx lens and Rx lens and sustained cluster 2 in PDPs over distances of 50–210 cm. This difference in PDPs between R2R LoS and R2R RNLoS links has an impact on the B_c values and the maximum data rate as discussed in the next paragraph. In addition, we can infer that reflections from server rack frames

(metal cabinets in our mock-up) are insignificant in the R2R LoS and R2R RNLoS links since the dominant multipath clusters 1, 2, and 3 are from reflections between the lenses.

B_c is a key parameter whose value is relative to the available bandwidth and data rate of the transmitted signal, and therefore determines the need for employing channel protection techniques, e.g., channel equalization, channel coding, or channel diversity to overcome the dispersive effects of multipaths [101]. In this paper, B_c is estimated from τ_{rms} with a correlation coefficient of 0.9 using (7). When calculating τ_{rms} from PDP, we perform noise filtering on PDP to remove unwanted noise by setting a threshold level at 8 dB above the noise floor, where PDP values below this threshold are considered as noise and set equal to zero. Fig. 13 shows the measured B_c for R2R LoS and R2R RNLoS scenarios at distance of 40–210 cm. An overall trend of increasing B_c as distance increases is observed in both

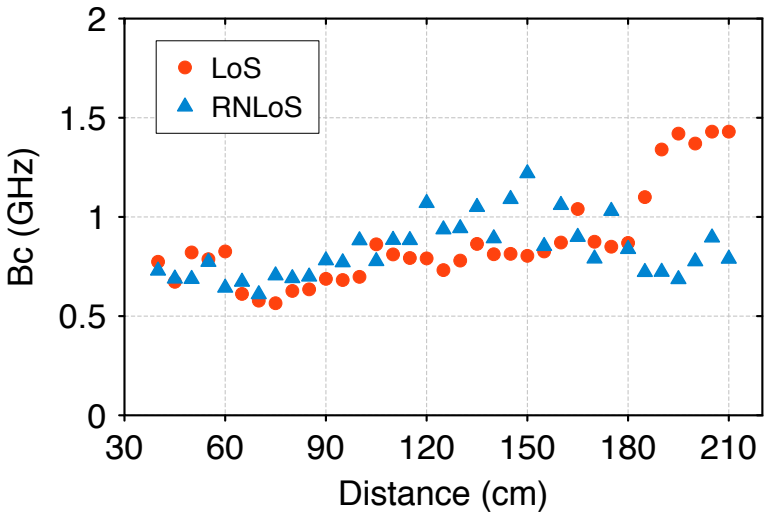

Figure 13: Measured B_c for R2R LoS and R2R RNLoS scenarios at distance of 40–210 cm.

LoS and RNLoS links, which is counterintuitive because τ_{rms} is expected to increase as distance increases due to wider beamwidth coverage of surrounding objects at further distance, resulting in decreased B_c. This counterintuitive observation results from the highly focused beam created by the lenses used in our measurement. Optical lenses effectively collimate the beam such that the propagating wave stays within the "cylindrical tube" created by the lenses. Because of this confined "tube-like" propagation channel, even though

the distance increases, there is no additional multipath involved in the channel except for clusters 1, 2, and 3 shown in Fig. 12. As distance increases, the existing clusters 1, 2, and 3 are attenuated thereby leading to a reduction in τ_{rms} and an increment in B_c. If we look into Fig. 13 more carefully, at distance around 60-180 cm, the RNLoS link has a slightly higher B_c than the LoS link. This is mostly due to reflector's reflection loss (shown in Fig. 20). At distance of 60-180 cm, the amplitude of multipath clusters 1, 2, and 3 in the RNLoS link in Fig. 12 (b) is slightly lower than that in the LoS link in Fig. 12 (a) due to reflection loss of the reflector. The attenuated multipath in the RNLoS link leads to a slightly lower τ_{rms} and slightly higher B_c. Similar observation is found in the obstructed R2R links in Fig. 16, where on average B_c in the ORNLoS link is slightly higher than the OLoS link due to suppressed multipath. Now if we compare the B_c in Fig. 13 at distances beyond 180 cm, it is observed that the B_c in the LoS link is higher than the RNLoS link by approximately 1 GHz. The suppressed B_c in the RNLoS link is caused by the scattering effect of the metal reflector. According to [102], metal objects can be viewed as perfect electrical conductors with a slightly rough surface and can cause scattering in the THz frequencies. The reflector in the RNLoS link slightly scatters the beam such that the beam is no longer ideally confined within the "tube-like" propagation channel and is reflected off of the metal rim of the lenses. As a result, multipath cluster 2 in the RNLoS link remains observable even at distances beyond 180 cm (highlighted in Fig. 12 (b)) due to reflections from the lens rim, resulting in higher τ_{rms} and lower B_c. Narrower B_c in the R2R RNLoS link may limit the maximum data rate.

3.4.2 Characterization of R2R OLoS and R2R ORNLoS Links

Here we investigate the relationship between Tx-Rx distance and path loss, PDPs, and B_c in the R2R OLoS link with cables, mesh structures, and metal cabinets as obstructions and the R2R ORNLoS link with cables as obstruction introduced in Figs. 5 (b), (g), (h), and Sections 3.3.2 and 3.3.4.

Figures 14 (a) and (b) compare the Friis path loss and the measured path loss in R2R OLoS and R2R ORNLoS links with cables as obstruction at distance of 50, 110, 150, 210 cm. We can observe that the R2R ORNLoS link has lower path loss (5 dB lower at distance

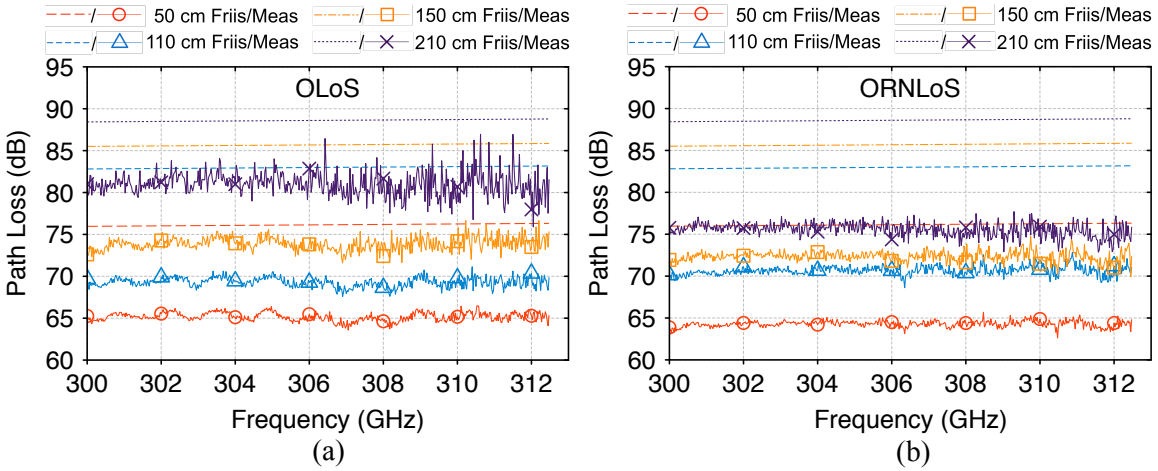

Figure 14: Measured path loss curves in (a) R2R OLoS and (b) R2R ORNLoS scenarios with cables as obstruction at distance of 50, 110, 150, 210 cm.

beyond 1.3 m) and less path loss fluctuations with frequency than the R2R OLoS link. The THz wave experiences both diffraction and reflection as propagating through cable clusters due to the fact that the radius of cables' curvature is comparable to the wavelength at 300 GHz. These diffracted and reflected waves are "collected" by the reflector in in R2R ORNLoS link and transmitted from the Tx to the Rx, resulting in lower path loss as compared to the R2R OLoS link. Measured PDPs for R2R OLoS and R2R ORNLoS links at distance of 50, 110, 150, 210 cm are presented in Figs. 15 (a) and (b). It has been observed that in the presence of obstructing cables, most of major multipath clusters (2 and 3) in Figs. 12 (a) and (b) are no longer visible. Measured B_c for R2R OLoS and R2R ORNLoS scenarios at distance of 40–210 cm is presented in Fig. 16. We can observe that as distance increases from 40 cm to 210 cm, B_c decreases from around 1.5–1.8 GHz to around 0.3–0.8 GHz. The R2R ORNLoS link has a wider B_c than the R2R OLoS link, corresponding to a relatively flat frequency domain response in Fig. 14 (b) compared to Fig. 14 (a), due to R2R ORNLoS link's suppressed multipath as shown in Figs. 15 (a) and

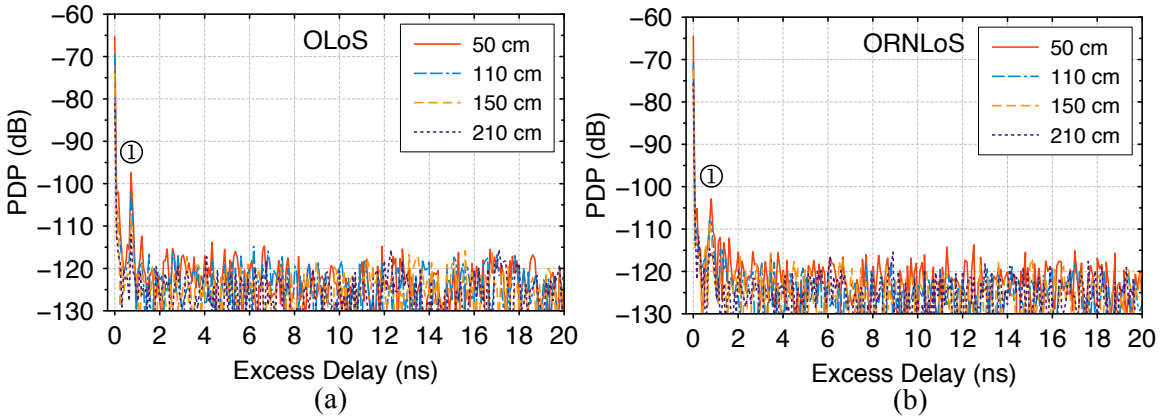

Figure 15: Measured PDPs for (a) R2R OLoS and (b) R2R ORNLoS scenarios with cables as obstruction at distance of 50, 110, 150, 210 cm.

(b).

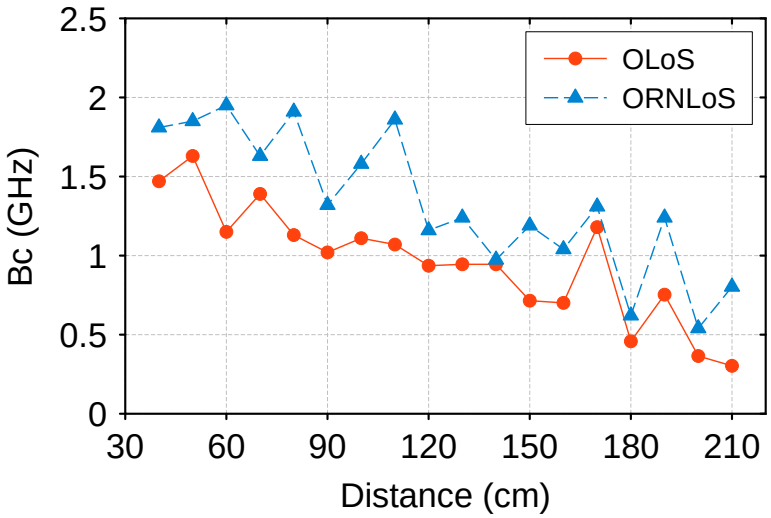

Figure 16: Measured coherence bandwidth (B_c) for R2R ORNLoS and R2R OLoS scenarios with cables as obstruction at distance of 40–210 cm.

We have further investigated the shadowing gain (X_σ) in the R2R OLoS and the R2R ORNLoS links with cables as obstructions by repeating the measurements with three cable thickness sizes and ten cable positions at distance of 40–210 cm to have enough ensemble to perform a statistical evaluation. We found that the shadowing gain of both R2R OLoS and the R2R ORNLoS links follow a log-normal distribution with its logarithmic equivalent having a zero-mean (in dB) and standard deviations (σ) of 6.8 dB and 4.3 dB, respectively.

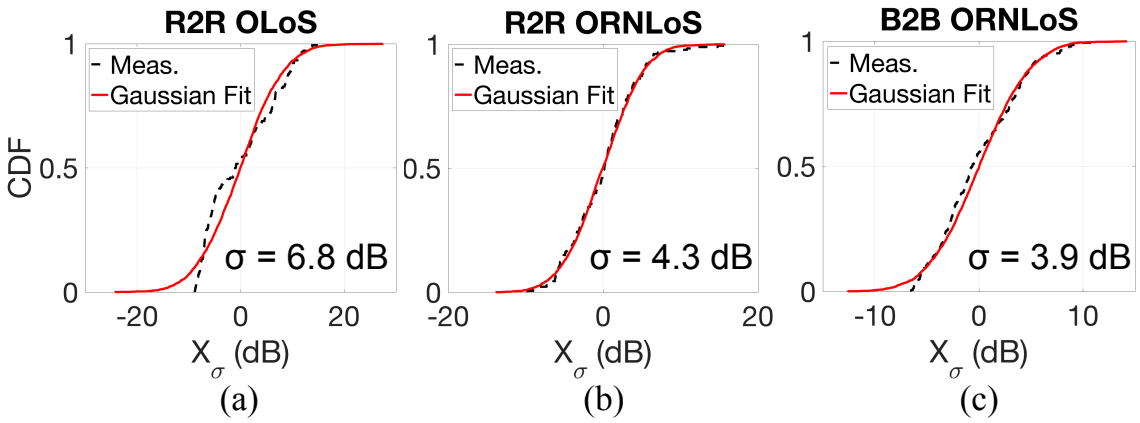

Figure 17: CDFs of the shadowing gain (X_σ) for (a) R2R OLoS link at distance of 40–210 cm, (b) R2R ORNLoS link at distance of 40–210 cm, (c) B2B ORNLoS link at distance of 20–49 cm, all measured with three cable thickness sizes and ten cable positions.

Cumulative distribution functions (CDFs) of X_σ for both links are presented in Figs. 17 (a) and (b) to confirm the log-normality of the shadowing gain.

Figure 18 presents the measured path loss at distance of 210 cm in the R2R LoS link (scenario in Fig. 5 (a); red circles) and in the R2R OLoS links with obstructions of mesh structures (scenario in Fig. 5 (c); green cross signs) and metal cabinets (scenario in Fig. 5 (d); blue triangles). Friis path loss at distance of 210 cm is presented alongside as a reference (red dash curve). Additional path loss of around 3 dB and 10 dB were observed due to the obstructions of mesh structures and metal cabinets, respectively. Fig. 19 shows the measured PDPs at distance of 210 cm in the R2R LoS link (red curve) and in the R2R OLoS links with obstructions of mesh structures (blue dash curve) and metal cabinets (purple dot curve). Two dominant multipaths have been observed: 1) multipath 1 is located at around 0.8 ns (same cause as cluster 1 in Fig. 12) and is present in all scenarios; 2) multipath 2 is only present in the R2R OLoS link obstructed by metal cabinets and is located at around 2 ns, which corresponds to two times of the distance (30 cm) between the middle cabinets and the Tx/Rx racks as shown in Fig. 5 (d).

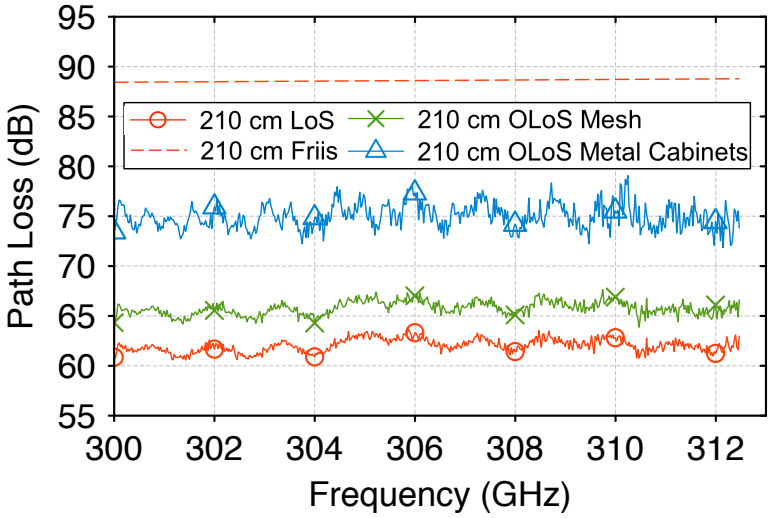

Figure 18: Measured path loss curves at distance of 210 cm in the R2R LoS link (red circles) and in the R2R OLoS links with obstructions of mesh structures (green cross signs) and metal cabinets (blue triangles). Friis path loss at distance of 210 cm is presented alongside as a reference (red dash curve).

3.4.3 Characterization of Reflection Coefficients of Reflectors

In this section, we characterize the reflection loss and the reflection coefficient of the aluminum reflector used in the R2R RNLoS link with optical lenses applied to the Tx/Rx. Similar characterization of the reflectors in the B2B RNLoS link without Tx/Rx optical lenses can be found in [103]. Our measurement setup is introduced in Fig. 5 (e) and Section 3.3.3. Calculation of reflection loss of the aluminum reflector in the R2R link is obtained by calculating the difference between the R2R LoS received power at distance of 90 cm and the R2R RNLoS received power with $\phi_T = \phi_R = 45°$ and Tx horn-to-reflector-to-Rx horn distance at 90 cm. The reflection coefficient is found from the reflection loss,

$$RL = -20 \log_{10} |\Gamma|, \tag{13}$$

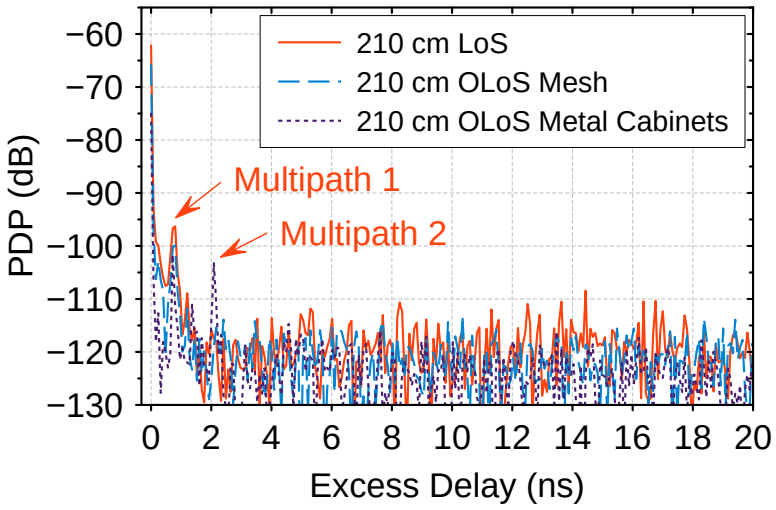

Figure 19: Measured PDPs at distance of 210 cm in the R2R LoS link (red curve) and in the R2R OLoS links with obstructions of mesh structures (blue dash curve) and metal cabinets (purple dot curve).

where Γ is the reflection coefficient and RL is the reflection loss in dB, which is calculated from the link budget equation,

$$RL = P_t - P_r + G_t + G_r - \overline{PL}[dB]. \tag{14}$$

Note that similar characterization of the reflectors in the B2B RNLoS link without Tx/Rx optical lenses can be found in [103].

Figure 20 presents the measured reflection loss of the aluminum reflector used in the R2R RNLoS link. Averaged reflection loss is calculated as 0.6 dB across the measured frequencies (from 300 GHz to 312 GHz). Fig. 21 (a) and Fig. 22 (red circles) present the measured path loss and the magnitude of reflection coefficient of the aluminum reflector used in the R2R RNLoS link with $\phi_T = \phi_R = 20°, 40°, 45°, 50°, 70°$. It is observed that the measured path loss values approximate 55 dB, which result in reflection coefficients very close to 1 across all ϕ_T and ϕ_R angles. Fig. 21 (b) and Fig. 22 (blue triangles) present the measured path loss and the magnitude of reflection coefficient of the aluminum reflector used in the R2R RNLoS link with ϕ_T fixed at 45° while ϕ_R varies at 20°, 40°, 45°, 50°,

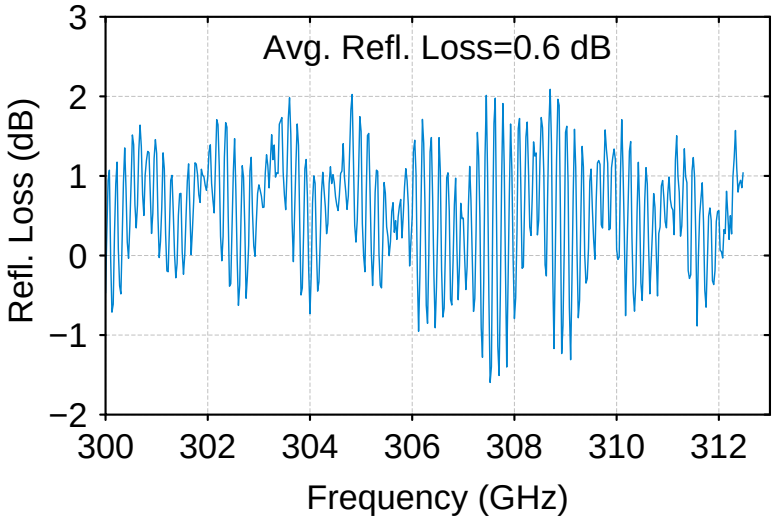

Figure 20: Measured reflection loss of the aluminum reflector used in the R2R RNLoS link. The averaged reflection loss is calculated as 0.6 dB.

70°. It is observed that as ϕ_R deviates from ϕ_T by only 5° (from $\phi_R = 45°$ to 40° or 50°), path loss increases more than 20 dB and reflection coefficient decreases from around 1 to less than 0.1 due to very focused beam. We can conclude that the reflector serves as a good reflecting surface for reliable RNLoS links at all angles ($\phi_T = \phi_R$). However, angular misalignment ($\phi_T \neq \phi_R$) requires careful attention in RNLoS links in THz wireless data centers given that the angular misalignment tolerance range is less than 5°.

3.5 B2B Results and Analysis

3.5.1 Characterization of B2B RNLoS and B2B ORNLoS Links

In this section, we investigate the reflection from vertical ground planes of different structures and how Tx-Rx distance relates to the path loss, PDPs, and B_c in the B2B RNLoS and B2B ORNLoS scenarios as introduced in Figs. 6–8 and Sections 3.3.5 and 3.3.6.

Figure 23 presents the Friis theoretical path loss (red line) and the measured mean path loss with different vertical ground plane structures: 1) solid metal (yellow circles), 2) hollow structure (blue triangles), 3) mesh structure (purple squares), and 4) hollow structure with cables as obstruction (green diamonds) in the vertical B2B link at distance of 20–

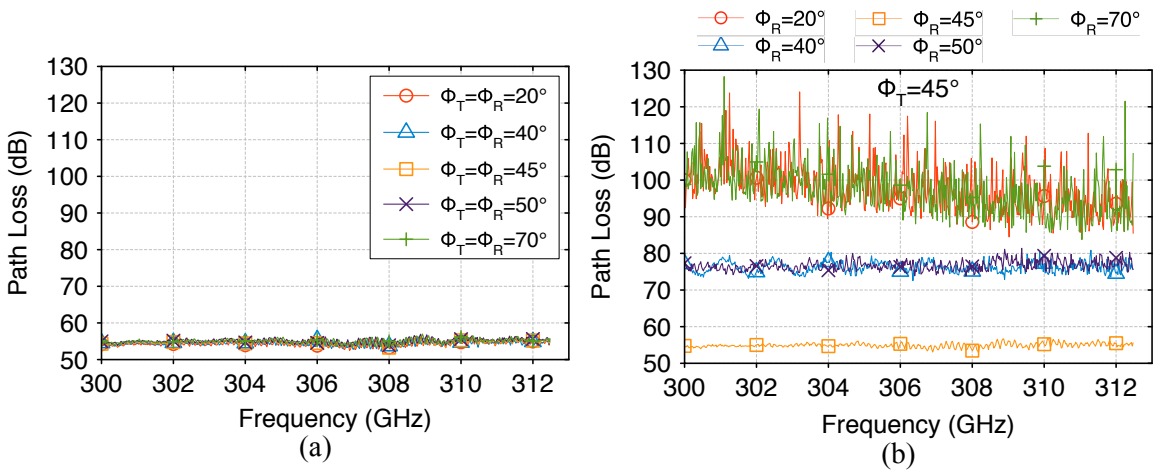

Figure 21: Measured path loss in the R2R RNLoS link at distance of 90 cm with (a) $\phi_T = \phi_R = 20°, 40°, 45°, 50°, 70°$; (b) $\phi_T = 45°$, $\phi_R = 20°, 40°, 45°, 50°, 70°$.

49 cm. It is observed that path loss fluctuates around the theoretical values as distance increases. Specifically, the hollow structure causes the least path loss fluctuation, closely followed by the mesh structure, while the solid structure creates the most unwanted path loss fluctuation around 4 dB above the Friis path loss. This path loss fluctuation is mainly caused by constructive and destructive interference from two reflected paths: 1) vertical ground plane (path 1 in Fig. 6 (b)) and 2) horizontal ground plane (path 2 in Fig. 6 (b)). Our measurement results show that the vertical ground plane has more dominant effects on the path loss fluctuation than the horizontal ground plane in vertical B2B links since strong path loss fluctuation is observed when solid vertical ground plane is applied (yellow circles in Fig. 23), while without the solid vertical ground plane, only slight path loss fluctuation is observed (blue triangles in Fig. 23). As a result, for future THz B2B communication system design, we recommend to use a hollow structure instead of solid metal for vertical ground planes on server racks to minimize path loss fluctuation. The following comparisons of measured path loss, PDPs, and B_c for the B2B RNLoS and B2B ORNLoS links are based on the hollow structure design in Fig. 8 (b) since it has the least path loss interference from vertical ground plane.

Note that besides vertical ground plane design, one of the key challenges in designing

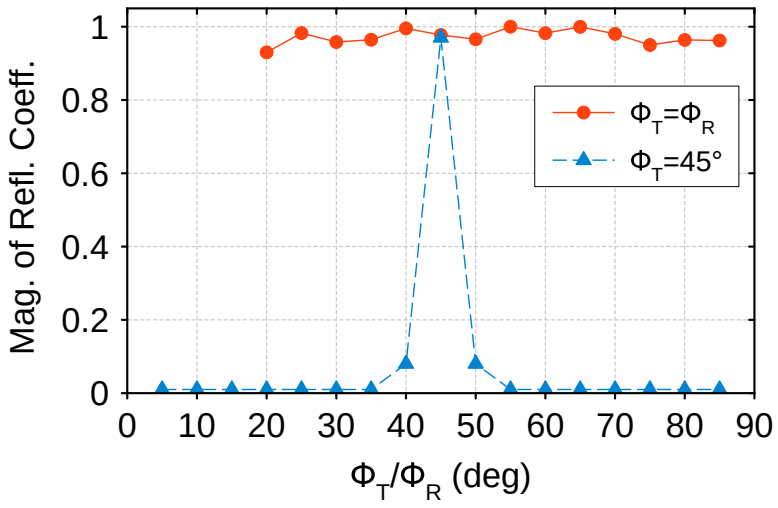

Figure 22: Measured magnitude of the reflection coefficient of the aluminum reflector used in the R2R RNLoS link: 1) $\phi_T = \phi_R$ in a range from 20° to 85° (red circles); 2) ϕ_T is fixed at 45° while ϕ_R varies from 5° to 85° (blue triangles).

vertical B2B links is the positioning of the Tx/Rx reflectors. Misaligned reflectors may increase path loss and path loss fluctuation, or even cause complete signal loss. Here we briefly discuss the consequences of misaligned reflectors. We use the same hollow vertical ground plane design in Fig. 8 (b) but intentionally tilt the Rx reflector around 1° away from the original 45° position. Fig. 24 shows the Friis theoretical path loss (red line) and the measured mean path loss with misaligned Rx reflector (blue triangles) at distance of 20–49 cm. It is observed that the misaligned reflector can cause up to 4 dB path loss deviation from the Friis values. Therefore, for future THz B2B link design, we recommend to integrate the Tx/Rx reflectors into the server racks for better alignment since the received signal is extremely sensitive to the positioning of the reflectors.

Next, we compare the measured path loss, PDPs, and B_c between B2B RNLoS and B2B ORNLoS links with a hollow vertical ground plane design. Fig. 23 compares the Friis theoretical path loss (red line) and the measured path loss curves in B2B RNLoS (blue triangles) and B2B ORNLoS (green diamonds) scenarios over distances at distance of 20–49 cm. Figs. 25 (a) and (b) present the Friis theoretical path loss curves and the measured path loss curves over frequencies in B2B RNLoS and B2B ORNLoS scenarios

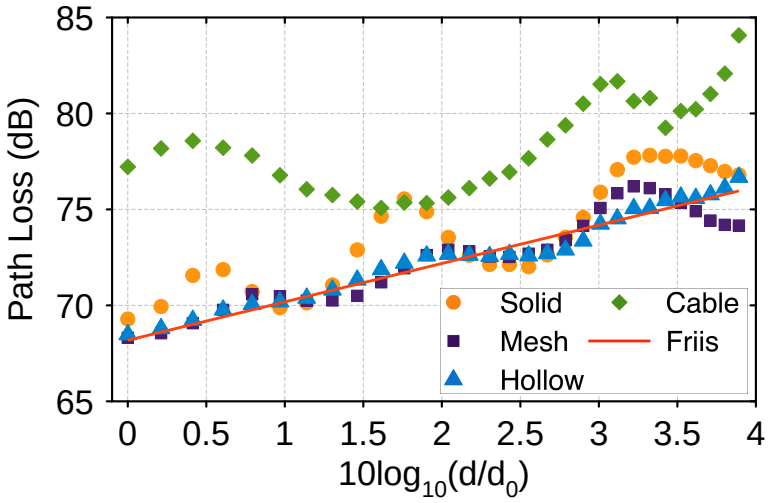

Figure 23: Friis theoretical path loss (red line) and the measured mean path loss with different vertical ground plane structures: 1) solid metal (yellow circles), 2) hollow structure (blue triangles), 3) mesh structure (purple squares), and 4) hollow structure with cables as obstruction (green diamonds) in the vertical B2B link at distance of 20–49 cm and $d_0 = 20$ cm.

at distance of 24, 32, 42 cm. In Fig. 23 (blue triangles) and Fig. 25 (a), the measured path loss curves in the B2B RNLoS link closely follow the Friis values in both distance and frequency domains. In Fig. 23 (green diamonds) and Fig. 25 (b), the measured path loss curves in the B2B ORNLoS link show that cables as obstruction can increase path loss by around 5–10 dB as compared to the B2B RNLoS link and the frequency-dependent path loss fluctuation becomes more prominent at higher frequencies. Note that path loss values in the B2B ORNLoS link in Fig. 23 (green diamonds) and Fig. 25 (b) decrease as distance increases from 24 cm (red circles in Fig. 25 (b)) to 32 cm (blue triangles in Fig. 25 (b)). This is because signals in the direct Tx-Rx path and reflected path caused by the cables arrive within the same delay bin, i.e., their time difference of arrival (or path length difference) is smaller than the minimum time domain resolution (or spatial resolution) of the measurement system, where signals add up either in-phase or out-of-phase and result in constructive or destructive interference. We have further investigated the shadowing gain (X_σ) in the B2B ORNLoS link by repeating the measurements with three cable thickness sizes and ten cable positions at distance of 20–49 cm to have enough ensemble to perform

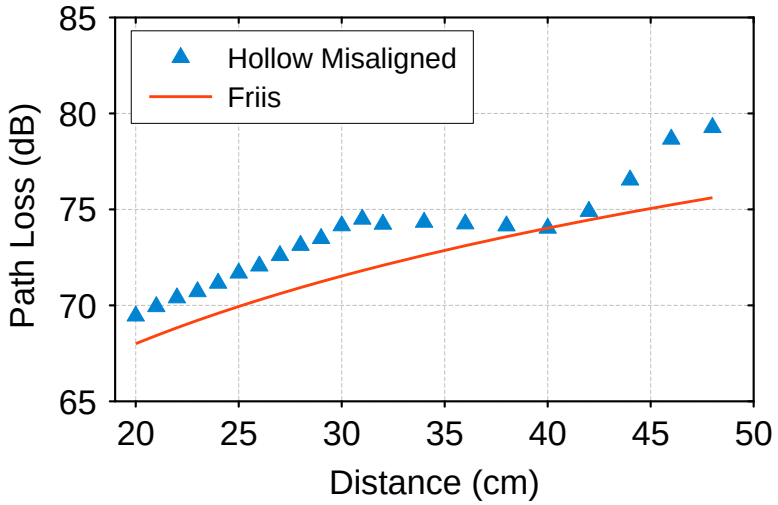

Figure 24: Friis theoretical path loss (red line) and the measured mean path loss with Rx reflector tilted (misaligned) by around 1° away from the original 45° position (blue triangles) in the vertical B2B link at distance of 20–49 cm.

a statistical evaluation. We found that the shadowing gain follows a log-normal distribution with the logarithmic equivalent having a zero-mean (in dB) and standard deviation (σ) of 3.9 dB. A CDF of X_σ for the B2B ORNLoS link is presented in Fig. 17 (c) to confirm the log-normality of the shadowing gain.

Figures 26 (a) and (b) show the measured PDPs for B2B RNLoS and B2B ORNLoS links at distance of 24, 32, 42 cm. In Fig. 26 (a), a dominant multipath cluster at around 1 ns is observed in the B2B RNLoS link, which results from multiple reflection between Tx/Rx blades since 1 ns corresponds to twice the vertical distance between two blades. In contrast, with cables as obstruction, the multipath cluster at around 1 ns is no longer observable in the B2B ORNLoS link as shown in Fig. 26 (b). In addition, the first arriving peak in Fig. 26 (b) is followed by a "long tail" over 0–0.5 ns, which is a result of multiple reflection between cables that arrives in several adjacent delay bins. A "long tail" in PDPs will generally act as interference and weaken communication performance [104].

Figure 27 shows the measured B_c for B2B RNLoS and B2B ORNLoS scenarios at distance of 20–49 cm. We can observe that as distance increases from 20 cm to 49 cm, B_c stays relatively constant at around 0.2–0.5 GHz in the ORNLoS link while decreases from

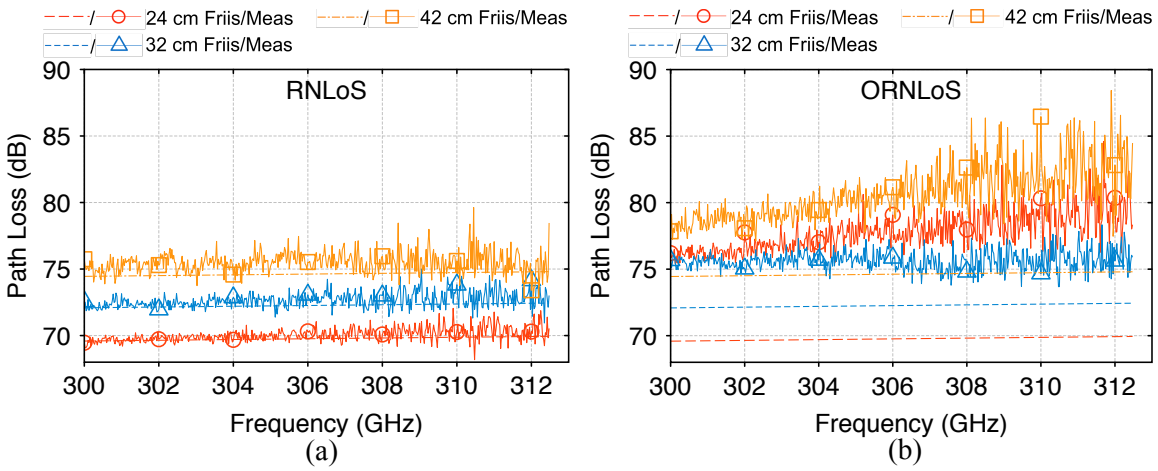

Figure 25: Measured path loss curves and Friis theoretical path loss curves in (a) B2B RNLoS and (b) B2B ORNLoS scenarios at distance of 24, 32, 42 cm.

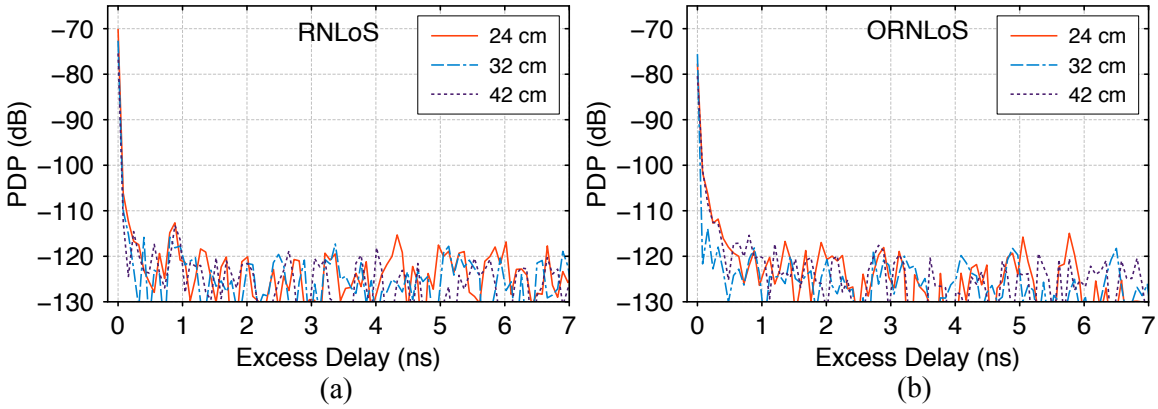

Figure 26: Measured PDPs for (a) B2B RNLoS and (b) B2B ORNLoS scenarios at distance of 24, 32, 42 cm.

around 1 GHz to around 0.4 GHz in the RNLoS link. Results imply that the B2B RNLoS link can achieve higher peak data rate as compared to the B2B ORNLoS link while the data rate in the B2B RNLoS link may fluctuate more as distance varies.

3.5.2 Characterization of B2B LoS Link

In this section, we study the relationship between Tx-Rx distance and the corresponding path loss and PDPs in the B2B LoS scenario as introduced in Fig. 7 (e) and Section 3.3.7.

Measured path loss curves and Friis theoretical path loss values for the B2B LoS link are presented in Fig. 28 (a). It can be observed that the measured path loss values closely

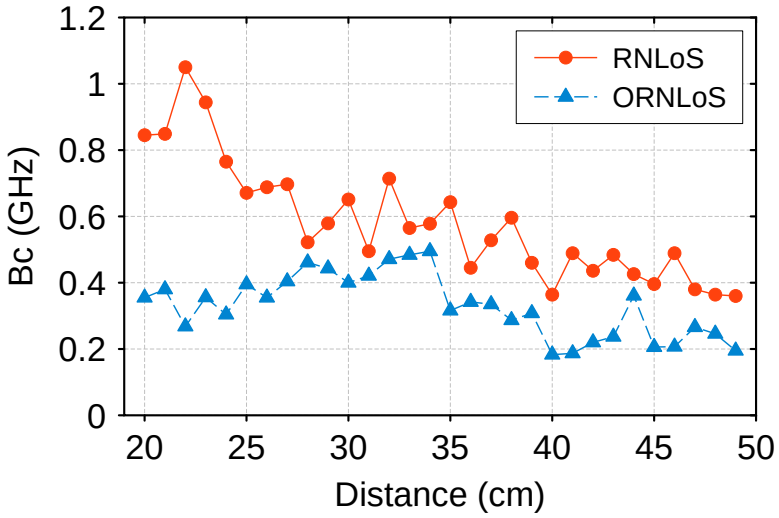

Figure 27: Measured B_c for B2B RNLoS and B2B ORNLoS scenarios at distance of 20–49 cm.

follow the theoretical values across all distances. The corresponding measured PDPs are presented in Fig. 28 (b). Although being surrounded by metal plates, there is no observable multipath cluster in the PDPs of the B2B LoS link due to very focused beamwidth at THz frequencies. In summary, the B2B LoS link is comparable to the LoS propagation in a free space. Similar measurement results can be found in [28].

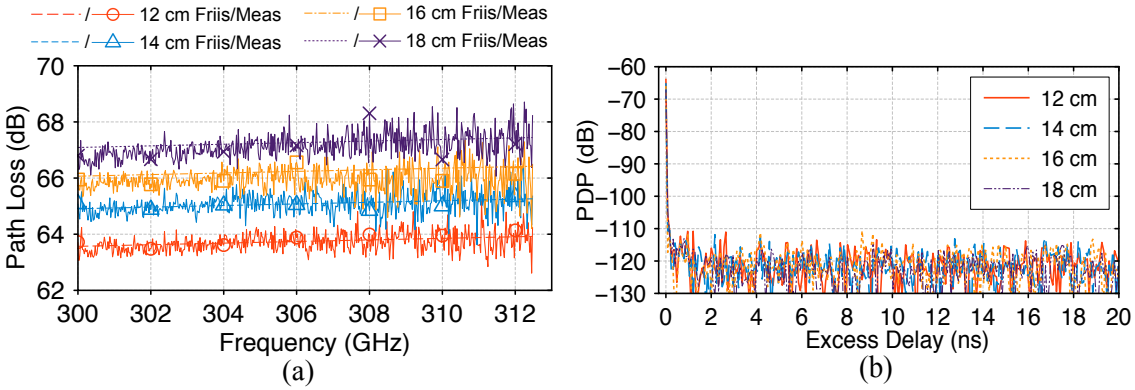

Figure 28: (a) Measured path loss curves and Friis theoretical path loss values and (b) measured PDPs for the B2B LoS scenario at distance of 12, 14, 16, 18 cm.

3.6 Modeling of Doppler Power Spectrum (DPS)

In this section, we investigate a scenario where vibration of cables caused by turbulence from the cooling airflow can lead to Doppler shift in the THz bands as shown in Fig. 9. A 2-D narrow-band geometrical model that is modified from [100] is introduced to model the corresponding Doppler power spectrum. The Doppler shift (or "spread") is important in determining the minimum signalling rate allowable for coherent demodulation and the minimum adaption rate for an adaptive receiver [97].

3.6.1 2-D Narrow-Band Geometrical Model

In Fig. 29, the two-ring model defines two rings separated by distance D, one around the Tx ($A_T^{(p)}$) with radius of R_T and the other around the Rx ($A_R^{(q)}$) with radius of R_R, along with the line-of-sight (LoS) ray, single-bounced ray at the transmit side (SBT), and single-bounced ray at the receive side (SBR). Two moving scatterers, $S_{TM}^{(k)}$, and $S_{RM}^{(l)}$, lie on the rings centered at the Tx and Rx, respectively. Both Tx and Rx are stationary while $S_{TM}^{(k)}$ and $S_{RM}^{(l)}$ are moving with relative speeds v_{TS} and v_{RS} with respect to the Tx and Rx, respectively, in the directions described by angles $\gamma_{TS}^{(k)}$ and $\gamma_{RS}^{(l)}$ relative to the x-axis, respectively. θ_T and θ_R are the half power beamwidths of the Tx and Rx antennas relative to the x-axis, respectively. $\alpha_{TM}^{(k)}$ and $\alpha_{RM}^{(l)}$ are the angle of departure and the angle of arrival from moving scatterers, respectively. ϵ_{pk}, ϵ_{kq}, ϵ_{pl}, and ϵ_{lq} are the distances $A_T^{(p)}$–$S_{TM}^{(k)}$, $S_{TM}^{(k)}$–$A_R^{(q)}$, $A_T^{(p)}$–$S_{RM}^{(l)}$, and $S_{RM}^{(l)}$–$A_R^{(q)}$, respectively. For the ease of reference, the definitions of the parameters used in the model are summarized in the second column in Table 2.

The complex impulse response of the $A_T^{(p)}$–$A_R^{(q)}$ link under narrow-band frequency-flat fading can be expressed as a superposition of LoS, SBT, and SBR rays,

$$h(t) = h^{\mathrm{LoS}}(t) + h^{\mathrm{SBT}}(t) + h^{\mathrm{SBR}}(t), \tag{15}$$

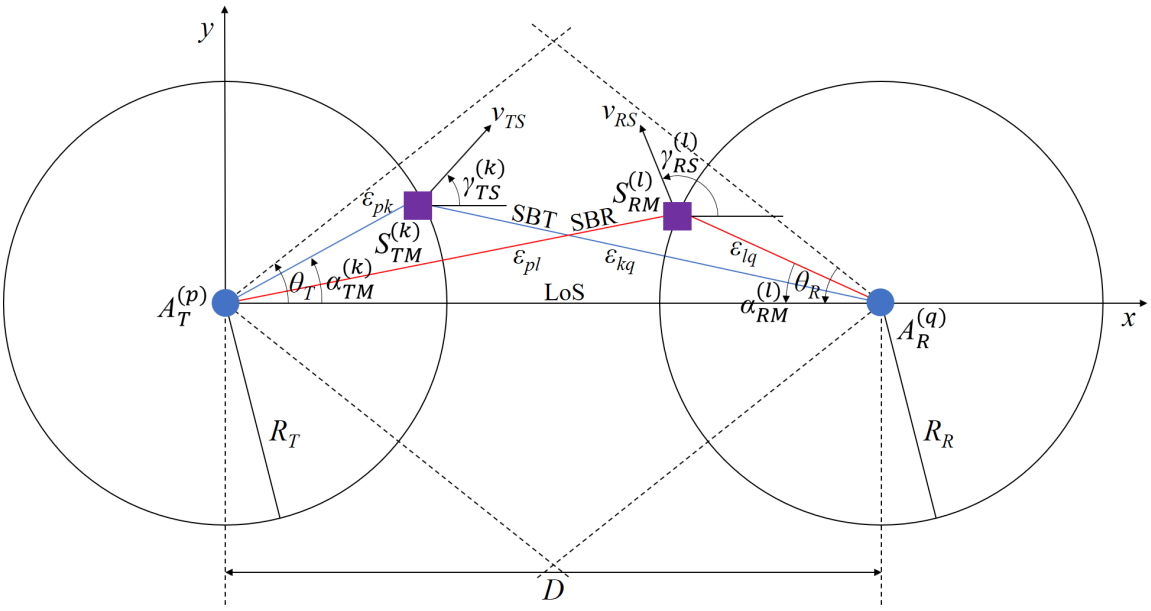

Figure 29: The two-ring model with LoS, SBT, SBR rays and moving scatterers.

where corresponding components are

$$h^{\mathrm{LoS}}(t) = \sqrt{\Omega_{pq}}\sqrt{\frac{K}{K+1}}e^{\left(j2\pi f_{pq}^{\mathrm{LoS}}t - j\frac{2\pi}{\lambda}D\right)}, \tag{16}$$

$$h^{\mathrm{SBT}}(t) = \sqrt{\Omega_{pq}}\lim_{M_M\to\infty}\sum_{k=1}^{M_M}\sqrt{\frac{\eta_{TM}}{(K+1)}}\frac{1}{\sqrt{M_M}}\cdot e^{\left(j2\pi f_k^{\mathrm{SBT}}t - j\frac{2\pi}{\lambda}(\epsilon_{pk}+\epsilon_{kq}) + j\phi_{pq,k}^{\mathrm{SBT}}\right)}, \tag{17}$$

$$h^{\mathrm{SBR}}(t) = \sqrt{\Omega_{pq}}\lim_{N_M\to\infty}\sum_{k=1}^{N_M}\sqrt{\frac{\eta_{RM}}{(K+1)}}\frac{1}{\sqrt{N_M}}\cdot e^{\left(j2\pi f_l^{\mathrm{SBR}}t - j\frac{2\pi}{\lambda}(\epsilon_{pl}+\epsilon_{lq}) + j\phi_{pq,l}^{\mathrm{SBR}}\right)}, \tag{18}$$

where K is the Rice factor, $\Omega_{pq} = (D^{-\gamma/2}\sqrt{G_T G_R}\lambda/4\pi)^2$ is the power associated with the pq^{th} path, D is the Tx-Rx distance, γ is the pathloss exponent, G_T and G_R are the gains of the transmit and receive antennas, and λ is the wavelegnth, respectively. We assume the

relative power allocated to the SBT and SBR is $\eta_{TM} + \eta_{RM} = 1$. M_M and N_M represent the number of the moving omnidirectional scatterers that lie on the Tx and Rx rings, respectively. f_{pq}^{LoS}, f_k^{SBT}, and f_l^{SBR} are the Doppler frequencies, where $f_{pq}^{\mathrm{LoS}} = 0$ given a fixed wireless communication scenario with stationary Tx and Rx, while f_k^{SBT} and f_l^{SBR} can be simplified as [100]

$$f_k^{\mathrm{SBT}} = -f_{\mathrm{TSmax}} \left[\cos\left(\alpha_{TM}^{(k)} - \gamma_{TS}^{(k)} \right) - \cos \gamma_{TS}^{(k)} \right], \tag{19}$$

$$f_l^{\mathrm{SBR}} = -f_{\mathrm{RSmax}} \left[\cos\left(\alpha_{RM}^{(l)} - \gamma_{RS}^{(l)} \right) - \cos \gamma_{RS}^{(l)} \right], \tag{20}$$

where $f_{\mathrm{TSmax}} = v_{TS}/\lambda$ and $f_{\mathrm{RSmax}} = v_{RS}/\lambda$ are the maximum Doppler frequencies associated with the moving scatterers around the Tx and Rx, respectively. Note that when the number of scatterers at the Tx and Rx, i.e., M_M and N_M, approaches infinity, random variables of $\alpha_{TM}^{(k)}$, $\alpha_{RM}^{(l)}$, $\gamma_{TS}^{(k)}$, and $\gamma_{RS}^{(l)}$ can be characterized as continuous random variables with specified PDF. We use the von Mises PDF to characterize the aforementioned parameters since it approximates various common distributions (e.g., uniform, Gaussian, Laplacian) and gives closed-form solutions for many useful situations. The von Mises PDF is defined as $p(\theta) = \exp\left[\kappa \cos(\theta - \mu)\right] / 2\pi I_0(\kappa)$ [105] where $\theta \in [-\pi, \pi)$, $I_0(\cdot)$ is the zeroth-order modified Bessel function of the first kind, $\mu \in [-\pi, \pi)$ is the mean angle where the scatterers are distributed in the x-y plane, and κ controls the spread of scatterers around the mean value. Phases $\phi_{pq,k}^{\mathrm{SBT}}$ and $\phi_{pq,l}^{\mathrm{SBR}}$ are assumed as independent random variables that are uniformly distributed on the interval $[0, 2\pi)$. Path lengths $\epsilon_{pk} = \epsilon_{lq} = \epsilon_{pl} = \epsilon_{kq} = 20$ cm.

The autocorrelation function of the narrow-band complex channel impulse response in (15) is defined as,

$$R(\Delta t) = \frac{E\left[h(t)^* \cdot h(t + \Delta t)\right]}{\sqrt{Var\left[h(t)\right] Var\left[h(t)\right]}}, \tag{21}$$

where $(\cdot)^*$ is the complex conjugate operation, $E[\cdot]$ represents the statistical expectation operator, and $Var[\cdot]$ is the statistical variance operator. Since $h^{\mathrm{LoS}}(t)$, $h^{\mathrm{SBT}}(t)$, and $h^{\mathrm{SBR}}(t)$ are independent complex Gaussian random processes, (21) can be simplified to

$$R(\Delta t) = R^{\mathrm{LoS}}(\Delta t) + R^{\mathrm{SBT}}(\Delta t) + R^{\mathrm{SBR}}(\Delta t), \tag{22}$$

where $R^{\mathrm{LoS}}(\Delta t)$, $R^{\mathrm{SBT}}(\Delta t)$, $R^{\mathrm{SBR}}(\Delta t)$ are the autocorrelation functions of the LoS, SBT, and SBR components, respectively, and can be expressed as

$$R^{\mathrm{LoS}}(\Delta t) = \frac{K}{K+1} e^{-j\frac{4\pi}{\lambda}D}, \tag{23}$$

$$R^{\mathrm{SBT}}(\Delta t) = \frac{\eta_{TM}}{K+1} \cdot \int_{0}^{2\pi} \int_{-\theta_T}^{\theta_T} e^{j2\pi f_k^{\mathrm{SBT}} \Delta t} f(\alpha_{TM}) f(\gamma_{TS}) d\alpha_{TM} d\gamma_{TS}, \tag{24}$$

$$R^{\mathrm{SBR}}(\Delta t) = \frac{\eta_{RM}}{K+1} \cdot \int_{0}^{2\pi} \int_{-\theta_R}^{\theta_R} e^{j2\pi f_l^{\mathrm{SBR}} \Delta t} f(\alpha_{RM}) f(\gamma_{RS}) d\alpha_{RM} d\gamma_{RS}, \tag{25}$$

where $f(\alpha_{TM})$ and $f(\alpha_{RM})$ are characterized as uniform random variables distributed on the interval $[-7.5^\circ, 7.5^\circ]$, while $f(\gamma_{TS})$ and $f(\gamma_{RS})$ are characterized as von Mises PDFs, i.e., $f(\gamma_{TS}) = \exp\left[\kappa \cos(\gamma_{TS} - \mu)\right] / 2\pi I_0(\kappa)$ and $f(\gamma_{RS}) = \exp\left[\kappa \cos(\gamma_{RS} - \mu)\right] / 2\pi I_0(\kappa)$, respectively. The Doppler power spectrum of the narrow-band channel impulse response can then be estimated by calculating the Fourier transform of the autocorrelation function

in (22), i.e.,

$$\begin{aligned} S(\nu) &= \mathcal{F}_{\Delta t}\{R(\Delta t)\} \\ &= \mathcal{F}_{\Delta t}\{R^{\mathrm{LoS}}(\Delta t) + R^{\mathrm{SBT}}(\Delta t) + R^{\mathrm{SBR}}(\Delta t)\}. \end{aligned} \tag{26}$$

Table 2: Definition of the Parameters Used in the 2-D Geometrical Model

Parameters	Definition	Value
D	The distance between the centers of Tx and Rx sectors.	40 cm
R_T R_R	The radius of the Tx and Rx sectors, respectively.	20 cm 20 cm
θ_T θ_R	Half power beamwidths of the Tx and Rx antennas in the x-y plane (relative to x-axis), respectively.	[-7.5º , 7.5º] [-7.5º , 7.5º]
v_{TS} v_{RS}	The relative velocities of the moving scatterers with respect to velocities of the Tx and Rx, respectively.	5.61 cm/s 5.61 cm/s
$f_{TS\,\max}$ $f_{RS\,\max}$	The maximum Doppler frequencies associated with the moving scatterers around the Tx and Rx, respectively.	56.1 Hz 56.1 Hz
$\alpha_{TM}^{(k)}$ $\alpha_{RM}^{(l)}$	The angle of departure (AoD) and the angle of arrival (AoA) from moving scatterers, respectively.	[-7.5º , 7.5º] [-7.5º , 7.5º]
$\gamma_{TS}^{(k)}$ $\gamma_{RS}^{(l)}$	The directions of moving scatterers around the Tx and Rx, respectively, in the x-y plane (relative to the x-axis).	[0 , 2π) [0 , 2π)
ε_{pk} , ε_{kq} , ε_{pl} , ε_{lq}	The distances $A_T^{(p)}$–$S_{TM}^{(k)}$, $S_{TM}^{(k)}$–$A_R^{(q)}$, $A_T^{(p)}$–$S_{RM}^{(l)}$, $S_{RM}^{(l)}$–$A_R^{(q)}$	$\varepsilon_{pk} = \varepsilon_{lq}$ = 20 cm $\varepsilon_{pl} = \varepsilon_{kq}$ = 20 cm
λ	The wavelength.	1 mm
K	The Rice factor.	5
u k	The von Mises pdf parameters: 1) u, mean angle where the scatterers are distributed in the x-y plane; 2) k, spread of scatterers around the mean.	0 0.3
η_{TM} η_{RM}	Specify how much the scattered rays from moving scatterers around the Tx and Rx contribute in the total averaged power.	0.5 0.5

3.6.2 Model Validation

To verify the geometrical model with measurements, we need to estimate the model parameters from the measured data. The relative velocities of the moving scatterers, i.e., cables, and the maximum Doppler frequencies are estimated from the spectrogram in Fig. 30, where a maximum Doppler frequency is observed as 56.1 Hz, corresponding to $v_{TS} = v_{RS} = 5.61$ cm/s. Note that the images on both sides of the carrier signal at 300 GHz are caused by sub-carrier artifacts (due to nonlinearity in the system). A zoom-in view in Fig. 30 shows that the Doppler effect on the artifact sub-carriers did not cause the inter-carrier interference. The parameters in the von Mises PDF and the Rice parameter K

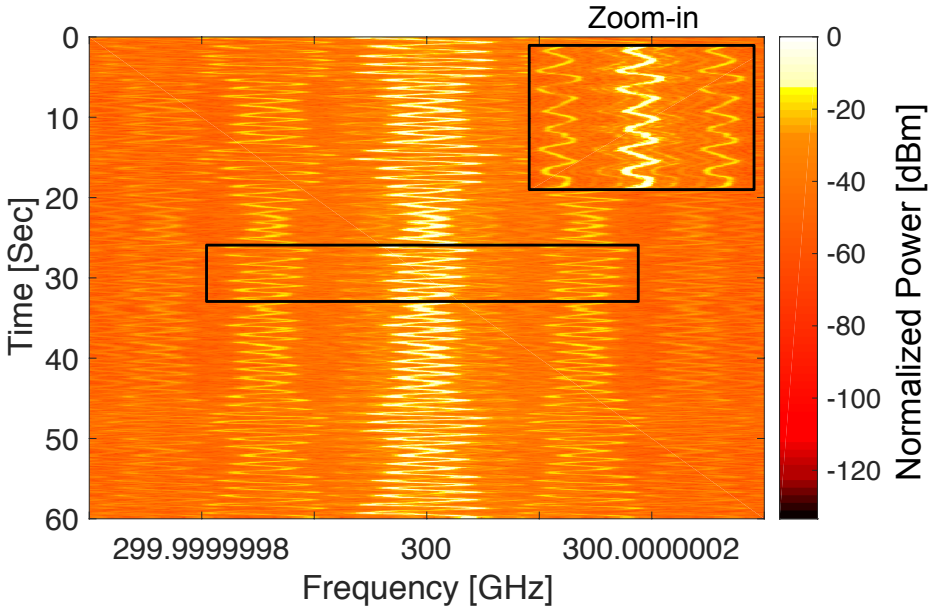

Figure 30: Spectrogram of the measured narrow-band channel impulse response at 300 GHz.

are estimated from the measured input delay-spread functions, where $(\mu, \kappa) = (0, 0.3)$ and $K = 5$, respectively. We assume $\eta_{TM} = \eta_{RM} = 0.5$. Detailed values of the parameters used in the proposed model are summarized in the third column in Table 2.

Figure 31 presents the modeled autocorrelation function, and Fig. 32 presents the measured and modeled DPS, respectively. We can observe that both the modeled and measured

DPS are similar to the "bell-shape" spectra in [97, 98, 99, 100], where both the transmitter and the receiver are stationary, and time-variations are due to the movement of the scatterers. We have also observed that the modeled DPS has a good agreement with measured data.

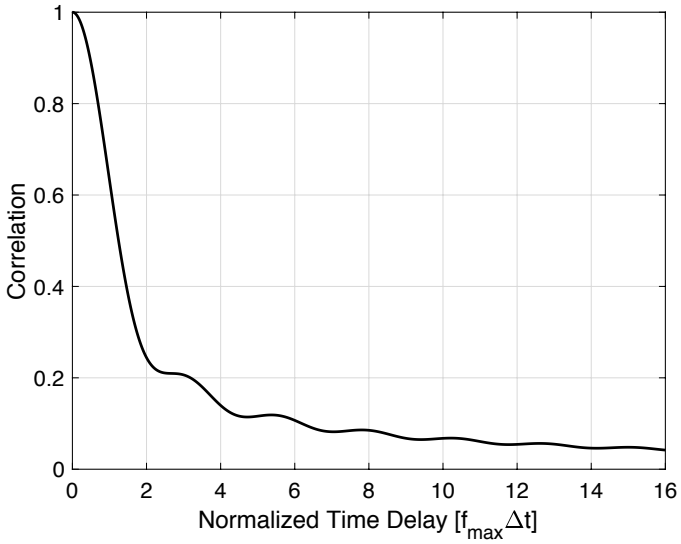

Figure 31: Modeled autocorrelation function.

3.7 Summary

This chapter presents detailed characterization of 300 GHz channels for wireless R2R and B2B communications in data centers. Measurements are conducted in R2R LoS, R2R OLoS, R2R RNLoS, R2R ORNLoS, B2B RNLoS, B2B ORNLoS, and B2B LoS scenarios, which evaluate the impact of Tx/Rx misalignment and obstructions such as cables, metal cabinets, and mesh structures on THz propagation, as well as possibility of using existing metal objects as reflectors that guide waves for NLoS type of links. For the R2R LoS scenario, the channel with optical lenses acts as a waveguide with a PLE of 1.48 and the optical lenses provide additional gain of more than 25 dB. PDPs reveal that optical lenses can cause additional multiple reflections. When obstructions of cables are present, ORNLoS link outperforms OLoS link with 2.5 dB lower shadowing gain and weaker multipath.

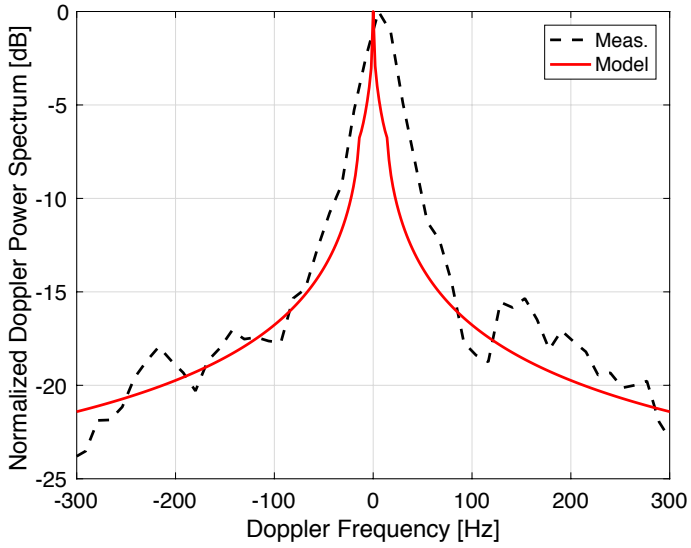

Figure 32: Measured and modeled Doppler power spectra (DPS).

For the B2B scenario, a dual-reflector THz transceiver rack system has been proposed to enable wireless links across vertically stacked servers and allow easy maintenance and repair of servers. The measured path loss approximates the Friis values in the LoS link and in the RNLoS link with the hollow vertical ground plane. A hollow rack structure is preferred over solid metal due to its minimum reflection interference. When obstructions of cables are present, the ORNLoS link experiences 5–10 dB higher path loss and on average 0.25 GHz lower B_c than the RNLoS link. Measured statistical channel properties show that the shadowing gain caused by cable clusters follows the log-normal distribution. Furthermore, Doppler shift in THz bands due to the effect of cooling airflow turbulence, which causes cables to vibrate has also been measured. A 2-D geometrical propagation model that includes moving scatterers is introduced. From the 2-D model, the corresponding DPS is derived and validated with measured data. Results show that a maximum Doppler frequency is observed as 56.1 Hz.

CHAPTER 4
CHARACTERIZATION OF 300 GHZ PROPAGATION IN A DATA CENTER ENVIRONMENT

4.1 Overview

In this section we present experimental results and channel modeling for realistic data center environment. Measurement-based work in [23] presented a THz measurement campaign conducted in a data center. Results showed that path attenuation is comparable to Friis theoretical values and that THz wireless communication in a data center is possible. However, the measurement campaign did not investigate the propagation scenario with exposed cables serving as obstruction, which have been observed in some of the existing data centers [5, 15].

Here, we present details from the THz channel measurement campaign conducted in a data center environment with consideration for propagation scenarios including line-of-sight (LoS) link, non-LoS (NLoS) link using existing materials in a data center to redirect the beam, and obstructed-LoS (OLoS), -NLoS (ONLoS) links with common objects in data centers (cables and server racks' mesh doors) serving as obstruction were investigated. Classic propagation channel parameters such as pathloss and root-mean-squared (RMS) delay spread were analyzed in the aforementioned scenarios. We find that local scattering objects such as Server-rack frames/pillars can be used to assist the NLoS type of link, and that cooling airflow in the data center has a negligible impact on THz propagation. Power cables and mesh doors of the server racks can cause additional attenuation of about 20 dB and 6 dB respectively. The statistics of amplitude fading in a 4×4 MIMO channel with cables serving as obstruction have been investigated with results showing an m-Nakagami distribution fit and a linear dependency on delay bins. Characterization results provided in

this chapter are pertinent to THz wireless system design for data center environments.

The remainder of the chapter is organized as follows. Section 4.2 presents the THz channel sounding system, antennas, and Polytetraflu-oroethylene (PTFE) optical lens configuration used in the measurement campaign. Section 4.3 describes the measurement environment and scenarios. Sections 4.4 presents the measurement and analysis results. Finally, Section 4.5 provides some concluding remarks.

4.2 Measurement Setup

The block diagram of the measurement system, measurement parameters, as well as the antennas used in this chapter are identical to those presented in Section 3.2 (Fig. 3, Fig. 4, and Table 1).

4.3 Measurement Environment

The propagation channel measurements were conducted in a data center at the Tech Way Building on the campus of the Georgia Institute of Technology, Atlanta, GA. The data center environment is unique in its densely packed compartmentalized layout where high performance computing servers with metal enclosures are vertically stacked up in metallic server racks, and rows of server racks are arranged in parallel separated by aisles. Each server rack has a movable door with mesh structure that allows for circulation of the cooling airflow. Exposed cable clusters, e.g., power cables and auxiliary cables, are observed among the server racks.

In our measurement campaign, five wireless data center scenarios have been considered: 1) LoS link, where a server from one rack communicates to the server in the next-aisle rack; 2) OLoS link, where the LoS link is obstructed by common objects in data centers, such as cables and server racks' mesh doors; 3) NLoS link, where servers in adjacent racks communicate with each other through reflection off of the Server-rack frames/pillars in the next aisle; 4) ONLoS link, where the NLoS link is obstructed by server racks' mesh doors;

5) Tx and Rx are placed at the opening of the cooling grille on the floor to study the effects of cooling airflow on THz propagation.

4.3.1 LoS Link

We envision that THz transceivers and optical lenses will eventually be integrated into the server chassis such that THz links can be established for server-to-server communications. Our measurement setup for the LoS link is presented in Fig. 33, where the Tx is placed in the server cabinet on the left side of the aisle and the Rx is placed in the server cabinet on the right side of the aisle with a Tx-Rx separation distance, d = 175 cm. We have

Figure 33: Measurement setup for the LoS link at distance of 175 cm.

also tested a scenario where misalignment exists between the Tx and Rx. In reality, each server rack may be configured for different applications using different types of servers with different heights [96]. In such case, the Tx and Rx that are integrated into the server enclosure may not be perfectly aligned in the vertical direction. Therefore, an investigation of the tolerance range of the vertical offset between the Tx and Rx is in order. A schematic of the measurement setup for the LoS link with vertical offset is presented in Fig. 34, where the vertical offset range, h, varies from 0 to 6 cm with a step size of 1 cm.

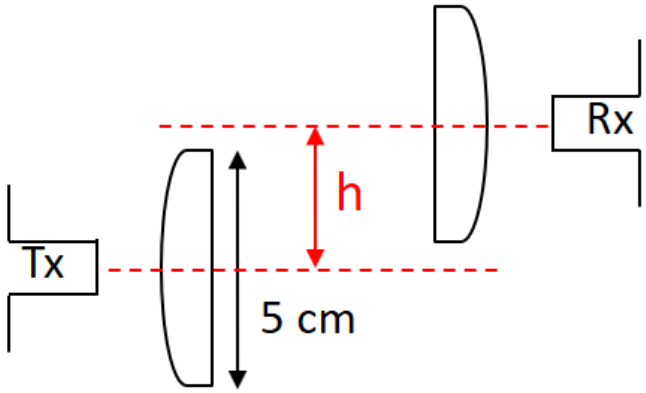

Figure 34: Illustration of the LoS vertical offset measurement setup, where h varies from 0 to 6 cm with a step size of 1 cm.

Note that several possible LoS propagation links in wireless data centers were presented in [14, Sec. II, para. 3], [23, Sec. II-B, para. 1, and Sec. II-C, para. 1],[7, Sec. II, para. 1], including links with Tx/Rx placed on top of the rack (ToR) and on the lower level of the rack. In our LoS setup, we investigate the case with Tx/Rx placed on the lower level of the rack since the ToR link has already been studied in [23, Sec. IV, para. 1], with measurement results showing a path attenuation, which followed the Friis propagation model. Moreover, according to [14, Sec. II, para. 4], by placing Tx/Rx on the lower level of the rack, interference [7, Sec. II, para. 4] from the ToR link can be avoided.

4.3.2 OLoS Link

Next, we investigate the OLoS scenario where the wireless channel is obstructed by objects commonly found in data centers such as cables and mesh doors. We envision that THz transceivers and optical lenses will be integrated into the server chassis, which implies that the mesh door on the server rack may obstruct the LoS link between the Tx and Rx. Therefore, we evaluate the impact of mesh door on THz links. For the OLoS link with mesh door serving as obstruction, measurements were recorded at distance of 175 cm with the mesh door on the Tx rack (left side in Fig. 33) closed, while the mesh door on the Rx rack (right side in Fig. 33) stayed open. A focused view of the mesh structure is shown in Fig. 35

(a). It is important to note that with the wired data links in existing data centers replaced with wireless links, the remaining power cables may serve as obstruction and interfere with the wireless propagation channels. Therefore, we intended to study the OLoS scenario with power cables serving as an obstruction. Fig. 35 (b) presents the existing power cables in a data center that we used for the OLoS scenario. It can be observed in Fig. 35 (b) that existing power cables in data centers are distributed nonuniformly, with some parts consisting of multiple cables fastened together, which create a thicker cable cluster (e.g., orange cable clusters in Fig. 35 (b)); while some other parts are formed by individual cable, which lead to a thinner and scattered cable cluster (e.g., blue and yellow cable clusters in Fig. 35 (b)). Such nonuniformly composed cable clusters create obstructions with varying thickness sizes and can cause fading in THz propagation channels. In order to obtain a generalized statistical evaluation of the fading caused by cables with various thickness sizes, we recorded the measurements as Tx and Rx are placed at 26 different horizontal positions with a step size of 0.5 cm and d = 175 cm to ensure that the interaction between THz waves and different parts of the cable clusters can be captured. An illustration of the measurement setup is presented in Fig. 36. Note that the number of Tx/Rx horizontal positions could not exceed 26 due to limited space in the server rack compartment.

4.3.3 NLoS Link

In the NLoS link, reflectors were used to redirect the the transmitted signal in order to bypass obstructions and aid transmission [6]. Previous works [7, 9, 8, 14] suggested covering the ceiling in the server room with reflective materials thereby using it as a reflector for the NLoS type of link. This approach increases cost and takes up a considerable amount of space. As an alternative, we propose the possibility of using existing objects in a data center as reflectors for the NLoS link. Our setup for the NLoS link is presented in Figs. 37 (a) and (b), where the Server-rack frame/pillar of the server rack is used as the reflector. Measurements were recorded at a path length of 282 cm.

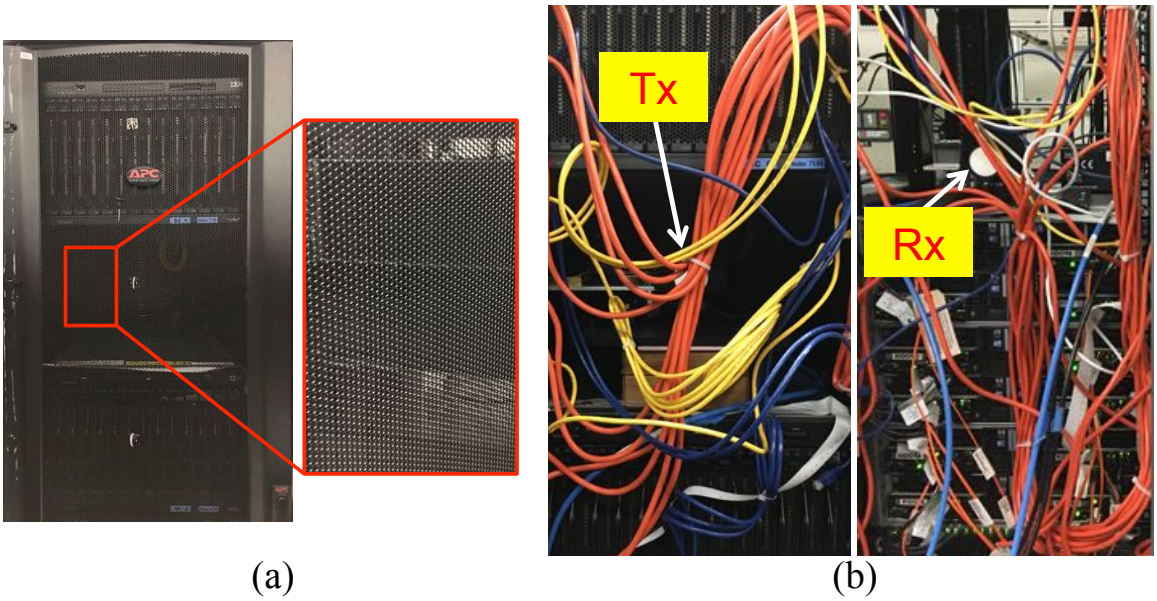

Figure 35: (a) Mesh structure on a server rack door and (b) the cable clusters at the Tx and Rx.

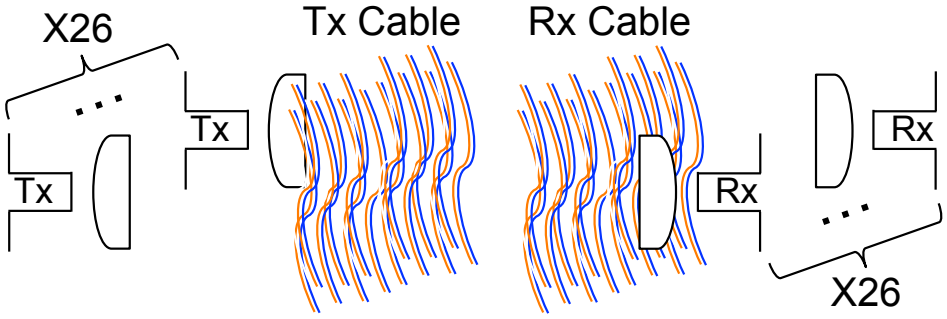

Figure 36: Illustration of the OLoS link with cables serving as obstruction. The step size between each Tx/Rx position is 0.5 cm.

4.3.4 ONLoS Link

The ONLoS scenario was also investigated, where the NLoS link introduced in Section 4.3.3 is obstructed by the mesh door on the server rack. Similar to the setup in Fig. 37 (b), here we close the mesh door on the Tx rack while leave the mesh door on the Rx rack open. Measurements were recorded at a path length of 282 cm.

Figure 37: (a) The Server-rack frame/pillar that is used as a reflector; (b) measurement setup for the NLoS link at a path length of 282 cm.

4.3.5 Effects of Cooling Airflow on THz Propagation

THz propagation encounters frequency- and moisture-dependent amplitude variation due to the molecular absorption (mainly related to an outdoor environment) at the THz bands [67]. In a data center, strong airflow from the cooling grille creates abrupt motion change to the movement of the air molecules. We investigate the cooling airflow effect on THz propagation due to the abrupt molecular movement around the cooling grille. Fig. 38 (a) presents the top-down view of the cooling grille used for our measurements. Figs. 38 (b) and (c) show the side-view of our measurement setup with cooling airflow passing through the grille and being blocked, respectively. The zero-span mode (single-frequency mode runs over time) in the VNA was used to record signal amplitude variation over time at 300 GHz with d = 9 cm. We use a 30 cm (width) x 15 cm (length) styrofoam board to block the airflow. To verify whether the airflow was really blocked by the styrofoam board, we held a piece of tissue paper on top of the styrofoam board and used visual inspection to examine whether the tissue paper was moved by the airflow. The tissue paper was observed to be stationary, and thus confirmed that the styrofoam board effectively blocked the airflow. Note that in order to have a fair comparison, we made sure that during the transition between setups in Figs. 38 (b) and (c), only the styrofoam board that blocked the airflow

was moved while the Tx/Rx alignment remained unchanged.

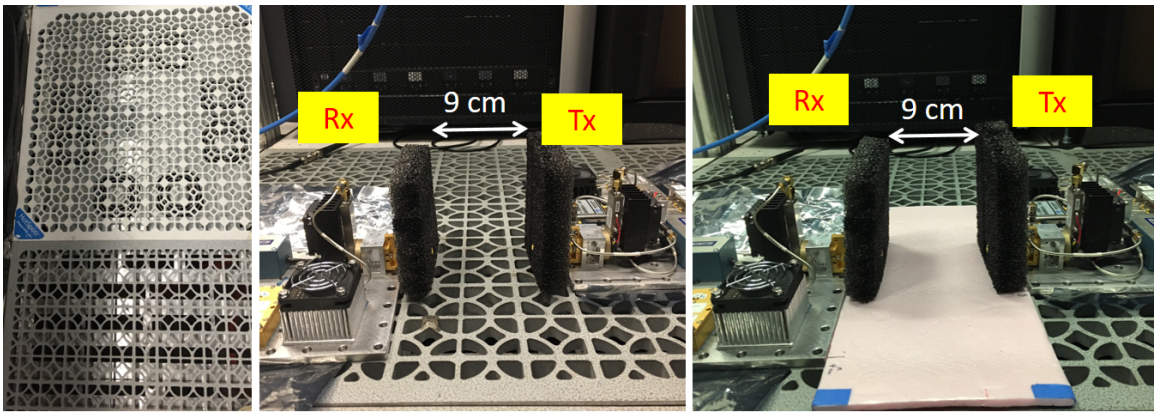

Figure 38: (a) Top-down view of the cooling grille in a data center; side-view of the measurement setup with cooling airflow (b) passing through and (c) being blocked.

4.3.6 4×4 MIMO Channel With Cables Serving as Obstruction

THz signals are suitable for short-range point-to-point communication [21], which can be established between adjacent server racks in a data center as shown in Fig. 39 (a). In such cases, clusters of power cables could serve as obstruction blocking the line-of-sight (LoS) link between the Tx and Rx. Towards diversity reasons, we conduct measurements using a 4×4 *virtual* MIMO uniform linear array (ULA) configuration [106] with 1 mm step size between antenna array elements to achieve 16 channel realizations at Tx-Rx separation, d $=$ 15 cm as illustrated in Fig. 39 (b). Five cable clusters with different thickness sizes were used to serve as obstruction to create an ensemble of shadowing positions. In this scenario, the surrounding environment mostly consists of metal structures of the server racks.

4.4 Measurement Analysis and Results

4.4.1 LoS Link Analysis

In this section, we characterize pathloss, PDP, and τ_{rms} in the LoS scenario as introduced in Fig. 33 in Section 4.3.1.

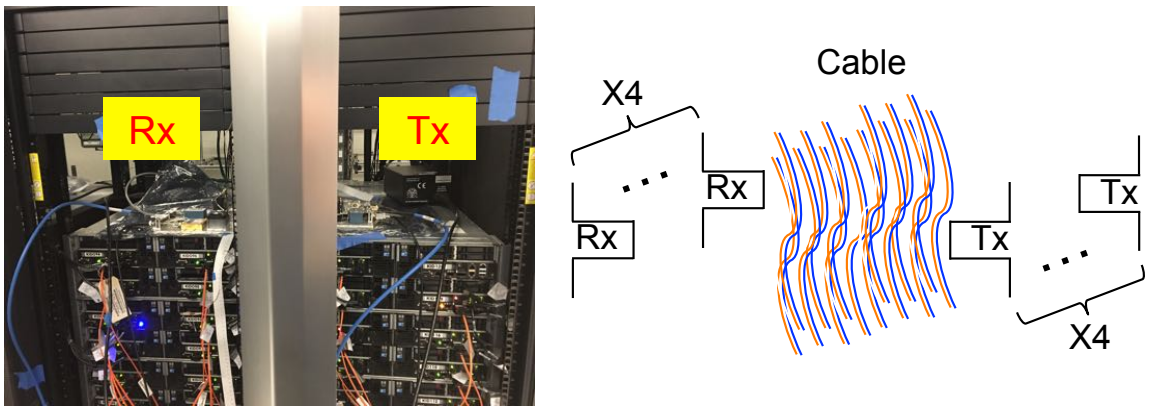

Figure 39: (a) Measurement setup and (b) illustration for the 4×4 MIMO channel with cables serving as obstruction.

The empirical and analytic (from Friis equation) pathloss results have been provided in Fig. 40. By comparing the Friis pathloss curve (black dash line with average loss = 87 dB) and the measured LoS pathloss curve (red diamond in with average loss = 57.7 dB), we find that the optical lens does provide an additional gain of around 29.3 dB by focusing the THz signal. Fig. 41 (red solid line) shows the measured PDP in the LoS link, where three distinctive MPCs were observed as labeled. A representation of the measured PDP has been provided in Fig. 41. Three distinct multipath components observed in this type of scenario have been labeled in the plot. The origin of these multipath components are subsequently discussed. MPC1 results from the sum of reflections between the lens and the horn at both Tx and Rx, where reflection at each end has a time delay of 0.4 ns. The sum of time delay at both Tx and Rx results in a total time delay of 0.8 ns. For the reflections between the lens and the horn at either Tx or Rx, the corresponding MPC is observed as unresolvable congested spikes at 0.4 ns (highlighted in blue circle in Fig. 41) due to limited temporal resolution. MPC2 results from reflections between Tx lens and Rx horn and between Rx lens and Tx horn. To be more specific, MPC2 has a delay of about 11.4 ns corresponding to an additional delay path of 342 cm that is twice the distance from the Rx horn to the Tx lens plus multiple reflected paths within the Rx lens. MPC3 is due

to Rx horn-to-Tx horn reflection. To be more specific, MPC3 has a delay around 12 ns corresponding to an additional delay path of 360 cm that is twice the distance from the Tx horn to the Rx horn plus multiple reflected paths within the Tx and Rx lenses. Since the area surrounding the Tx and Rx horns are covered with absorbers as shown in Figs. 3 (a) and (b), we can infer that the internal surfaces and the tips of the horns are the cause of horn-related reflections. The corresponding τ_{rms} in the LoS link is estimated as 0.295 ns. For ease of reference, measured mean pathloss and τ_{rms} in the LoS link are summarized in the first row in Table 3.

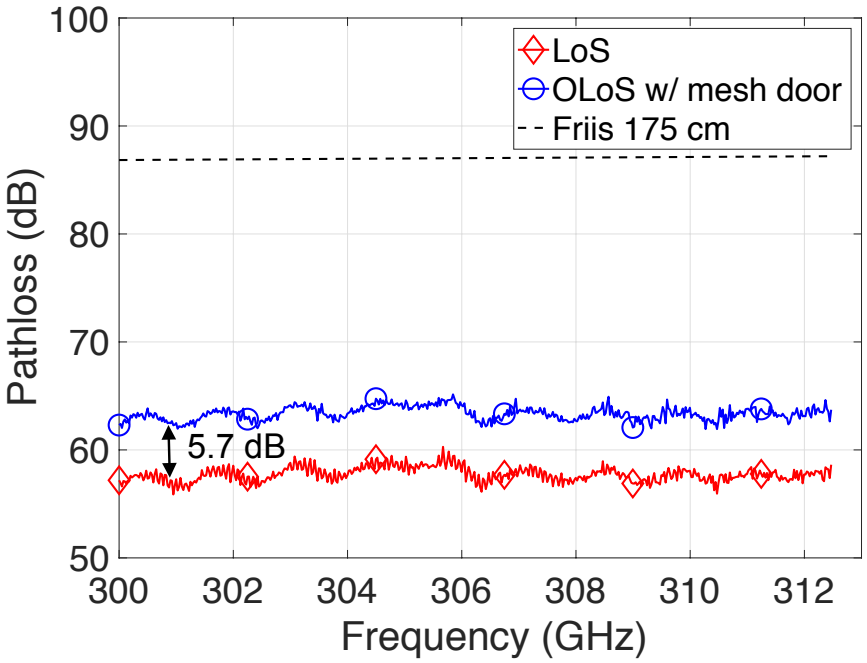

Figure 40: Measured pathloss in the LoS (red diamond) and OLoS (blue circle) links at distance of 175 cm along with Friis pathloss (black dash line) at distance of 175 cm.

Next, the LoS scenario with vertical offset between the Tx and Rx was investigated. The setup used for this measurement has been illustrated in Fig. 34, where the vertical offset range, h, varies from 0 to 6 cm with a step size of 1 cm. Fig. 42 shows the measured pathloss over frequency with various Tx-Rx offset values. It can be observed that as the offset approaches 6 cm, the pathloss value gradually increases and the fluctuation becomes more prominent. The pathloss fluctuation results from the fact that the received signal is

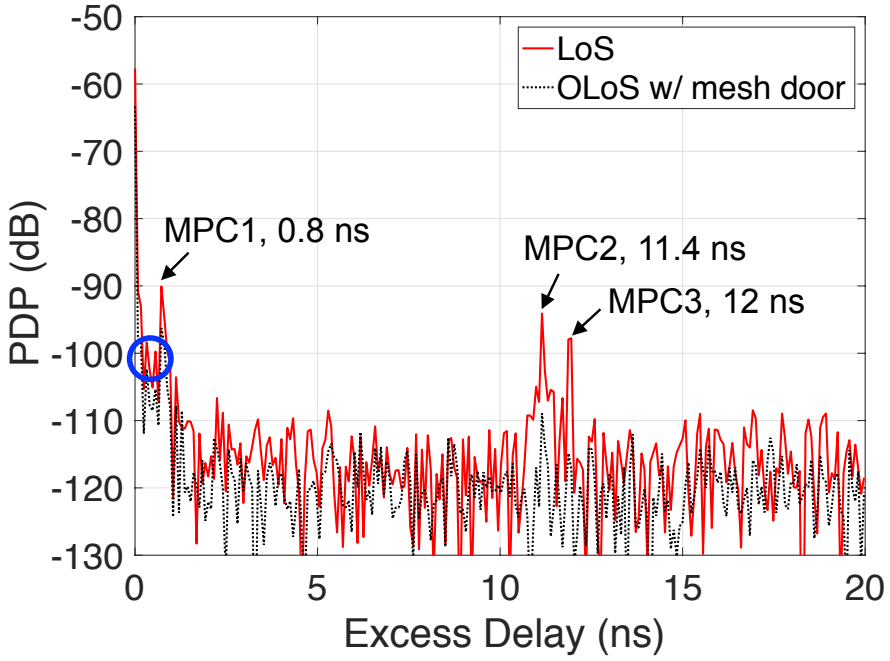

Figure 41: Measured PDP in the LoS (red solid line) and OLoS (black dot line) links at distance of 175 cm.

Table 3: Measured Mean Pathloss and τ_{rms}

Scenario		**Distance**	**Pathloss**	$\boldsymbol{\tau_{rms}}$
LoS	Door open	175 cm	57.7 dB	0.295 ns
OLoS	Door closed		63.4 dB	0.113 ns
NLoS	Door open	282 cm	78.4 dB	0.372 ns
ONLoS	Door closed		84.4 dB	0.299 ns

approaching the noise floor. Note that when offset exceeds 6 cm, there is no signal reception but only a noise floor is observed. Similar observation of the pathloss fluctuation in the THz bands can be found in [25]. Fig. 43 presents the measured mean pathloss (red solid line) and the measured τ_{rms} (black dash line) with respect to Tx-Rx offset values. It can be observed in the offset range of 0–4 cm, the measured mean pathloss has an increment of 6.1 dB from 57.7 dB to 63.8 dB, while in the offset range of 4–6 cm, the pathloss has a more rapid increment of 23.6 dB from 63.8 dB to 87.4 dB. Following similar trend, τ_{rms} varies between 0.12–0.3 ns in the offset range of 0–4 cm, and 0.15–1 ns in the offset range of 4–6

cm, respectively. Coincidentally, the breakpoint around 4 cm approximates the lens diameter of 5 cm, which is reasonable since a discontinuity of propagation channel properties can be expected when the Tx-Rx misalignment exceeds the aperture size. As a result, more abrupt change in the pathloss and τ_{rms} should be expected when the Tx-Rx misalignment approaches the boundary of the lens. Note that if we look into the τ_{rms} curve in Fig. 43 during the offset distance of 0–4 cm, we can find that τ_{rms} first decreases about 0.2 ns during an offset range of 0–2 cm, and then starts to increase during an offset range of 2–4 cm. This is because during an offset range of 0–2 cm, multipaths mainly come from the reflections between the lenses and horn antennas as explained in the previous paragraph. As an offset increases from 0 cm, the aforementioned reflections start to attenuate due to the Tx/Rx misalignment, and thus result in decreased τ_{rms}. In the offset range of 2–4 cm, reflection from the surrounding environment (e.g., server enclosures and rack compartments) leads to a wider MPC as shown in Fig. 44 and thus slightly increases the τ_{rms}. As an offset distance increases beyond 4 cm, the main cause of rapid increase in the τ_{rms} is dominated by the attenuation of the first arrival path, which causes τ_{rms} to increase according to (5).

4.4.2 OLoS Link Analysis

In this section, we characterize the pathloss, PDP, and τ_{rms} in the OLoS scenario as introduced in Section 4.3.2.

Figure 40 (blue circle) shows the measured pathloss in the OLoS link with a mesh door serving as an obstruction. The measured mean pathloss is calculated as 63.4 dB. By comparing the mean pathloss in the LoS link and OLoS link, we can conclude that the additional loss resulting from the mesh door is around 5.7 dB. Fig. 41 shows the measured PDP in the OLoS link, with the corresponding τ_{rms} estimated as 0.113 ns. Interestingly, the PDP showed that with the obstruction of the mesh door, multipaths are significantly attenuated compared to the LoS link, and that the τ_{rms} is reduced from 0.295 ns to 0.113 ns. For ease of reference, measured mean pathloss and τ_{rms} in the OLoS link with the mesh

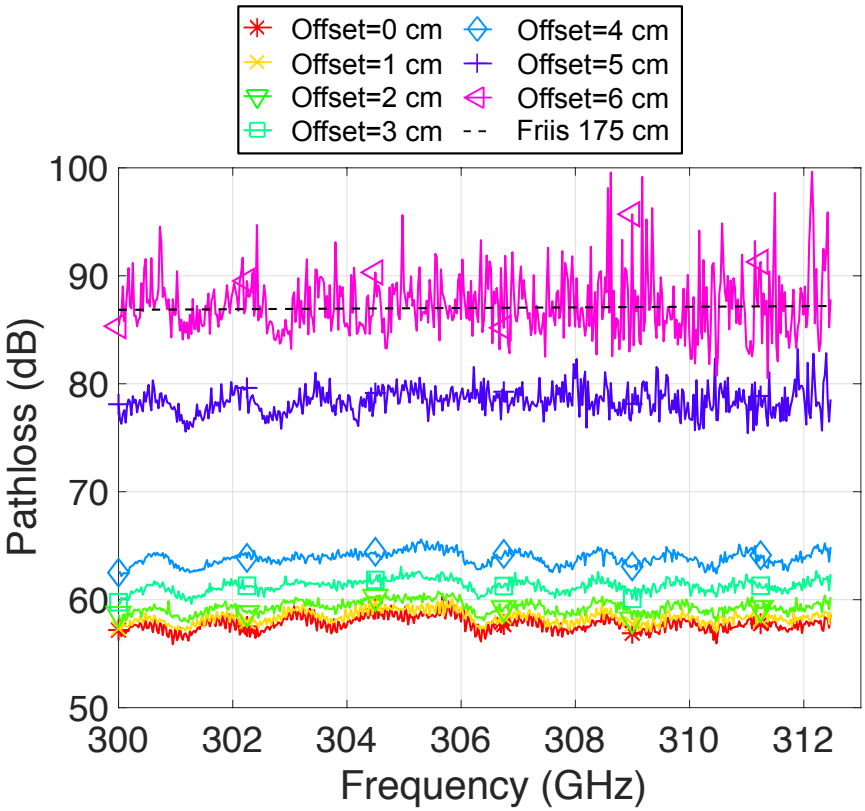

Figure 42: Measured pathloss and Friis pathloss (black dash line) in the LoS link at distance of 175 cm with Tx-Rx vertical offset varying from 0 to 6 cm.

door serving as obstruction are summarized in the second row in Table 3.

As explained in Section 4.3.2, cable clusters used in the OLoS link are distributed nonuniformly with irregular shapes and various thickness sizes. This cable composition in the OLoS propagation channel can eventually lead to small-scale fading. Figs. 45 and 46 present the measured pathloss and PDP in the OLoS link at distance of 175 cm with cables serving as obstruction, where variations in pathloss and multipath distribution (highlighted in Fig. 46) that are dependent on the Tx/Rx horizontal positions with respect to the cable clusters were observed.

4.4.3 NLoS Link Analysis

In this section, we analyze the pathloss, PDP, and τ_{rms} in the NLoS link as introduced in Fig. 37 in Section 4.3.3.

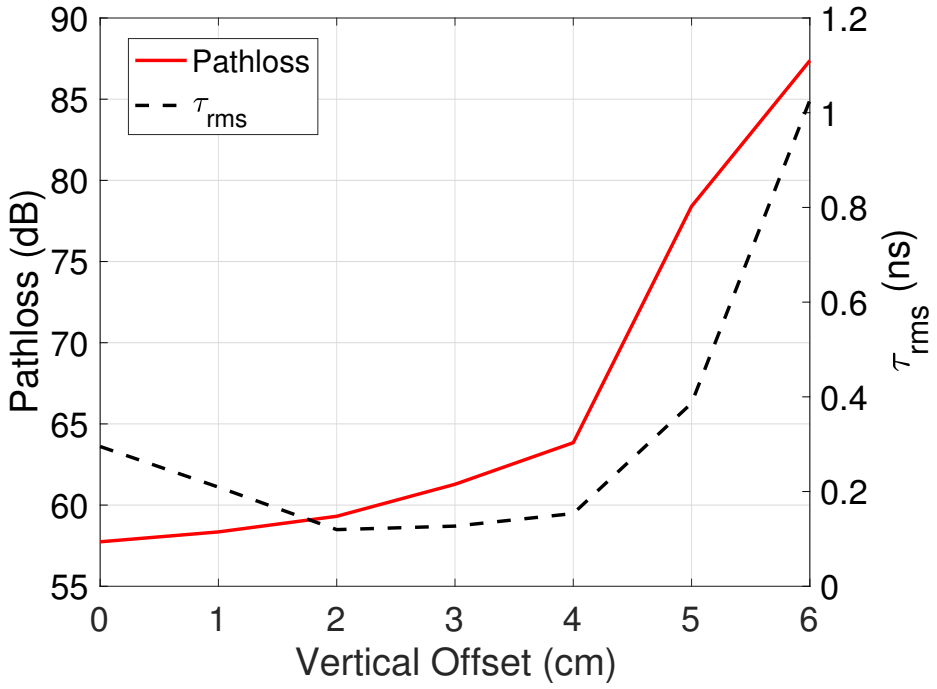

Figure 43: Measured mean pathloss (red solid line) and measured τ_{rms} (black dash line) versus Tx-Rx offset values in the LoS link at distance of 175 cm.

Figure 47 (red diamond) presents the measured pathloss in the NLoS link with Server-rack frames/pillars serving as reflector. We found that the measured mean pathloss (averaged over all frequencies), 78.4 dB, is 12.6 dB lower than the mean Friis pathloss (averaged over all frequencies), 91 dB, at a path length of 282 cm. Therefore, we conclude that in the absence of a LOS link between Tx and Rx, an alternate mean of transmission would be to use local scatterers (such as the Server-rack frames/pillars) as reflectors to aid transmission between Tx and Rx. Fig. 48 (red solid line) shows the measured PDP in the NLoS link, where two distinctive MPCs were observed as labeled. MPC1 results from reflections between Tx lens and Tx horn and between Rx lens and Rx horn, where a time delay of 0.8 ns corresponds to four times of lens-to-horn distance. Note that the MPC1 in the NLoS link has similar delay as the MPC1 in the LoS link shown in Fig. 41 (red curve), while the amplitude of NLoS link's MPC1 is weaker due to longer propagation path. MPC2 results from reflections between the Server-rack frame/pillar and the rack door that lies between the Tx

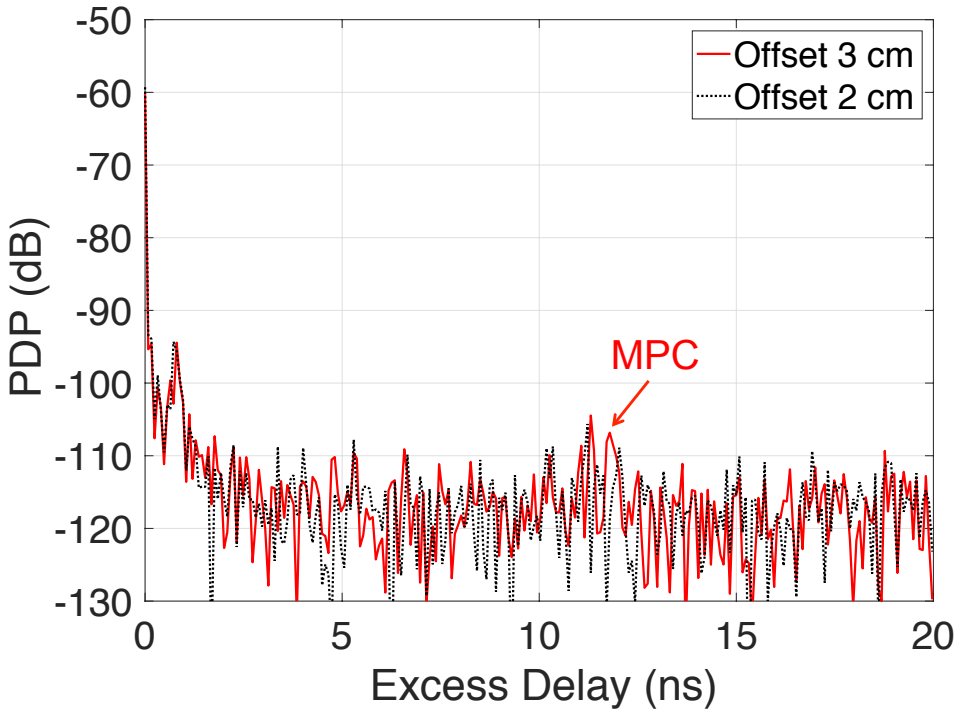

Figure 44: Measured PDP in the LoS link at distance of 175 cm with Tx-Rx vertical offset of 2 cm (black dash line) and 3 cm (red solid line).

and Rx. To be more specific, MPC2 has a delay of about 6.7 ns corresponding to an additional delay path of 200 cm that is twice the distance from the rack Server-rack frame/pillar to the rack door. This result points out that although the Server-rack frame/pillar can serve as an ideal reflector, it may also create additional scattered beams in the surrounding space and cause additional multipaths. The corresponding τ_{rms} in the NLoS link is estimated as 0.372 ns. For ease of reference, measured mean pathloss and τ_{rms} in the NLoS link are summarized in the third row in Table 3.

4.4.4 ONLoS Link Analysis

In this section, we characterize the pathloss, PDP, and τ_{rms} in the ONLoS scenario as introduced in Section 4.3.4.

In Fig. 47, the measured pathloss in the ONLoS link with mesh door serving as obstruction, where the mean pathloss is estimated as 84.4 dB, has been presented. By comparing

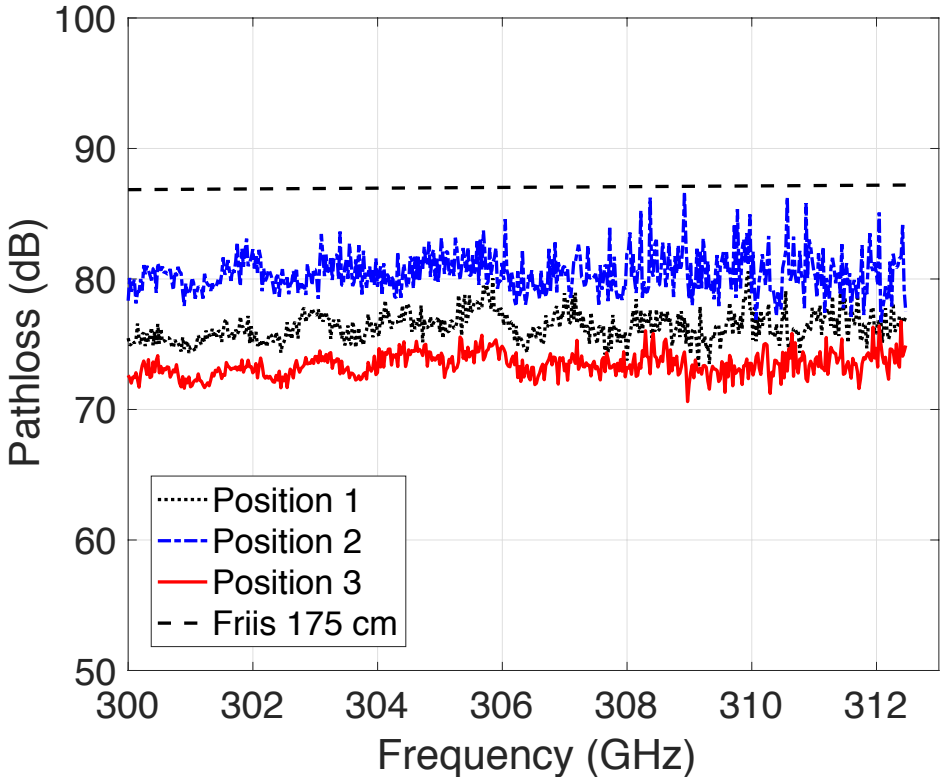

Figure 45: Measured pathloss and Friis pathloss (black dash line) in the OLoS link at distance of 175 cm with cables serving as obstruction.

the mean pathloss in the NLoS link and ONLoS link, we found that the additional loss resulting from the mesh door is around 6 dB, which is similar to the result in Section 4.3.2. Fig. 48 shows the measured PDP in the ONLoS link. Similar to the result in Section 4.3.2, MPCs are found to be attenuated by the obstruction of a mesh door. Compared to the NLoS link, the τ_{rms} in the ONLoS link is reduced from 0.372 ns to 0.299 ns. For ease of reference, measured mean pathloss and τ_{rms} in the ONLoS link are summarized in the fourth row in Table 3.

4.4.5 Effects of Cooling Airflow on THz Propagation

In this section, we investigate the impact of cooling airflow on THz propagation as introduced in Section 4.3.5. Fig. 49 presents the time domain measurement results using a 300 GHz carrier frequency with Tx-Rx separation distance of 9 cm. The average (ensemble

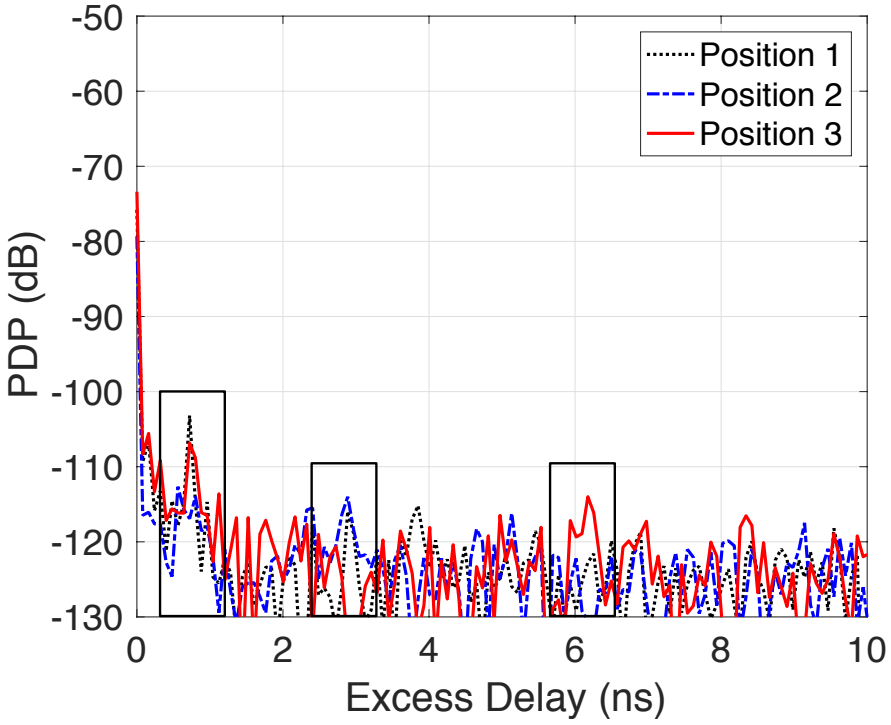

Figure 46: Measured PDP in the OLoS link at distance of 175 cm with cables serving as obstruction.

over time) magnitude of the transfer function of the channel with (blue circle) and without (red diamond) cooling airflow is -51.61 dB and -51.63 dB, respectively, with a 0.02 dB difference. As a result, we conclude that the impact from the cooling airflow is negligible. Note that the lens wasn't used for this measurement due to a short Tx-Rx distance as shown in Fig. 38.

4.4.6 Amplitude Fading Statistics of the 4×4 MIMO Channel With Cables Serving as Obstruction

We characterize the signal's amplitude fading statistics in a 4×4 MIMO channel with stationary cables serving as obstruction in the propagation channel as introduced in Figs. 39 (a) and (b). We have found that the distribution of the signal amplitude fading can be modeled by m-Nakagami distribution, where the m-parameter in dB can be modeled as a truncated Gaussian distribution denoted by m– $(T_N(\mu_m(dB), \sigma_m^2(dB))$ with a CDF shown

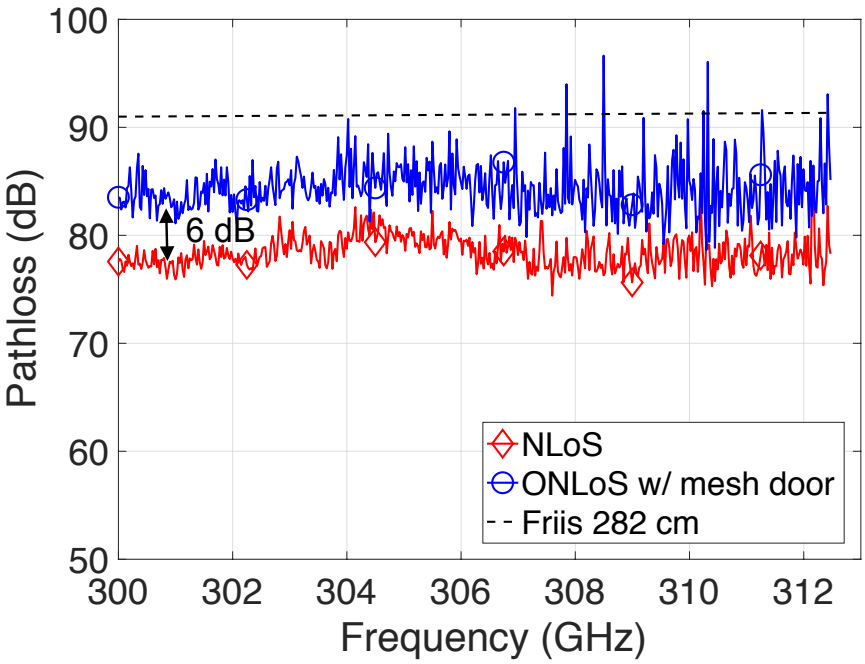

Figure 47: Measured pathloss in the NLoS (red diamond) and ONLoS (blue circle) links along with Friis pathloss (black dash line) at a path length of 282 cm.

in Fig. 50. The mean (μ_m) and standard deviation (σ_m) of the m-parameter have also been modeled as a function of the delay bin (τ_k) of the PDP at each shadowing point, which can be expressed as

$$\mu_m(\tau_k) = A - \frac{1}{B}\tau_k, \tag{27}$$

$$\sigma_m(\tau_k) = C - \frac{1}{D}\tau_k, \tag{28}$$

where the unit of τ_k is in nanosecond. Linear fit results are shown in Fig. 51, and the corresponding values of slope and intercept are stated in Table 4.

Table 4: Signal Amplitude Statistics

Scenario	A	B	C	D
4X4 MIMO	1.22	429.8	0.44	197.9

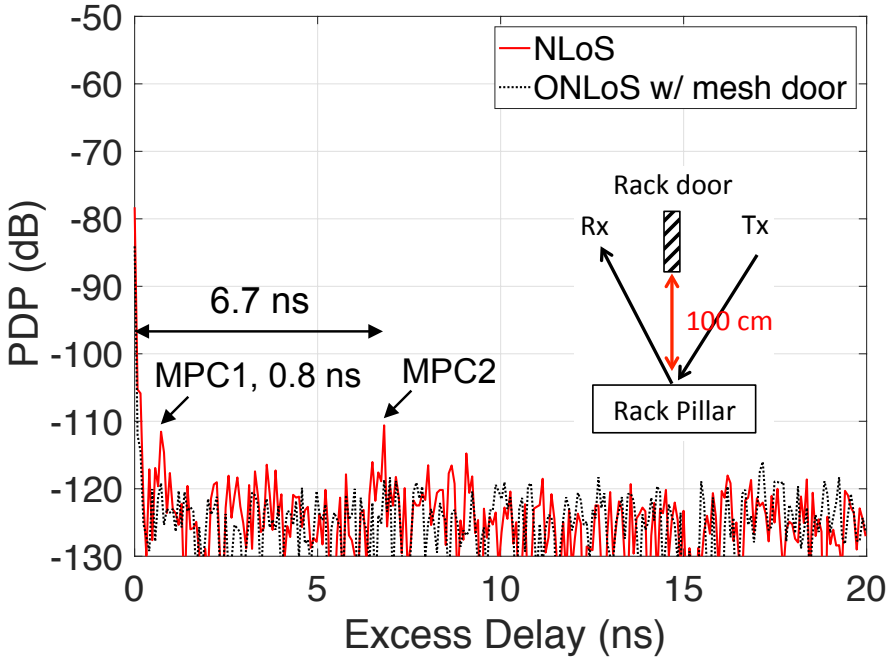

Figure 48: Measured PDP in the NLoS (red solid line) and ONLoS (black dot line) links at a path length of 282 cm.

4.5 Summary

This chapter presents a THz channel measurement campaign conducted in a data center environment and its corresponding results. Various propagation scenarios such as LoS, NLoS, OLoS, and ONLoS links have been studied. Channel properties such as pathloss, PDP, and delay spread have been analyzed. We found that optical lenses can provide additional gain of 29.3 dB in the LoS link at distance of 175 cm, and 12.6 dB in the NLoS link at a path length of 282 cm, respectively. We also found that cables and mesh structure can cause additional attenuation of about 20 dB and 6 dB, respectively. Existing objects in data centers, e.g., Server-rack frames/pillars, serve as ideal reflectors for the NLoS type of link. Furthermore, the Tx/Rx misalignment tolerance range is found to approximate the diameter of the lens, and the impact of cooling airflow on THz propagation can be overlooked. The statistics of amplitude fading in a 4×4 MIMO channel have been investigated with results showing an m-Nakagami distribution fit and a linear dependency on delay bins.

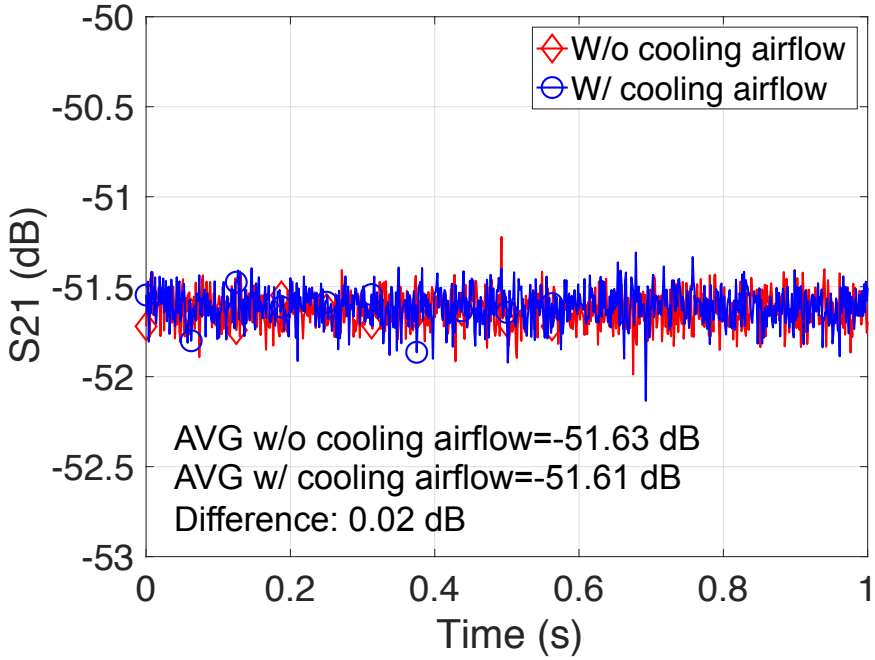

Figure 49: Magnitude of the transfer function of the channel with cooling airflow passing through (blue circle) and being blocked (red diamond). Measurements were recorded over time at 300 GHz at distance of 9 cm.

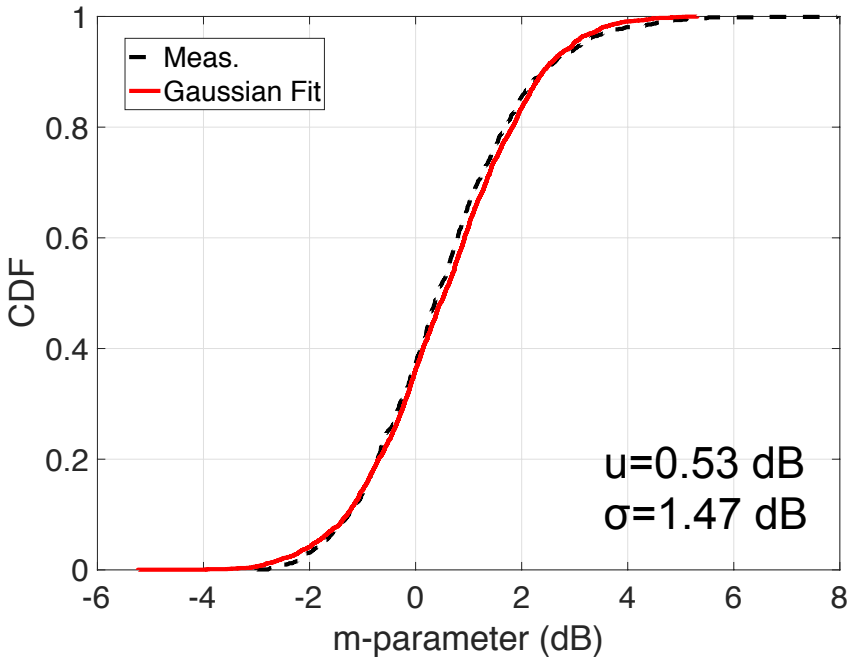

Figure 50: CDF of the m-parameter (dB) using an ensemble of shadowing points.

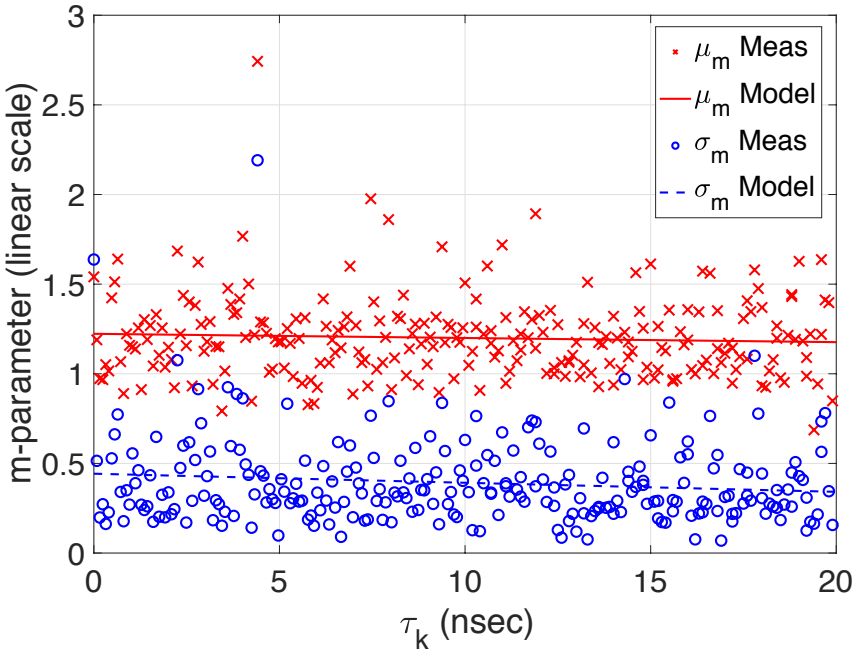

Figure 51: Linear model for the mean (μ_m) and standard deviation (σ_m) of the m-parameter as a function of delay bin (τ_k).

CHAPTER 5
CLUSTER-BASED MODELING FOR 300 GHZ PROPAGATION IN A DATA CENTER ENVIRONMENT

5.1 Overview

In measurement results presented in Chapter 4, we can observe that multipath components (MPCs) naturally group into clusters in some of the measurements conducted. Therefore, a cluster-based propagation model for THz propagation in a data center environment has been proposed in such scenarios. Cluster-based models have been widely used for indoor propagation channels across a wide range of frequency spectra, from microwave (cellular), ultra-wideband (UWB), mm-wave, up to THz bands [30, 31, 32, 33, 34, 35, 36, 37, 38, 39]. Clustering in the delay domain directly affects the delay spread, which is important in determining the need for employing channel protection techniques, e.g., channel equalization, channel coding, or channel diversity to overcome the dispersive effects of multipaths [40]. Regardless of such wide applicability and the aforementioned importance, no cluster-based model has been developed for THz propagation channels in data center environments.

This chapter introduces a statistical clustering model for THz propagation in a data center environment. The proposed model was validated with the measured data. The average inter-arrival time of clusters ($1/\Lambda$) and rays ($1/\lambda$) are estimated as 4.4 ns and 0.24 ns, respectively. Cluster modeling results provided in this chapter are pertinent to THz wireless system design for data center environments.

The remainder of the chapter is organized as follows. Section 5.2 presents the THz channel sounding system, antennas, and Polytetraflu-oroethylene (PTFE) optical lens configuration used in the measurement campaign. Section 5.3 describes the measurement environment and scenarios. Sections 5.4 describes the cluster-based model and the validation

results. Finally, Section 5.5 provides some concluding remarks.

5.2 Measurement Setup

The block diagram of the measurement system, measurement parameters, as well as the antennas used in this chapter are identical to those presented in Section 3.2 (Fig. 3, Fig. 4, and Table 1).

5.3 Measurement Environment

For the development of clustering model for a data center environment, the measurement environment and scenario can be found in Section 4.3.2, Section 4.3.3, and Section 4.3.4.

5.4 Cluster-Based Modeling of PDP

In this section, we introduce a cluster-based channel model that can handle THz propagation in a data center environment. We define a cluster as a group of MPCs having similar properties such as delays. Clusters primarily stem from interacting objects (or scatterers) such as obstructing cables, metallic shelves and doors in the data center environment. We use the K-power means clustering algorithm [35, 107] along with visual inspection [108, 109, 110] to obtain a reasonable number of clusters. Relevant channel statistics derived from the clustering model are discussed, and model validation is presented.

5.4.1 Proposed Statistical Clustering Model

The proposed clustering model in this work is based on a modified version of the widely-used Saleh-Valenzuela (S-V) model [30]. The assumption of the S-V model for the PDP is that MPCs arrive within several distinctly recognizable clusters. The PDP of the S-V

model in dB can be expressed as [62],

$$\mathrm{PDP}(\tau) = \sum_{l=1}^{L}\sum_{k=1}^{K_l}\Bigg[10\log_{10}\overline{\beta_{11}^2} - \overbrace{\frac{T_l}{\Gamma}(10\log_{10}e)}^{\mathrm{P}(T_l)} - \overbrace{\frac{\tau_{kl}}{\gamma}(10\log_{10}e)}^{\mathrm{P}(\tau_{kl})}\Bigg]\cdot\delta(\tau - T_l - \tau_{kl}), \tag{29}$$

where L is the number of clusters, K_l is the number of rays (MPCs) in the l^{th} cluster, $\overline{\beta_{11}^2}$ is the local mean power of the 1^{st} ray ($k = 1$) in the 1^{st} cluster ($l = 1$). T_l is the time of arrival of the l^{th} cluster, τ_{kl} is the delay of the k^{th} component relative to the time T_l, and $\delta(\cdot)$ denotes the Dirac delta function. Γ and γ are the cluster power and ray power decay rates, respectively.

Contrary to the traditional S-V model's assumption, we have found that Γ could not precisely capture the attenuation of the multipath clusters in the THz data center environment. Therefore, we propose a modified clustering model with Γ that is expressed into two sections as a function of delay,

$$\Gamma(\tau) = \begin{cases} \Gamma_1 & , 0 < \tau < \tau_{th}, \\ \Gamma_2 & , \tau_{th} \leq \tau < \tau_{Max}, \end{cases} \tag{30}$$

where τ_{th} is a delay threshold value serving as a breakpoint for Γ and can be selected based on the distribution of multipath clusters. Γ_1 and Γ_2 can be determined through linear regression of cluster peak powers in dB and the associated delays in nanosecond. The ray power decay rate γ in each cluster can be obtained by

$$\gamma(\tau) = a \cdot \tau + b, \tag{31}$$

where $\gamma(\tau)$ and its parameters a and b can be determined through linear regression of intra-cluster powers in dB and the associated delays in nanosecond. The S-V model assumes that the distributions of the cluster and ray arrival times may be described by stochastic Poisson processes, which implies that the distribution of inter-arrival time of clusters ($T_l - T_{l-1}$) can be described by an independent exponential probability density function (PDF) as follow,

$$p(T_l|T_{l-1}) \quad = \quad \Lambda \cdot e^{-\Lambda(T_l - T_{l-1})}, l > 0, \tag{32}$$

where Λ is the mean cluster arrival rate, and that the distribution of inter-arrival time of rays ($\tau_{kl} - \tau_{(k-1)l}$) can be expressed by the following PDF,

$$p(\tau_{kl}|\tau_{(k-1)l}) \quad = \quad \lambda \cdot e^{-\lambda(\tau_{kl} - \tau_{(k-1)l})}, k > 0, \tag{33}$$

where λ is the mean ray arrival rate. A schematic illustration of the proposed S-V model introduced in (29)–(31) is shown in Fig. 52.

Figure 53 presents the normalized measured cluster power with respect to excess delay (τ), where the measured data are collected from an ensemble of all the measured positions from the OLoS, NLoS, and ONLoS scenarios as introduced in Section 5.3. The black circles in Fig. 53 represent the normalized measured cluster peak powers from all the measured positions, where the normalization is with respect to the first arriving signal at each measured position. Solid red and dash-dot blue lines represent the linear regression fits of cluster peak powers with slopes (cluster power decay rates) of Γ_1 = -72.3 dB/ns and Γ_2 = -0.58 dB/ns, respectively, where the two regression lines intersect at an excess delay of τ_{th} = 0.7 ns. Parameters a, b for the ray power decay coefficient in (31) have been estimated as 5.48 dB/ns and -75.93 dB, respectively. The average inter-arrival time of clusters ($1/\Lambda$) and rays ($1/\lambda$) are estimated as 4.4 ns and 0.24 ns, respectively. In an ensemble of measured positions, the number of clusters is found to follow a Poisson distribution with a mean of 3, while the number of rays is found to follow a Rayleigh distribution with a

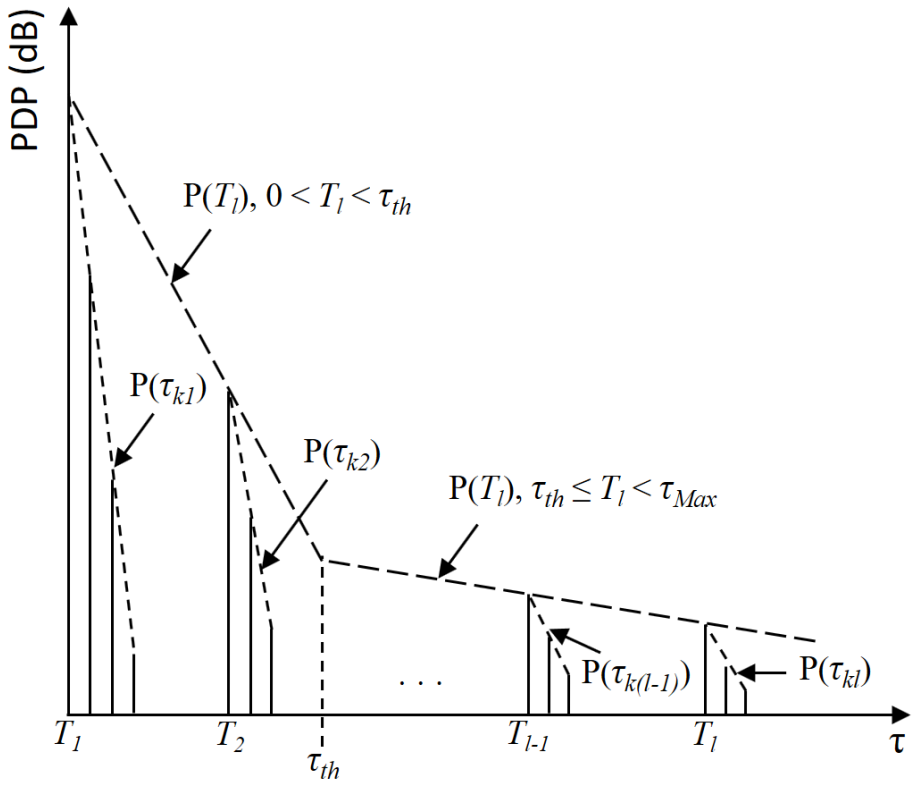

Figure 52: Schematic illustration of the proposed clustering model introduced in (29)–(31).

mean of 4. For the ease of reference, parameters used in the proposed clustering model are summarized in Table 5.

An example of the measured PDP from one of the measured positions in the OLoS scenario with cables serving as obstruction is shown in Fig. 54. It is observed that four clusters (highlighted by thick red lines) were clearly identified using the aforementioned approach. Note that the red lines in Fig. 54 are for annotation, not the actual model. Cluster 2 in Fig. 54 results from the reflections between the Tx lens and the Tx horn and between the Rx lens and the Rx horn. Clusters 3 and 4 consist of the scattered and reflected waves from the Tx/Rx cables. To be more specific, the peak power of cluster 3 is located at excess delay, $\tau = 11.8$ ns, corresponding to an additional delay path of 354 cm that is twice the distance from the Tx horn to the Rx horn plus twice the distance between the Tx cable and the Tx lens and between the Rx cable and the Rx lens (the Tx/Rx cables are positioned at 8–

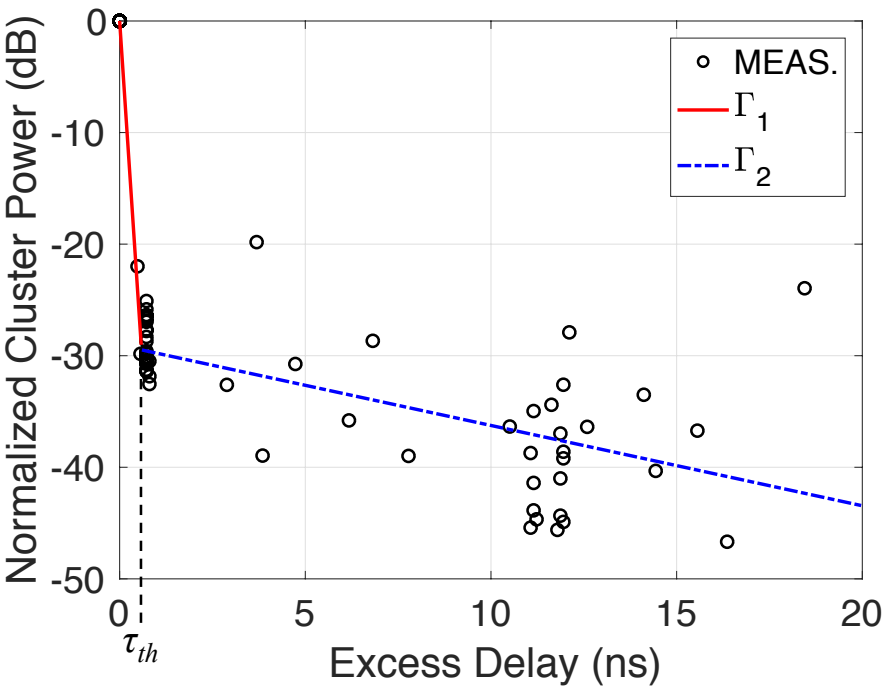

Figure 53: Normalized measured cluster power (black circles) versus excess delay (τ) and the corresponding linear regression fits with slopes of Γ_1 (red solid line) and Γ_2 (blue dot dash line).

10 cm in front of the Tx/Rx lenses). Within cluster 3, the peak power is followed by several MPCs that are 0.56 ns and 1.04 ns away. These MPCs are the results of the single-bounced and double-bounced reflections between the Tx/Rx cables and the Tx/Rx lenses, since the delays of 0.56 ns and 1.04 ns are two times and four times of the distance between the Tx/Rx cables and the Tx/Rx lenses, respectively. The peak power of cluster 4 is located at $\tau = 16.4$ ns, corresponding to an additional delay path of 492 cm that is twice the distance between the Tx cables and Rx cables plus twice the distance between the Tx cable and the Tx lens and between the Rx cable and the Rx lens. Within cluster 4, the peak power is followed by several MPCs that are 0.64 ns and 1.2 ns away. Similar to the observation in cluster 3, these MPCs are the results of the single-bounced and double-bounced reflections between the Tx/Rx cables and the Tx/Rx lenses, since the delays of 0.64 ns and 1.2 ns are two times and four times of the distance between the Tx/Rx cables and the Tx/Rx lenses, respectively. In contrast to cluster 3, the MPCs in cluster 4 decay at a slower rate due to

Table 5: Clustering Model Parameters

Parameter	Value
τ_{th} (ns)	0.7
Γ_1 (dB/ns)	-72.3
Γ_2 (dB/ns)	-0.58
a (dB/ns)	5.48
b (dB)	-75.93
$1/\Lambda$ (ns)	4.4
$1/\lambda$ (ns)	0.24
Cluster No.	3
Ray No.	4

longer propagation path. Note that for all the measured PDPs, the excess delay (τ) of the first arriving MPC is normalized to 0 ns. Noise filtering was performed on PDPs by setting a threshold level of 8 dB above the noise floor as shown in Fig. 54. PDP values below this threshold are considered as noise and equaled to zero.

5.4.2 Pathloss and Shadowing

In this section we analyze the pathloss and the shadowing gain using an ensemble of all measured positions from the OLoS, NLoS, and ONLoS scenarios. We found that the logarithmic equivalent of the pathloss can be modeled as Gaussian distribution, with mean value (μ (dB)) of 75.33 dB and a standard deviation (σ) of 10.71 dB, which corresponds to the *bulk* shadowing gain. The cumulative distribution function (CDF) of the aforementioned pathloss is presented in Fig. 55.

5.4.3 Clustering Statistics

This section analyzes the statistics of the clustering model derived in Section 5.4.1, such as cluster shadowing, distributions of the number of clusters and rays, and correlation coeffi-

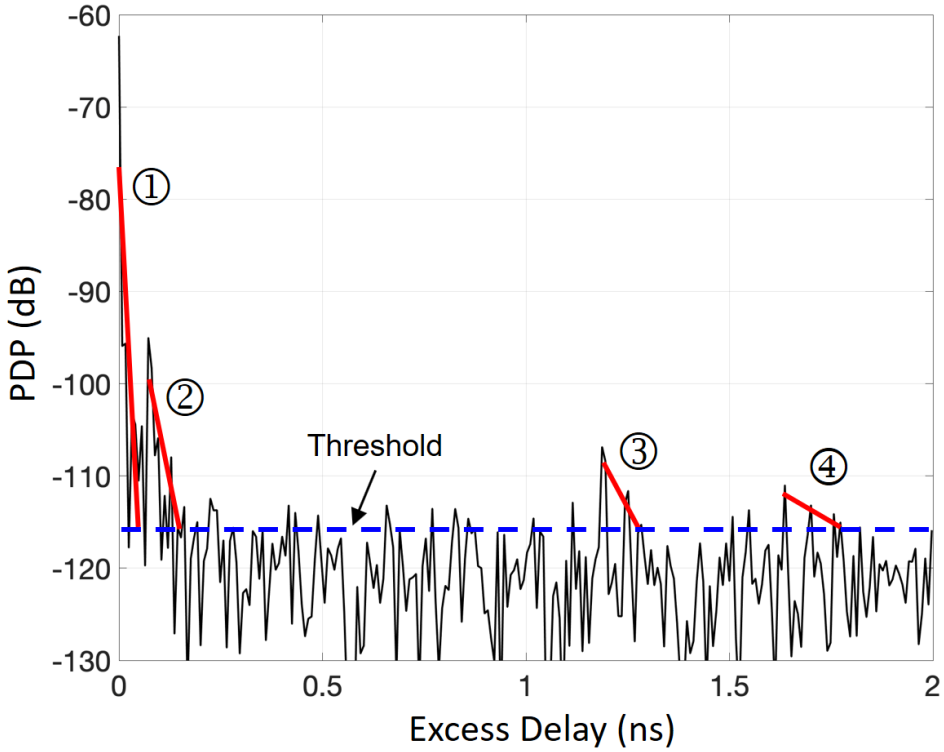

Figure 54: Measured PDP and the identified clusters in the OLoS link with cables serving as obstruction.

cient matrix of relevant channel parameters.

The cluster shadowing gain is defined as the difference between the measured cluster power and the expected value that is estimated from the cluster power decay constant ($\Gamma(\tau)$ in (30)). The cluster shadowing gain in our analysis is modeled to be log-normally distributed, where its value in dB approximates a zero-mean Gaussian distribution with $\sigma =$ 7.95 dB. The PDF of the cluster shadowing gain derived from the clustering model is shown in Fig. 56. The fitness of the distribution with respect to the measured data has been quantified by a maximum deviation value metric [111], $D_{\text{v}} = \text{Max}|F_{\text{measurement}}(\text{x}) - F_{\text{test}}(\text{x})|$, where $F_{\text{measurement}}(\text{x})$ and $F_{\text{test}}(\text{x})$ are the CDFs of the measured cluster shadowing gain and the tested distributions, respectively. Several typical theoretical distributions such as log-normal, Rayleigh, exponential, Nakagami, normal, Rician, and Weibull have been tested, and the results are shown in the second column in Table 6. The log-normal distribution is

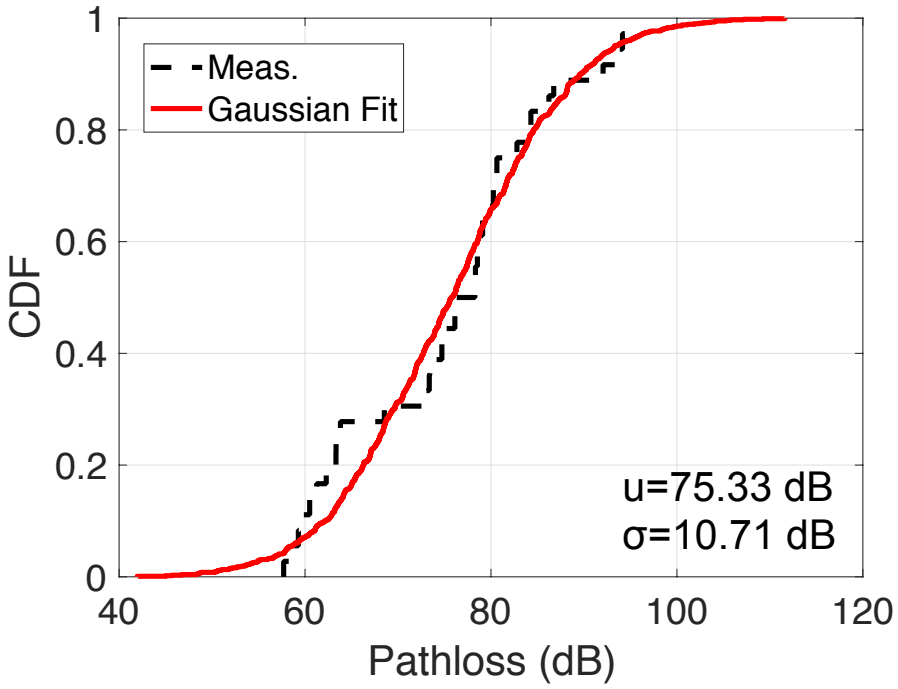

Figure 55: CDF of the mean pathloss measured from all the measured positions in the OLoS, NLoS, and ONLoS links.

found to have the smallest D_{v} of 0.057 among all the tested distributions, which is small according to [112] and thus confirms a good fit.

Our empirical results of PDPs measured from all the measured positions show that the number of clusters $\mathrm{N_{cluster}}$ can be modeled as $\mathrm{N_{cluster}} = \mathrm{N_{min}} + \mathrm{X}$, where $\mathrm{N_{min}} = 1$ is the minimum number of clusters, and X is a Poisson distributed random variable with an average rate (λ) of 1.64. As a result, the mean of $\mathrm{N_{cluster}}$ is 2.64, which explains the reason a cluster number of 3 is used in the proposed model as summarized in the ninth row in Table 5. The CDF of the number of clusters from all the measured positions is presented in Fig. 57 to confirm the Poisson distribution. On the other hand, the number of rays within clusters can be modeled as Rayleigh distributed random variable with a mean value of 4.41, which explains the reason a ray number of 4 is used in the proposed model as summarized in the last row in Table 5. The mean value (μ) of the number of rays within clusters is estimated from the scale factor (σ_R) of the Rayleigh distribution [113], where

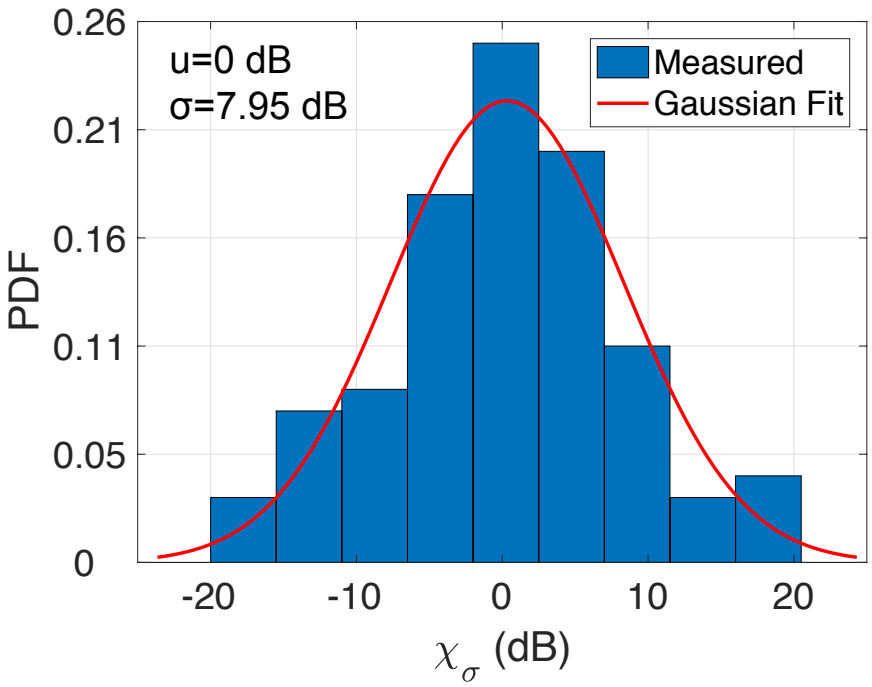

Figure 56: PDF of the cluster shadowing gain (X_σ) derived from the clustering model.

$\mu = \sigma_R\sqrt{\pi/2}$. The CDF of the number of rays within clusters from all the measured positions is presented in Fig. 58 and is modeled to be Rayleigh distributed. Several typical theoretical distributions have been tested, and the results are shown in the third column in Table 6. The Rayleigh distribution is observed to have the smallest D_{v} of 0.177 among all the tested distributions.

A correlation coefficient matrix of parameters such as cluster power, cluster shadowing, τ_m, and τ_{rms}, is shown in Fig. 59. It can be observed that there are high correlations between cluster power and cluster shadowing, and between τ_m and τ_{rms}, respectively.

5.4.4 Model Validation

The proposed clustering model is validated by comparing the distributions of the τ_{rms} derived from our model to that obtained from the measured data. τ_{rms} is chosen because it is a fairly standard criterion for validation of clustering models, and has been used in various publications such as [40, 32, 31]. To derive the τ_{rms} from the proposed model, we first

Table 6: Maximum Deviation (D_{v}) Values Between the Cluster Shadowing Gain/Number of Rays and Distribution Fits

Distribution	$\boldsymbol{D_v}$	
	Cluster Shadowing	**Number of Ray**
Rayleigh	0.720	0.177
Log-normal	0.057	0.184
Exponential	0.347	0.201
Nakagami	0.261	0.220
Normal	0.326	0.231
Rician	0.717	0.190
Weibull	0.062	0.193

synthesize the PDP using the parameters presented in Table 5, then estimate the τ_{rms} from the synthesized PDP using (5). Two examples of the measured (red solid line) and synthesized/modeled (black dash line) PDPs in the OLoS link with cables serving as obstruction with different Tx/Rx (horizontal) positions have been presented in Figs. 60 (a) and (b). It can be observed that the modeled PDPs have a good agreement with the measurements and that the dominant MPCs above the threshold are clearly captured by the model.

Figure 61 presents the CDF of the modeled τ_{rms} and the measured τ_{rms} obtained from all the measured positions. Visually, we have observed that the distribution of the modeled τ_{rms} is in good agreement with the measured data, where the μ and σ are estimated as -95.06 dB and 3.17 dB, respectively. In addition to the visual inspection, a maximum deviation value metric [111], $D_{\text{v}} = \text{Max}|F_{\text{model}}(\text{x}) - F_{\text{measurement}}(\text{x})|$, where $F_{\text{model}}(\text{x})$ and $F_{\text{measurement}}(\text{x})$ are the distributions obtained from the model and measurements, respectively, is used to quantify the fitness of the model with respect to the measured data. The value of D_{v} is estimated as 0.153, which is small according to [112] and thus confirms a good fit. Please note that the statistics of the clustering model are derived from the number of measurement points collected in this measurement campaign. To acquire a more

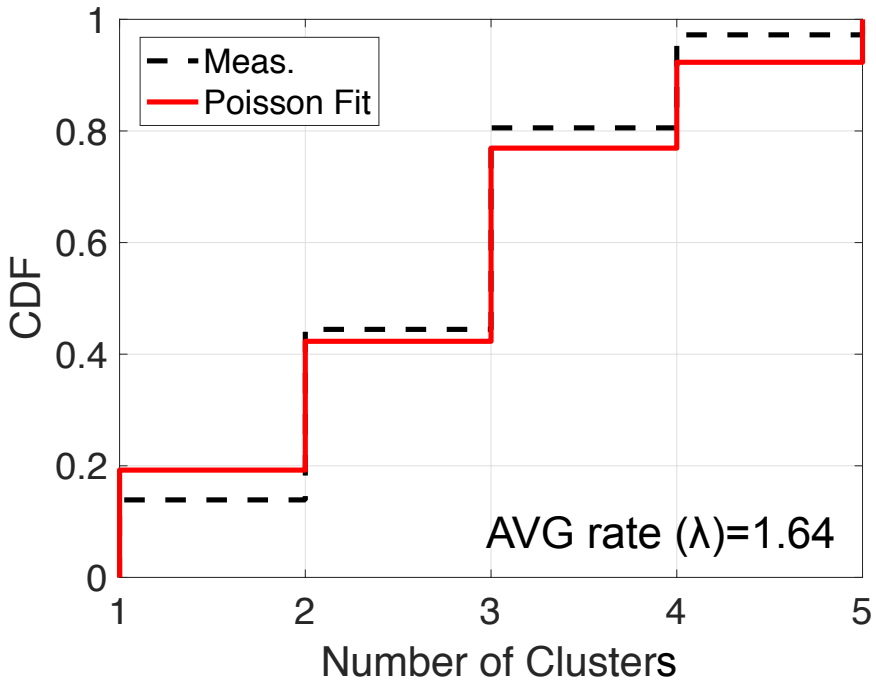

Figure 57: CDF of the number of clusters derived from the clustering model.

generalized statistical characterization of the clustering model, complementary measurements in other data centers with multiple Tx/Rx positions would be required to validate how much the model parameters change from data center to data center. This is, however, a challenge often encountered in channel modeling, especially for a data center environment, where special permission is required to access the facility since data centers hold sensitive or proprietary information. Nonetheless, the measurement designs and results provided in this paper are the starting point for realistic performance evaluations and designs of THz communication systems in a data center environment.

5.5 Summary

This chapter presents a cluster-based propagation model for THz propagation in a data center environment. The proposed model is validated with measured data, where the average numbers of clusters and rays are estimated as 3 and 4, respectively, and the average

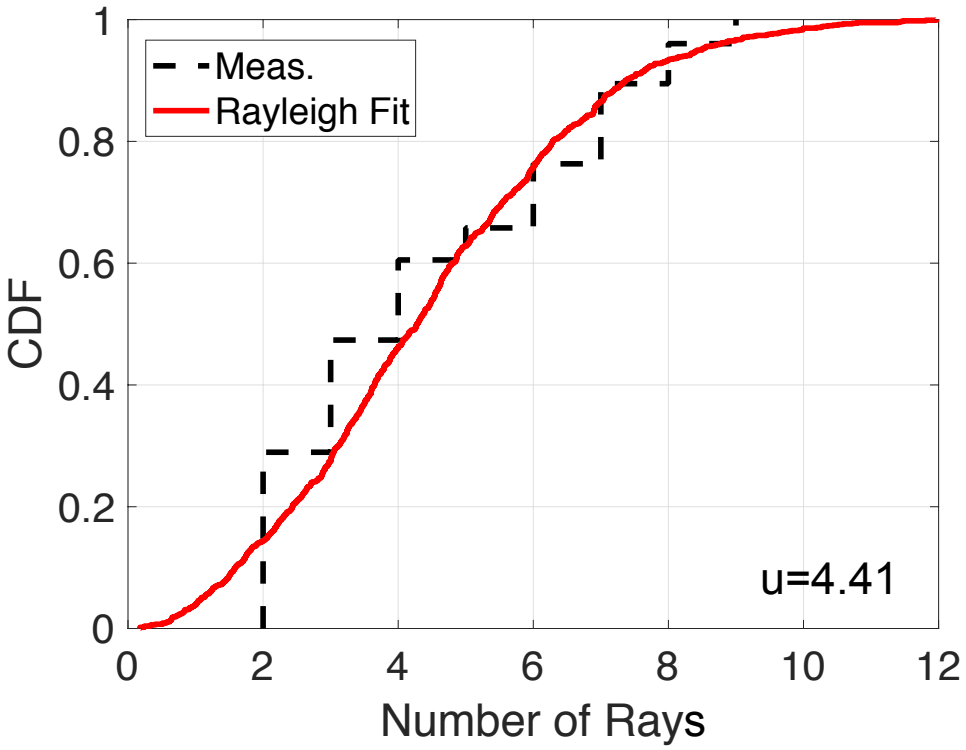

Figure 58: CDF of the number of rays derived from the clustering model.

inter-arrival time of clusters ($1/\Lambda$) and rays ($1/\lambda$) are estimated as 4.4 ns and 0.24 ns, respectively.

	Cluster pwr	Cluster shad	τ_m	τ_{rms}
Cluster pwr	1	0.9989	-0.17	-0.197
Cluster shad	0.9989	1	-0.166	-0.193
τ_m	-0.17	-0.166	1	0.9451
τ_{rms}	-0.197	-0.193	0.9451	1

Figure 59: Correlation coefficient matrix of parameters derived from the clustering model: cluster power, cluster shadowing, τ_m, and τ_{rms}.

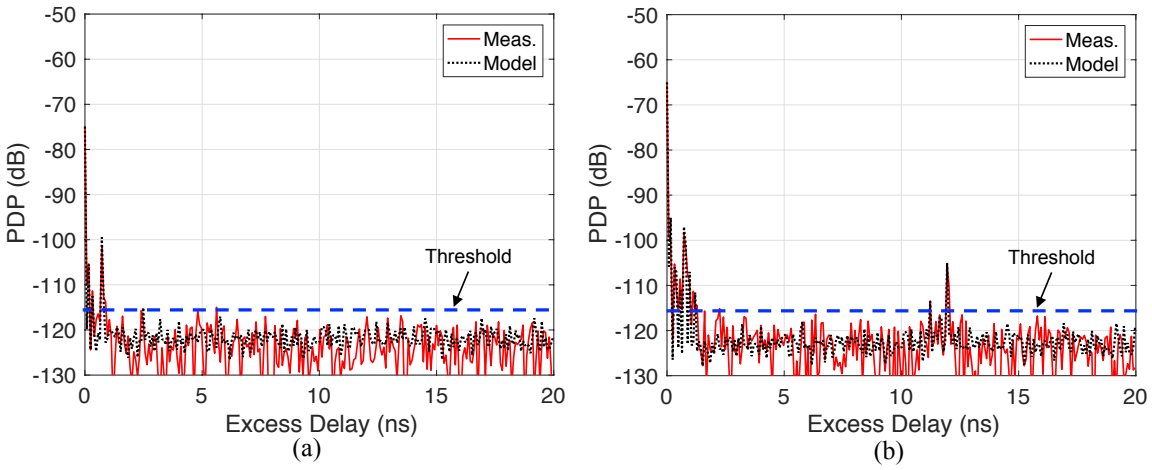

Figure 60: Comparison of the measured (red solid line) and modeled (black dash line) PDPs in the OLoS link with cables serving as obstruction, where (a) and (b) present the results from two different Tx/Rx (horizontal) positions.

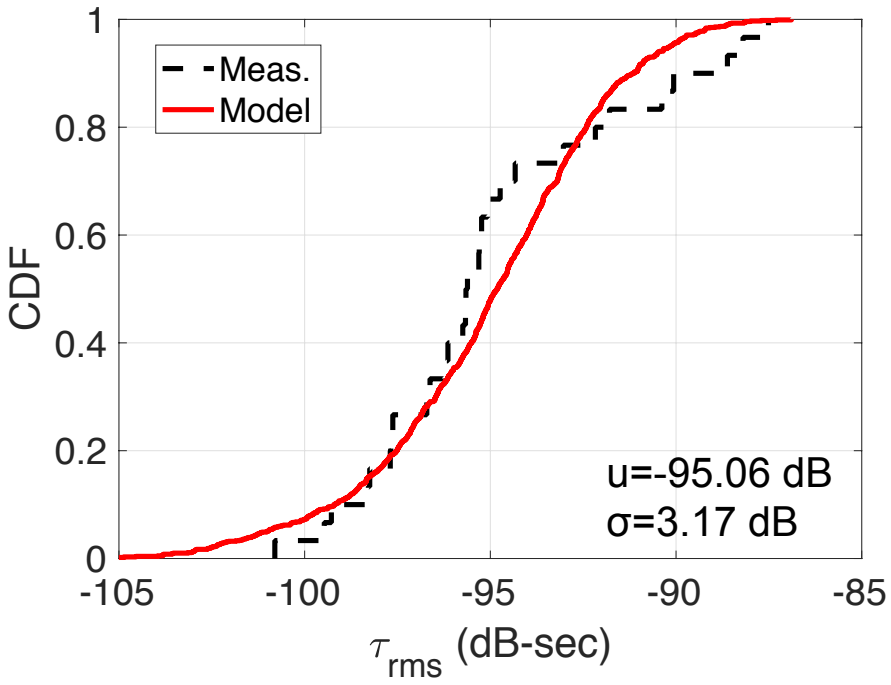

Figure 61: CDF of the measured and modeled τ_{rms} obtained from all the measured positions in the OLoS, NLoS, and ONLoS links.

CHAPTER 6
IMPEDANCE ESTIMATION OF SWITCHING TRANSISTORS IN DIGITAL ELECTRONICS FOR THZ ANTENNA-LESS RFID TAGS

6.1 Overview

Chapter 2.4 summarizes state of the art in RFID tag design. Traditional backscatter communication refers to a radio channel where a reader sends a continuous carrier wave (CW) signal to a tag and retrieves information from a modulated wave scattered back from the tag. During backscatter operation, the input impedance of a tag antenna is intentionally mismatched by two-state RF loads (Z_0 and Z_1) to vary the tag's reflection coefficient and radar cross section (RCS) and to modulate the incoming CW [41, 42]. Mm-wave RFIDs (MMID) [43, 44, 45, 46, 47] and THz RFIDs [48, 49, 50] have been developed due to the wider available bandwidth at higher frequencies that allows high data rates and superior spatial resolution for short-range communication and localization. However, the form factor of all the existing RFID tags has limited room for further miniaturization since they all need to use antennas, which are the largest parts of the tag [46]. To fulfill this need, we develop an antenna-less RFID tag that is based on a new type of backscatter radio generated from switching of transistors in digital electronics, which does not need to use antennas or any RF front-end circuits thereby further reducing the device's form factor. Moreover, the proposed antenna-less RFID tags are compatible with a wide range of interrogating carrier frequencies from sub-6 GHz up to 300 GHz, and can be implemented on existing electronics without additional cost. Since this is a new type of backscatter communication, the backscatter mechanism needs to be addressed.

This chapter introduces a circuit impedance model that explains the modulation mechanism of the proposed backscatter radio and describes the relation between the total input

impedance and the logic resources of the digital circuits. The procedure of estimating the impedance (resistance and reactance) of the antenna-less RFID tag from SPICE model parameters is also presented.

The remainder of the chapter is organized as follows. Section 6.2 explains the modulation mechanism of the proposed backscatter radio and describes an equivalent circuit model for the digital circuits in the antenna-less RFID tag. Section 6.3 describes the procedure of estimating the impedance (resistance and reactance) of the antenna-less RFID tag. Finally, Section 6.4 provides some concluding remarks.

6.2 Equivalent Circuit Model

Traditional backscattering communication in Fig. 2 refers to a radio channel where a reader sends a continuous carrier wave (CW) signal and retrieves information from a modulated wave scattered back from a tag. During backscatter operation, the input impedance of a tag antenna is intentionally mismatched by two-state RF loads (Z_0 and Z_1) to vary the tag's reflection coefficient and to modulate the incoming CW [41]. Compared to the traditional RFID backscattering modulation scheme, our proposed RFID tag in Fig. 62 is modulated by switching activity in digital logic, e.g., programmable logic gates and flip-flops inside a field-programmable gate array (FPGA) chip. The equivalent impedance of the digital logics changes as toggling patterns and number of toggled flip-flops change. This impedance variation amplitude-modulates the signal power reflected off from the chip (transistors). As a result, the proposed RFID tag does not require any pre-designed antennas, two-state RF loads (Z_0 and Z_1), and RF front-end circuits, e.g., matching networks, resonant circuits, etc. By controlling the activity of the chip's logic and flip-flops, we can transmit information through backscatter modulation.

We use FPGA to demonstrate the proposed antenna-less backscatter communication due to its re-configurability. A simplified internal structure of an FPGA chip is shown in Fig. 63 (a), where logic blocks are arranged in a two-dimensional grid and are connected

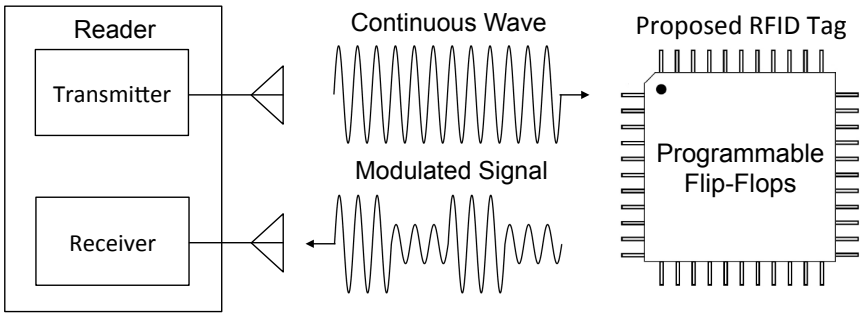

Figure 62: Proposed antenna-less RFID tag.

by a programmable-routing interconnect. This symmetrical grid is connected to I/O blocks which make off-chip connections. The "programmable/re-configurable" term in FPGAs indicates their ability to implement a new function on the chip after its fabrication is complete. Logic blocks can be simplified as programmable flip-flops shown in Fig. 63 (b-1). The output circuit of flip-flops consists of multiple inverters [114]. An equivalent output circuit of a CMOS inverter is shown in Fig. 63 (b-2). During the steady state, when input voltage of the inverter is low, NMOS transistors are off and PMOS transistors are on. A direct path exists between V_{out} and V_{DD}, resulting in a high output state. On the other hand, high input results in a low output state. As shown in Fig. 63 (b-3), there exists a finite resistance between the output and V_{DD} (R_1 or R_p) and between the output and the ground (R_0 or R_n), respectively. During the transient state, that is, when the input voltage of the inverter is switching from low to high and from high to low, parasitic capacitance would influence the transient behavior of the cascade inverter pair [115]. An equivalent output circuit of the cascaded inverter pair during transient state is shown in Fig. 64, where C_{gd} is the gate-drain capacitance, C_{db} is the diffusion capacitance, C_g is the gate capacitance of fanout, C_w is the wiring (interconnect) capacitance, and N is the fanout number of the cascaded inverter. For simplification, all the capacitances are lumped together into one single capacitor C_L located between V_{out} and ground.

The switching between inverter's high output state (Z_1) and low output state (Z_0) creates impedance variation, which is analogous to the variation in antenna terminating

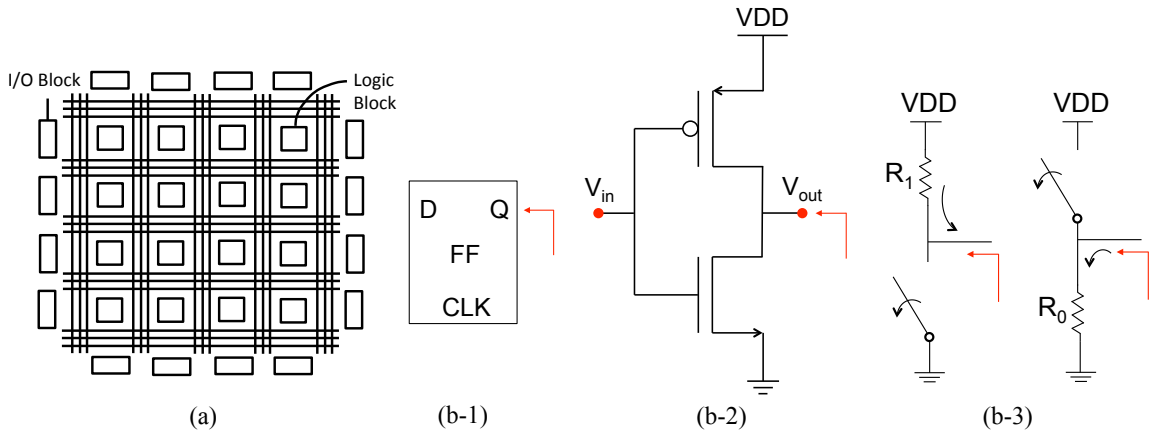

Figure 63: (a) Simplified internal structure of FPGA; RFID tag circuit model: (b-1) programmable flip-flop, (b-2) equivalent output circuit of a CMOS inverter, (b-3) high-state resistance, R_1 (PMOS on resistance) and low-state resistance, R_0 (NMOS on resistance).

impedance in typical RFID tags. The impedance variation creates a difference in the circuit's RCS and thus modulates the electronic backscatter signals. In order to modulate the electronic backscatter signals, we have programmed flip-flops to switch in a pattern shown in Fig. 65 (a). Flip-flops continuously switch between high state and low state at a clock frequency (f_{clock}) of 50 MHz for half of clock cycle and stay quiet for the other half of the clock cycle. The switching cycle (modulating frequency, f_m) directly relates to the modulated signal bandwidth, i.e., the first harmonic of the modulated backscatter signal will be located at $f_{carrier} \pm f_m$. By changing f_m, we can easily upshift or downshift the modulated signals, making design very flexible. Note that f_m should be selected to avoid undesired harmonics in higher frequencies, i.e., the highest sideband (f_m) needs to be less than three times of the lowest sideband (f_m), and to comply radio regulations and avoid interference from other radio systems. Please note that in practice, the switching transistors do not produce ideal square pulses but rather pulses that have rising and falling edges, which sometimes leads to appearance of signals at even harmonics of the modulated backscatter signal. To avoid undesired interference, the highest sideband (f_m) should be less than two times the lowest sideband (f_m).

In addition to the switching pattern, the number of simultaneously-switched elements

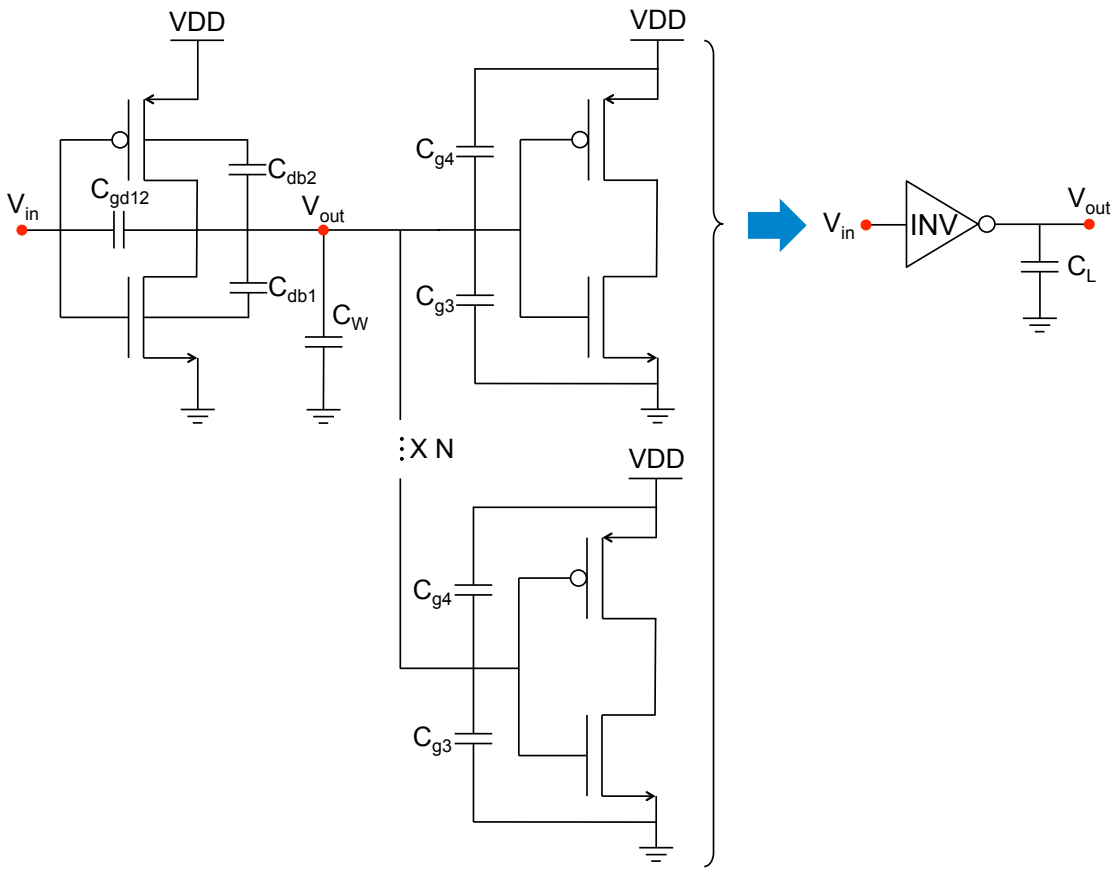

Figure 64: Parasitic capacitance observed at the output of the cascaded inverter during transient state.

is another factor that affects electronic backscattering modulation. The more flip-flops are switching in unison, the stronger the backscatter signal is. To control the number of elements that switch simultaneously, we use an N-bit shift register, where N can be used to control the number of simultaneously-toggled flip-flops. Fig. 65 (b) shows a simplified schematic for a 3-bit shift register, created by connecting N=3 flip-flops (FFs). Fig. 66 shows how logic is mapped onto an Altera Cyclone V FPGA chip for different values of N, Dark blue blocks represent utilized resources (flip-flops and logic) while light blue blocks denote unused resources. This Cyclone V FPGA chip is completely utilized (100% design in Fig. 66) when N=36600, and designs with 50% and 30% utilization use N=18300 and N=10980, respectivelly. Note that other FPGA chips may contain diferent numbers of programmable elements (total available N), so the same utilization percentage may require

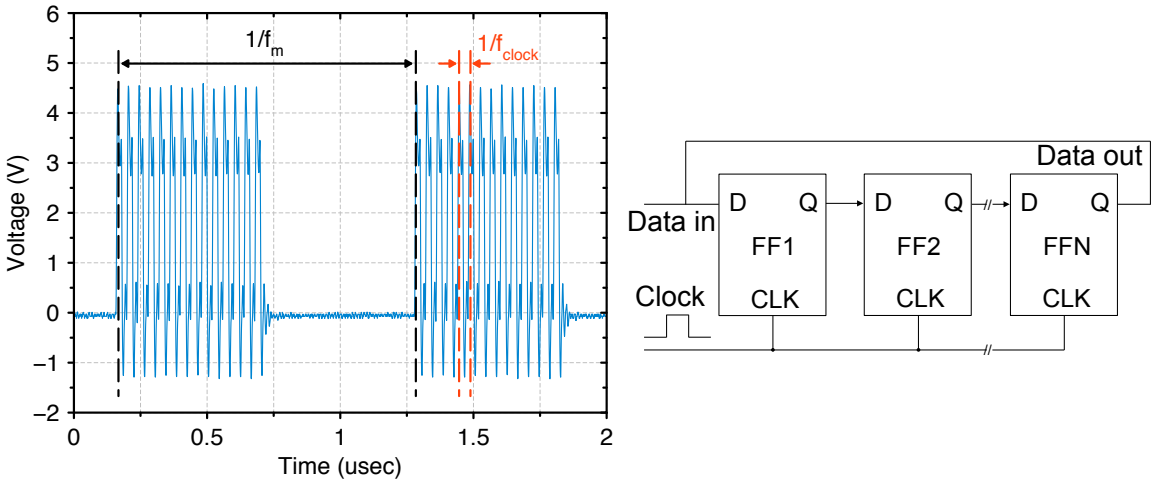

Figure 65: (a) Flip-flops switching signal pattern at f_m=900 kHz; (b) Simplified building block of an N-bit shift register.

different values of N to be selected when using other FPGA chips.

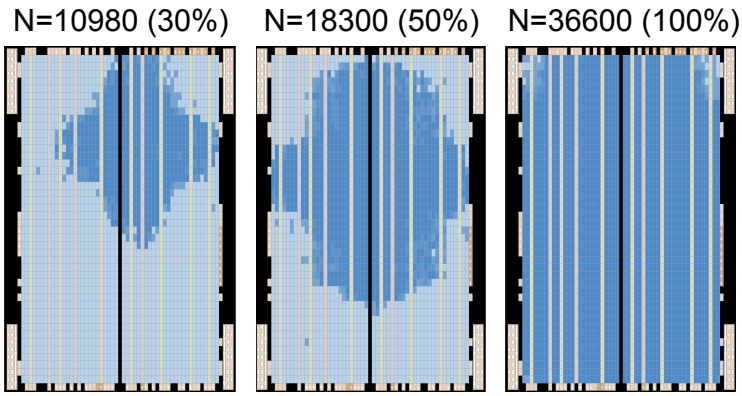

Figure 66: Logic utilization mapping of an ALTERA Cyclone V FPGA chip.

6.3 Estimation of Resistance and Reactance

Output impedance of a power supply network in integrated circuits is the parallel combination of output impedances of individual power-supply connections of all flip-flops[84]. The more flip-flops are connected, the more individual power supplies are connected in parallel, which reduces impedance. That is, the total input impedance of the proposed RFID tag is

inversely related to the logic utilization N. Given this relationship between logic utilization and input impedance, we introduce a modulation loss factor, M, which relates the total tag's modulation loss to transistors' impedance variation. M can be expressed as [116]

$$M(x\%) = \frac{1}{4}\left|\frac{Z_1(x\%) - 377^*}{Z_1(x\%) + 377} - \frac{Z_0(x\%) - 377^*}{Z_0(x\%) + 377}\right|^2 \tag{34}$$

where $Z_1(x\%)$ and $Z_0(x\%)$ are the estimated high state (1s) impedance and low state (0s) impedance of the FPGA chip, and parameter x represents the percentage of total logic resources being configured. Impedance, $Z_{1/0}$, consists of resistance, $R_{1/0}$, and reactance, $X_{1/0}$, where $R_{1/0}$ is the real part of the high/low state impedance and $X_{1/0}$ is the imaginary part of the high/low state impedance, i.e., $Z_{1/0} = R_{1/0} + jX_{1/0}$. Resistance and reactance together determine the magnitude and phase of the impedance. $Z_1(x\%)$ and $Z_0(x\%)$ are defined as,

$$Z_1(x\%) = \frac{Z_1(10\%)}{\frac{x\%}{10\%}} \tag{35}$$

$$Z_0(x\%) = \frac{Z_0(10\%)}{\frac{x\%}{10\%}}. \tag{36}$$

$Z_1(10\%)$ and $Z_0(10\%)$ are the estimated high state (1s) and low state (0s) impedance of an FPGA chip where 10 % of total resources are utilized. The input impedance of the tag is equal to free space impedance, 377 Ω, since there is no antenna but only air at the interface between the carrier signal and FPGA chip.

In order to estimate $Z_0(10\%)$ and $Z_1(10\%)$, we first calculate the values of $R_{1/0}$ and $X_{1/0}$ using transistor's SPICE model parameters (22nm PTM LP model in [117], which shares the same technology node as the Altera Cyclone V FPGA) to determine a range for $R_{1/0}$, $X_{1/0}$, and the corresponding $Z_{1/0}$. We then perform curve fitting between the measured backscattered power and the modeled backscattered power to estimate the optimal

value of $Z_{1/0}$. According to [118], R_n (R_0) and R_p (R_1) presented in Fig. 63 (b-3) can be estimated by $R_{n/p} = (R_{lin,n/p} + R_{sat,n/p})/2$, where $R_{lin,n/p}$ and $R_{sat,n/p}$ are the on resistance of the NMOS/PMOS in the linear and saturation regions, respectively, and can be calculated as

$$R_{lin,n/p} = \frac{V_{lin}}{I_{lin}} = \frac{(V_{DD} - V_{SS} - V_{th,n/p})/2}{\frac{3}{8}k'_{n/p}(\frac{W}{L})_{n/p}(V_{DD} - V_{SS} - V_{th,n/p})^2}, \tag{37}$$

and

$$R_{sat,n/p} = \frac{V_{sat}}{I_{sat}} = \frac{V_{DD} - V_{SS}}{\frac{1}{2}k'_{n/p}(\frac{W}{L})_{n/p}(V_{DD} - V_{SS} - V_{th,n/p})^2}. \tag{38}$$

$k'_{n/p}$ represents $u_{n/p}C_{ox}$, where $u_{n/p}$ is the mobility of NMOS/PMOS and C_{ox} is the gate capacitance. W and L are the width and length of the transistor, respectively. V_{SS} and V_{DD} are the source and drain voltage, respectively. $V_{th,n/p}$ is the threshold voltage of NMOS/PMOS. Detailed values of the above parameters can be found in [117, 115, 119]. The expressions and estimated values of parasitic capacitances C_{gd}, C_{db}, C_g, C_w, and C_L are presented in Table 7, and the definitions of the corresponding parameters are provided in Table 8. Results in [117, 115, 119] provide detailed values of the parameters for the parasitic capacitance.

Table 7: Estimated Values and Expressions of the Parasitic Capacitance

Capacitor	**Expression**	**Value (fF)**	
		High-to-Low	**Low-to-High**
C_{gd1}	$2C_{on}W_n$	0.0143	0.0143
C_{gd2}	$2C_{op}W_p$	0.0143	0.0143
C_{db1}	$K_{eqbpn}AD_nCJ_n + K_{eqswn}PD_nCJSW_n$	0.0524	0.0662
C_{db2}	$K_{eqbpp}AD_pCJ_p + K_{eqswp}PD_pCJSW_p$	0.0692	0.0584
C_{g3}	$C_{ox}W_nL_n + (2C_{on})W_n$	0.074	0.074
C_{g4}	$C_{ox}W_pL_p + (2C_{op})W_p$	0.074	0.074
C_w	From extraction	0.085	0.085
C_L	$C_{gd1}+C_{gd2}+C_{db1}+C_{db2}+(C_{g3}+C_{g4})*N+C_w$	0.383	0.386

Using the resistance and reactance values estimated from the SPICE model as a boundary

Table 8: Definitions of the Parameters for the Parasitic Capacitance

Parameter	Definition
$C_{ox\_n/p}$ (fF/um^2)	Gate CAP (CAP per unit area by gate oxide)
$C_{on/p}$ (fF/um)	Overlap CAP
$CJ_{n/p}$ (fF/um^2)	Bottom junction CAP
$CJSW_{n/p}$ (fF/um)	Sidewall junction CAP
$AD_{n/p}$ (um^2)	Drain area
$PD_{n/p}$ (um)	Drain perimeter
$K_{eqbpn/p}$	Bottom plate capacitor linearization factor
$K_{eqswn/p}$	Sidewall capacitor linearization factor

condition, we then perform curve fitting between the measured backscattered power and the modeled backscattered power to estimate the optimal value of (Z_1, Z_0). Fig. 67 presents the estimated resistance ($R_{1/0}$), reactance ($|X_{1/0}|$), and the corresponding modulation loss factor (M) calculated by (34). Detailed descriptions of the backscatter measurement setup

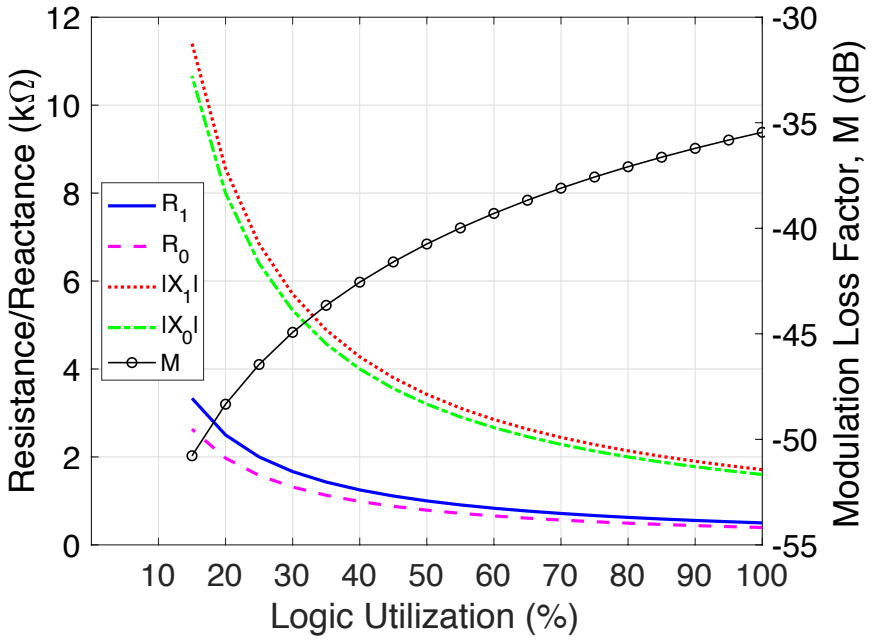

Figure 67: Estimated values of R_1, R_0, $|X_1|$, $|X_0|$, and modulation loss factor (M) with respect to logic utilization (%).

and the measured backscattered power can be found in Chapter 7. The M describes the modulation loss factor as a function of the logic utilization of the digital circuits and is a crucial component in the propagation model introduced in this thesis, which can be used to

estimate the link budget. Please note that the impedance value and the propagation model are estimated and developed at 26.5 GHz ($|X_{1/0}|$ is a function of frequency) since the compact antenna form factor at 26.5 GHz has a shorter Fraunhofer distance that guarantees far-field propagation for the measurement distances we studied. Although Fraunhofer distance at 300 GHz is even shorter due to smaller antenna size, the higher attenuation at 300 GHz limits the distance range for the development of the proposed propagation model.

6.4 Summary

This chapter presents a circuit impedance model that explains the modulation mechanism of the backscatter radio generated by the switching transistors inside digital circuits and describes the relation between the total input impedance and the logic resources of the digital circuits. The procedure of estimating the impedance (resistance and reactance) of the antenna-less RFID tag from SPICE model parameters is also presented.

CHAPTER 7

PROPAGATION MODEL FOR ANTENNA-LESS BACKSCATTER RADIO

7.1 Overview

A complete propagation model for traditional backscatter radio systems is required to assess link budget, which is important for evaluating the feasibility and reliability of a wireless link. However, the existing backscatter propagation model does not provide the estimation of the modulation loss resulting from the switching activity of the digital electronics, and thus cannot be directly applied to the proposed antenna-less backscatter radio link.

To address this need, this chapter introduces a new propagation model for the antenna-less RFID tag. The proposed propagation model consists of a modulation loss factor (due to the switching of transistors) that is derived from the proposed circuit impedance model introduced in Chapter 6, and can be used to estimate link budget. Detailed derivation of the proposed backscattered power model and validation with measurements are provided. The shadowing gain for the carrier power and the backscattered power have been characterized as 3.93 dB and 0.96 dB, respectively, showing that the backscattered channel can provide a more reliable link that is resistant to the constructive and destructive interference from the multipaths as compared to the carrier link.

The remainder of the chapter is organized as follows. Section 7.2 presents measured backscattered signal to demonstrate that the impedance difference between transistor gates in the high-state and in the low-state can change the radar cross section and modulate the backscattered signal through amplitude modulation. Section 7.3 introduces the propagation models for the proposed RFID tags, including the carrier power model and the proposed backscattered power model. Modeling results are tested against measurements. Finally, Section 7.4 provides some concluding remarks.

7.2 Demonstration of Backscattered Modulation From Switching of Transistors in Digital Electronics

This section demonstrates that the impedance difference between transistor gates in the high-state and in the low-state can change the radar cross section and amplitude-modulate the backscattered signal. Please note that for the demonstration of the proposed backscatter modulation and the development of propagation model presented in this chapter, we use an interrogating frequency at 26.5 GHz since it belongs to the FR2 band of the 5G spectrum and the compact antenna form factor in the mm-wave frequencies results in shorter Fraunhofer distance that guarantees far-field propagation for the measurement distances we studied. Although the Fraunhofer distance at 300 GHz is even shorter due to smaller antenna size, the higher attenuation at 300 GHz limits the distance range for the development of the proposed propagation model. For the demonstrations of the proposed antenna-less RFID tags with multi-bit static and dynamic IDs interrogated at other frequencies such as 5.8 GHz, 17 GHz, and 300 GHz, readers can refer to Chapter 8.

7.2.1 Measurement Setup

An Agilent MXG N5183A Signal Generator with input power of 15 dBm (31.6 mW) and $f_{carrier}$ =26.5 GHz is used as a signal source and an Agilent MXA N9020A Vector Signal Analyzer is used to record the signals. An Altera DE0-Cyclone V FPGA board is used as the RFID tag as shown in Fig. 68 (a). For interrogation, we use horn antennas (A-INFO LB-28-10) shown in Fig. 68 (b) that operates from 26.5 GHz to 40 GHz with 55° HPBW and an average isotropic gain of 10 dBi.

7.2.2 Measurement Results

The switching frequencies (f_m, shown in Fig. 65 (a)) of the flip-flops in the FPGA board are set as 900 kHz with logic utilization of 100 %. Fig. 69 shows the measurement results with

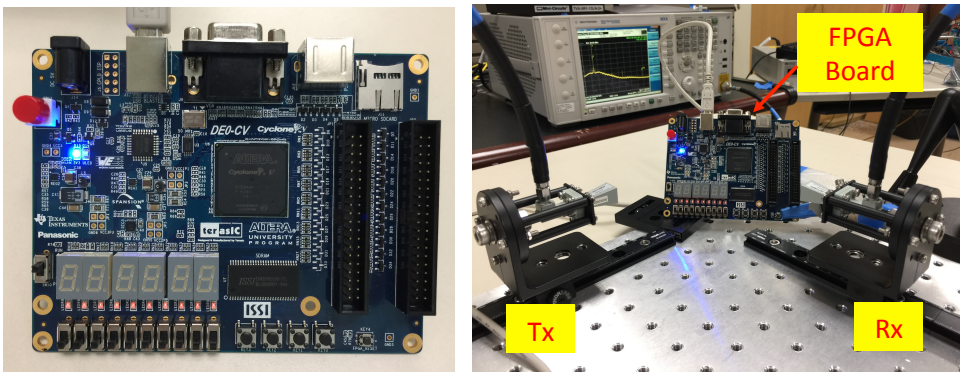

(a) (b)

Figure 68: (a) Altera Cyclone V FPGA board; (b) measurement setup for the 26.5 GHz measurement.

f_m=900 kHz (red). The standby curve (blue) is the measured power spectrum when FPGA board is turned on but not switching. Distinct modulated sidebands are observed at 26.5 GHz $\pm$ 900 kHz. Signal strength of the modulated sideband is around -122 dBm with an SNR of around 26 dB. In the standby mode, other modulated sidebands around 26.5 GHz are also observed. Since the measurement is conducted in an indoor office environment, these modulated sidebands are results from surrounding interference, e.g., measurement instruments, LCD monitors, mobile phones, WiFi routers, etc. **Note that conductive traces on an FPGA board that connect the FPGA chip to GPIO pins may act as antennas and radiate the backscatter signal. We disconnect these traces to verify that the signal is coming from the FPGA chip itself and not from the board. When turned on, GPIO pins can still operate correctly but will produce stronger RFID signal**. Our experiment results in Fig. 69 verify that switching electronics can establish backscatter channels without any antennas or RF front-end circuits.

7.3 Propagation Models

This section introduces the propagation models for the proposed RFID tags, including the carrier power model and the proposed backscattered power model. Modeling results are tested against measurements at 26.5 GHz.

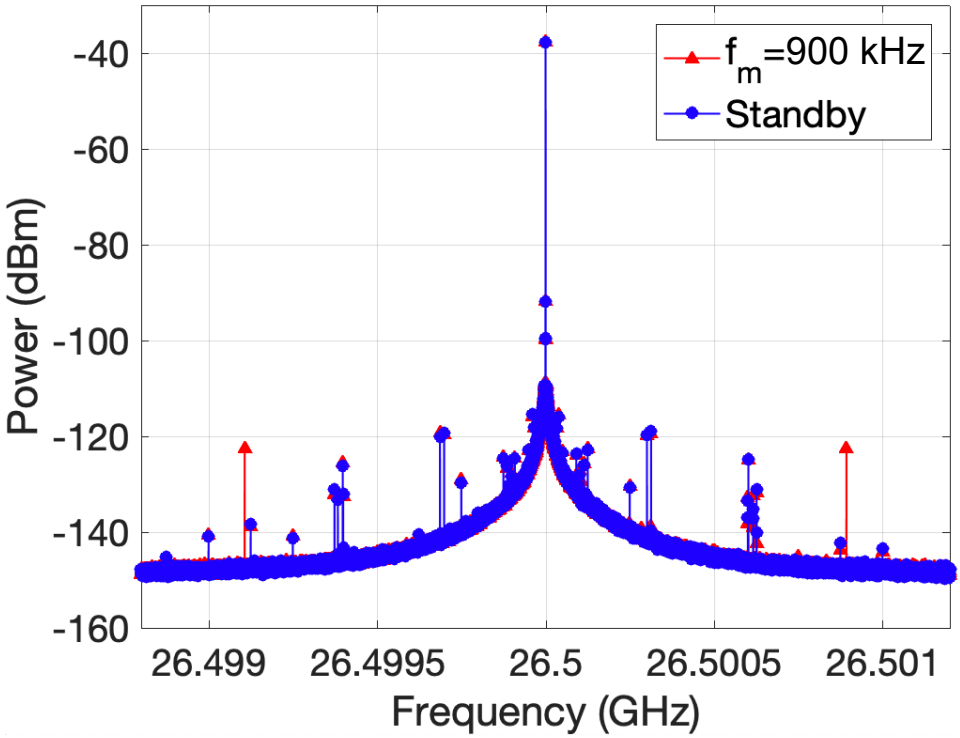

Figure 69: Measured backscattered power with $f_{carrier}$ =26.5 GHz and f_m =900 kHz (red). The standby curve (blue) is the measured backscattered signal when FPGA board is turned on but not switching.

7.3.1 Carrier Power Model

A carrier power model that is similar to the FI pathloss model in (2) is used except that the value being modeled is the received power in dBm rather than the pathloss in dB, which is expressed as

$$P_{\text{rx\_carrier}}(d)[\text{dBm}] = \alpha + 10 \cdot \beta \cdot \log_{10}\left(\frac{d}{d_0}\right) + X_{\sigma}^{P_{\text{rx\_carrier}}}, d \geq d_0. \tag{39}$$

The reference distance, d_0, is 10 cm. The carrier power model parameters (α, β, and σ) are estimated by curve fitting the measured carrier power to (39). The absolute value of parameter β in (39) is equivalent to the PLE in the FI pathloss model in (2).

For the measurement of the carrier power, horn antennas (A-INFO LB-28-10) in Fig. 68 (b) that operates from 26.5 GHz to 40 GHz with 55° half-power beamwidth (HPBW) and

10 dBi gain are used as the Tx and Rx. The interrogating signal has a carrier frequency of 26.5 GHz with a transmitting power (P_t) of 0 dBm. Note that when characterizing a propagation channel, it is important to ensure the measurements are conducted in the far-field range. The largest physical dimension of the horn aperture is 1.9 cm, which defines the far-field boundary to be 6.2 cm at 26.5 GHz according to the Fraunhofer distance. As a result, we vary the Tx-Rx distance from 10 cm to 60 cm with a step size of 1 cm such that the far-field condition is satisfied.

Figure 70 presents the measured and modeled carrier power at 26.5 GHz with Tx-Rx distance (d) varying from 10 cm to 60 cm in a NLoS link with an FPGA PCB board serving as a reflector. The absolute value of parameter β is estimated as 1.66, representing a waveguide type of channel. Moreover, it can be observed that the received carrier power

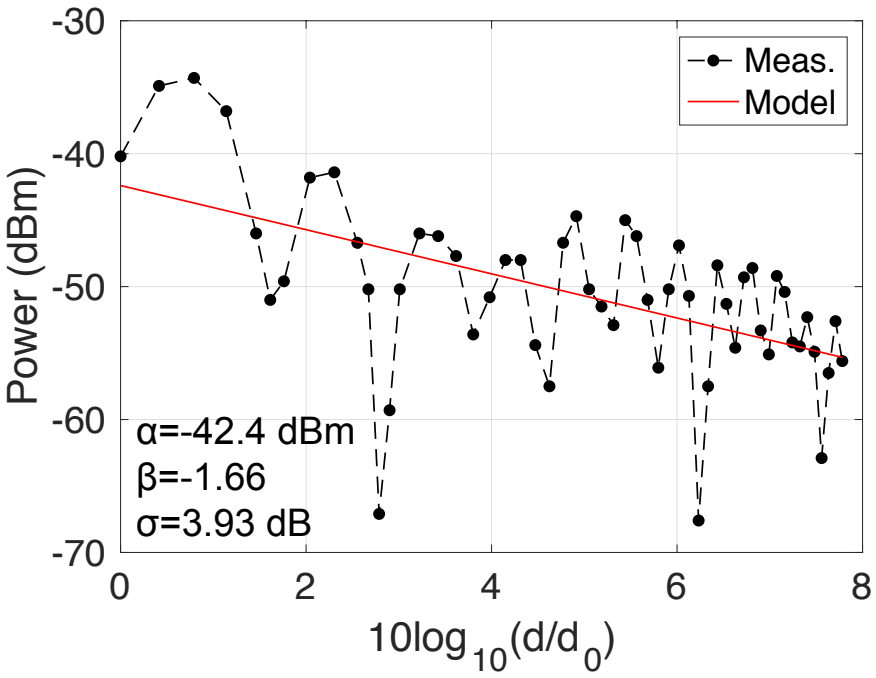

Figure 70: Measured carrier power and modeled carrier power at 26.5 GHz with Tx-Rx distance varying from 10 cm to 60 cm in a NLoS link with an FPGA PCB board serving as a reflector.

experienced significant fluctuation (periodic peaks and dips) over distance with a peak-to-peak separation distance of around 2.5 cm. The lowest received power is observed as -67.1

dBm at a Tx-Rx distance of 19 cm, which is more than 20 dB below the modeled average value (red curve). We conclude that the fluctuation in the received power is caused by the constructive and destructive interference from two reflected paths: 1) ground reflections and 2) reflections between components on the PCB, e.g., surface mount capacitors, resistors, switches, LEDs, I/O ports, buttons. Given that the center of the 26.5 GHz horn antenna aperture is positioned at 6.5 cm above the ground plane with a beam width of 55°, a minimum path length around 30 cm is needed for the ground reflection to arrive at the Rx. Therefore, for Tx-Rx distance of 10 cm–30 cm, the constructive and destructive interference is mainly contributed from multiple reflections between PCB board components, while at Tx-Rx distance beyond 30 cm, the sources of constructive and destructive interference are combinations of ground reflections and the multiple reflections between PCB board components. To quantify the fluctuation of the received carrier power, we have investigate the shadowing gain (X_σ) of the carrier power over distance and found that the X_σ follows a log-normal distribution with its logarithmic equivalent having a zero-mean (in dB) and standard deviations (σ) of 3.93 dB. CDF of the X_σ is presented in Fig. 71 to confirm the log-normality of the shadowing gain.

Our empirical results showed that for the mm-wave chip-to-chip/board-to-board communication scenarios that rely on the NLoS type of link with PCB boards serving as reflectors [120, 121, 122], with Tx-Rx distance varying within a few wavelengths, the wireless system may experience communication dead zones where the received power drops by more than 20 dB from the average power level due to destructive interference from the reflections from the components on the PCB board.

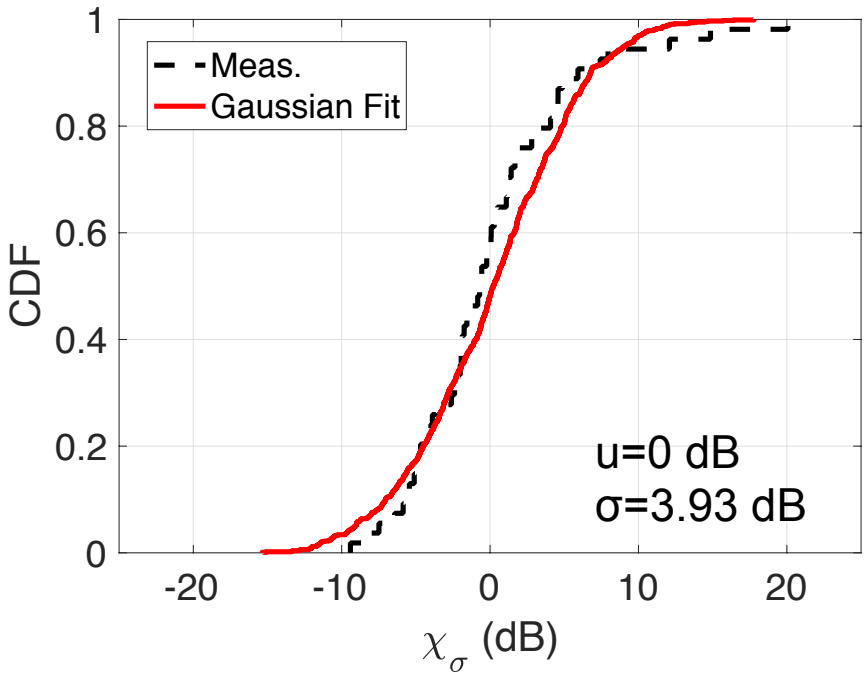

Figure 71: CDF of received carrier power's shadowing gain (X_σ) measured at 26.5 GHz at d = 10 cm–60 cm in a NLoS link with an FPGA PCB board serving as a reflector.

7.3.2 Backscattered Power Model

The proposed backscattered power model addresses the modulated power results from the switching activity of the transistors in the tag, which is defined as,

$$P_{\text{rx\_backscattered}} = S_{\text{tag\_rad}} A_{\text{rx}}, \tag{40}$$

where A_{rx} in (40) is the antenna effective aperture at the receiver and is expressed as

$$A_{\text{rx}} = \frac{\lambda^2}{4\pi} G_{\text{rx}}, \tag{41}$$

and $S_{\text{tag\_rad}}$ in (40) is the non-directional power-flux density from the tag to the Rx that is expressed as,

$$S_{\text{tag\_rad}} = \frac{P_{\text{tag\_rad}}}{4\pi d^2}. \tag{42}$$

$P_{\text{tag\_rad}}$ in (42) is the reradiated power from the tag and is given by

$$P_{\text{tag\_rad}} = S_{\text{tx}}\sigma_{\text{tag}}, \tag{43}$$

where S_{tx} in (43) is the non-directional power-flux density from the Tx to the tag and is expressed as

$$S_{\text{tx}} = \frac{P_{\text{tx}}G_{\text{tx}}}{4\pi d^2}, \tag{44}$$

and σ_{tag} in (43) is the RCS of the tag, which is defined as

$$\sigma_{\text{tag}} = A_{\text{tag}}L_{\text{refl}}M, \tag{45}$$

where L_{refl} in (45) is the reflection loss of the tag, which is estimated as -10 dB by comparing the carrier power reflected from an ideal metal reflector, e.g., copper plate, versus from an FPGA board at a Tx-Rx distance of 10 cm in the NLoS setup in Fig. 68 (b). M in (45) is the modulation loss factor and its value is presented in Fig. 67. A_{tag} in (45) is the antenna effective aperture of the tag, which is defined as

$$A_{\text{tag}} = \frac{\lambda^2}{4\pi}L_{\text{refl}}. \tag{46}$$

The final form of the backscattered power model is given by

$$P_{\text{rx\_backscattered}} = \frac{P_{\text{tx}}G_{\text{tx}}G_{\text{rx}}L_{\text{refl}}^2M\lambda^4}{(4\pi d)^4}. \tag{47}$$

Please note that the d in (47) is the distance from Tx/Rx to the tag. For the ease of reference, detailed descriptions of backscattered power model parameters and formulae are summarized in Table 9.

Table 9: Backscattered Power Model Parameters

Parameter	Description	Formula/Value
$\Gamma_{1,0}$	Reflection coefficient at states 1 and 0.	$\frac{Z_{\mathrm{TAG}}^{1,0} - Z_{\mathrm{ANT}}^{*}}{Z_{\mathrm{TAG}}^{1,0} + Z_{\mathrm{ANT}}^{*}}$
$\Delta\Gamma$	Differential reflection coefficient.	$\frac{1}{2}\lvert\Gamma_1 - \Gamma_0\rvert$
M	Modulation loss factor.	$\Delta\Gamma^2 = \frac{1}{4}\lvert\Gamma_1 - \Gamma_0\rvert^2$
$\mathrm{A_{tag}}$	Antenna effective aperture at the tag.	$\frac{\lambda^2}{4\pi}\mathrm{L_{refl}}$
$\mathrm{A_{rx}}$	Antenna effective aperture at the Rx.	$\frac{\lambda^2}{4\pi}\mathrm{G_{rx}}$
σ_{tag}	Tag radar cross section (RCS).	$\mathrm{A_{tag}L_{refl}M} = \frac{\lambda^2}{4\pi}\mathrm{L_{refl}^2M}$
$\mathrm{S_{tx}}$	Non-directional power-flux density from the Tx to the tag.	$\frac{\mathrm{P_{tx}G_{tx}}}{4\pi d^2}$
$\mathrm{P_{tag\_rec}}$	Received power at the tag.	$\mathrm{S_{tx}A_{tag}} = \frac{\mathrm{P_{tx}G_{tx}L_{refl}}\lambda^2}{(4\pi)^2 d^2}$
$\mathrm{P_{tag\_rad}}$	Reradiated power from the tag.	$\mathrm{S_{tx}}\sigma_{\mathrm{tag}} = \frac{\mathrm{P_{tx}G_{tx}L_{refl}M}\lambda^2}{(4\pi)^2 d^2}$
$\mathrm{S_{tag\_rad}}$	Non-directional power-flux density from the tag to the Rx.	$\frac{\mathrm{P_{tag\_rad}}}{4\pi d^2} = \frac{\mathrm{P_{tx}G_{tx}L_{refl}^2M}\lambda^2}{(4\pi)^3 d^4}$
$\mathrm{P_{rx\_backscattered}}$	Received backscattered power at the Rx.	$\mathrm{S_{tag\_rad}A_{rx}} = \frac{\mathrm{P_{tx}G_{tx}G_{rx}L_{refl}^2M}\lambda^4}{(4\pi d)^4}$

Next, we test the proposed backscattered power model against measurements. The same measurement setup in Section 7.3.1 is used with P_t=0 dBm. Measurements were recorded as Tx-Rx distance varies from 10 cm to 24 cm with a step size of 1 cm. The reason that the Tx-Rx distance stops at 24 cm is because the backscattered power decreased below the noise floor at distances beyond 24 cm. Note that when using a lower carrier frequency, the

maximum distance can reach up to 2 m (demonstrated in Chapter 8) due to lower pathloss. The tag's modulating frequency, f_m, is 900 kHz. We assume that there is no Tx-Rx antenna polarization mismatch.

Figure 72 presents the measured and modeled backscattered power with respect to logic utilization at Tx-Rx distances of 11 cm (black circle), 14 cm (red diamond), and 18 cm (blue triangle). Results show a good agreement between the measured and modeled backscattered power. Figure 73 presents the measured and modeled backscattered power with Tx-

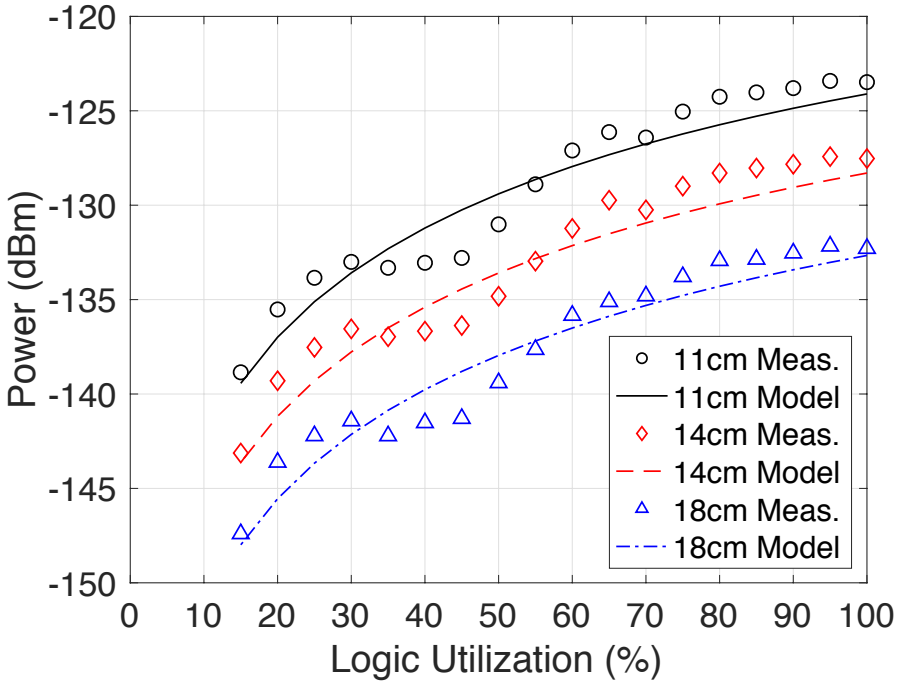

Figure 72: Measured and modeled backscattered power with respect to logic utilization (%) at Tx-Rx distances of 11 cm (black circle), 14 cm (red diamond), and 18 cm (blue triangle).

Rx distance varying from 10 cm to 24 cm with logic utilization (%) of 100 % (black circle), 55 % (red diamond), and 15 % (blue triangle). It can be observed that the model has a good match with the measurements. Interestingly, in contrast to the carrier power in Fig. 70, the backscattered power does not have significant fluctuation as distance increases. We further characterize the shadowing gain (X_σ) of the backscattered power over distance and found that the X_σ follows a log-normal distribution with its logarithmic equivalent having a zero-

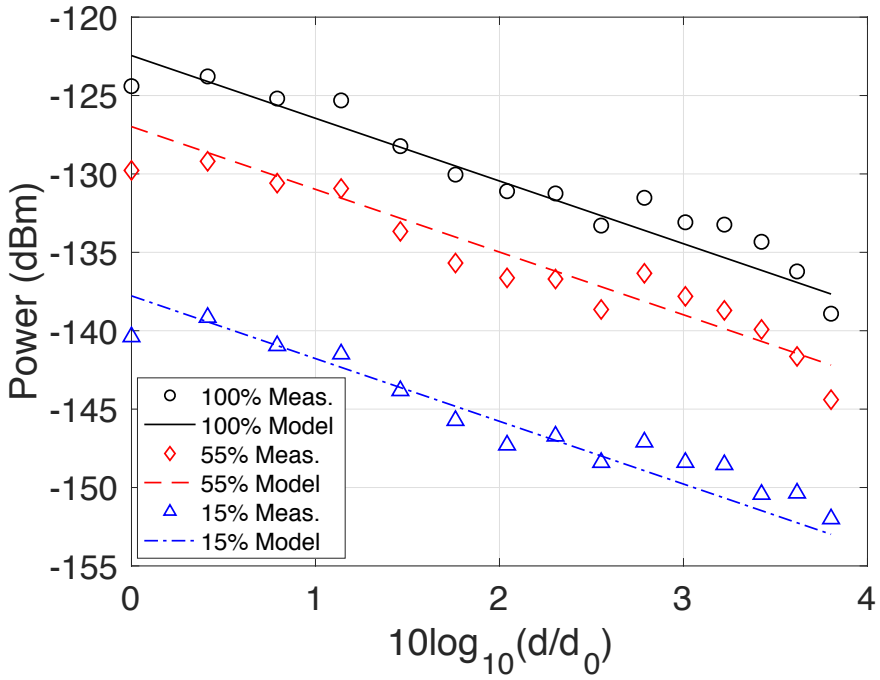

Figure 73: Measured and modeled backscattered power with Tx-Rx distance varying from 10 cm to 24 cm with logic utilization (%) of 100 % (black circle), 55 % (red diamond), and 15 % (blue triangle).

mean (in dB) and standard deviations (σ) of 0.96 dB. CDF of the X_σ is presented in Fig. 74 to confirm the log-normality of the shadowing gain. The backscatter link has a lower σ of 0.96 dB (compared to σ=3.93 dB in the carrier power) since backscatter modulation is a result of the relative amplitude change from the carrier signal. Although the absolute power level of the carrier signal experiences significant fluctuation as distance changes, the backscattered power is not affected by the variation of the carrier power. Therefore, we conclude that the backscattered channel can provide a more reliable link that is resistant to the constructive and destructive interference from the multipaths as compared to the carrier link.

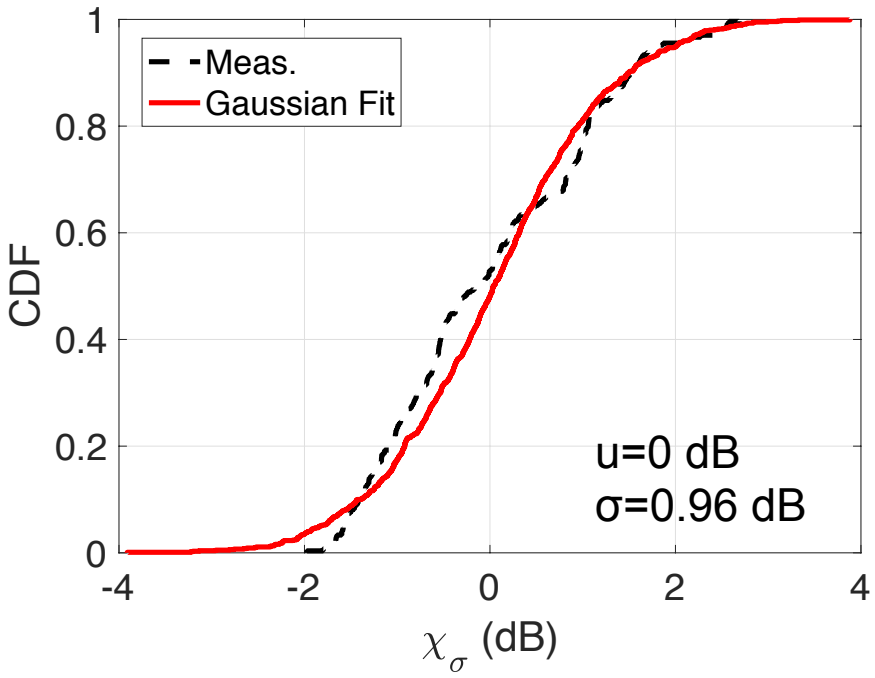

Figure 74: CDF of received backscattered power's shadowing gain (X_σ) measured at 26.5 GHz at d = 10 cm–24 cm.

7.4 Summary

This chapter presents a new propagation model for the antenna-less RFID tag that can be used to estimate the link budget. Detailed derivation of the proposed backscattered power model is provided. Propagation properties such as shadowing gain have been analyzed for the carrier power and the backscattered power. The proposed propagation model has been validated with measurements.

CHAPTER 8

STATIC AND DYNAMIC RFIDS AT 5.8 GHZ, 17 GHZ, 26.5 GHZ, AND 300 GHZ

8.1 Overview

This chapter describes the design methodology of the antenna-less RFID tags and presents the applications of the proposed static and dynamic multi-bit IDs across various interrogating frequencies. To demonstrate that the proposed RFID tag is compatible with a wide range of carrier frequencies, we have tested the following interrogating frequencies: 1) 5.8 GHz, a frequency typically used for RFID communications, 2) 17.46 GHz, a frequency that we have identified to have the highest signal-to-noise ratio (SNR), 3) 26.5 GHz, a frequency that can be used for 5G wireless communications, and 4) 300 GHz, a frequency that belongs to the IEEE 802.15.3d [17] standard for THz communication. Additionally, we have designed a variety of RFID applications to demonstrate the proposed RFID tag's flexible bit-configurations, including *static IDs with 4, 6, 12, and 36 bits*, *multi-bit (4-, 8-, and 12-bit) dynamic RFID tag*, and *single-bit dynamic RFID tag*.

The proposed static ID configurations can transmit up to 36 bits simultaneously and provide up to 68.7 billion (2^{36}) combinations of unique IDs, whereas existing RFID tags with computational chips [123, 124, 125] can only transmit 1 bit simultaneously. The number and pattern of bits are fully re-configurable. This flexible bit design does not occupy additional space on the printed circuit board of the FPGA as the number of bits increases. The proposed dynamic RFID tags with 4 bits, 8 bits, and 12 bits were implemented and all bits were successfully detected. The achieved data rates are comparable with work in [80], where both 16-QAM (quadrature amplitude modulation) and 4-PSK (phase shift keying) RFIDs are designed. We have also tested a single-bit dynamic RFID tag. By transmitting one bit of information at a time to have better SNR, the proposed RFID tag can achieve

a data rate of 100 kbits/sec with a bit error rate (BER) of 0.00000183 (10^{-6}), which is comparable to state-of-the-art RFIDs in [126, 127].

The remainder of the chapter is organized as follows. Section 8.2 describes the design methodology of the antenna-less RFID tags. Section 8.3 describes measurement setup and tests what is the maximum range at which the tag can be operated. Section 8.4 demonstrates applications of the proposed static and dynamic multi-bit IDs across frequencies of 5.8 GHz, 17.46 GHz, 26.5 GHz, and 300 GHz. Finally, Section 8.5 provides some concluding remarks.

8.2 Design Methodology

This section presents the design methodology for the static and dynamic multi-bit IDs. The proposed RFID operates the same as traditional RFID when only one single-bit single-sideband transmission is created. However, when higher data-rate is needed, traditional RFID uses multiple amplitude and/or phase levels and multi-bit modulation schemes to transmit the message in a single-sideband transmission. However, it is also possible to have multiple inverters in the FPGA that switch at different frequencies, allowing for dynamic or static multi-bit designs using frequency modulation. The advantage of multi-frequency design is that receiver design is much simpler. For example, it does not require channel equalization and synchronization and detection is much simpler. To generate multiple bits, multiple shift registers in Fig. 75 are used to switch at different f_m. Parameter M' represents the number of total shift registers. Parameter $N_{M'}$ denotes the number of total configured flip-flops in the M'^{th} shift register. The more flip-flops are configured, the higher SNR can be achieved. Parameter $f_{mM'}$ is the modulating frequency of the M'^{th} shift register, which affects the location of each side band and corresponding bandwidth for the communications.

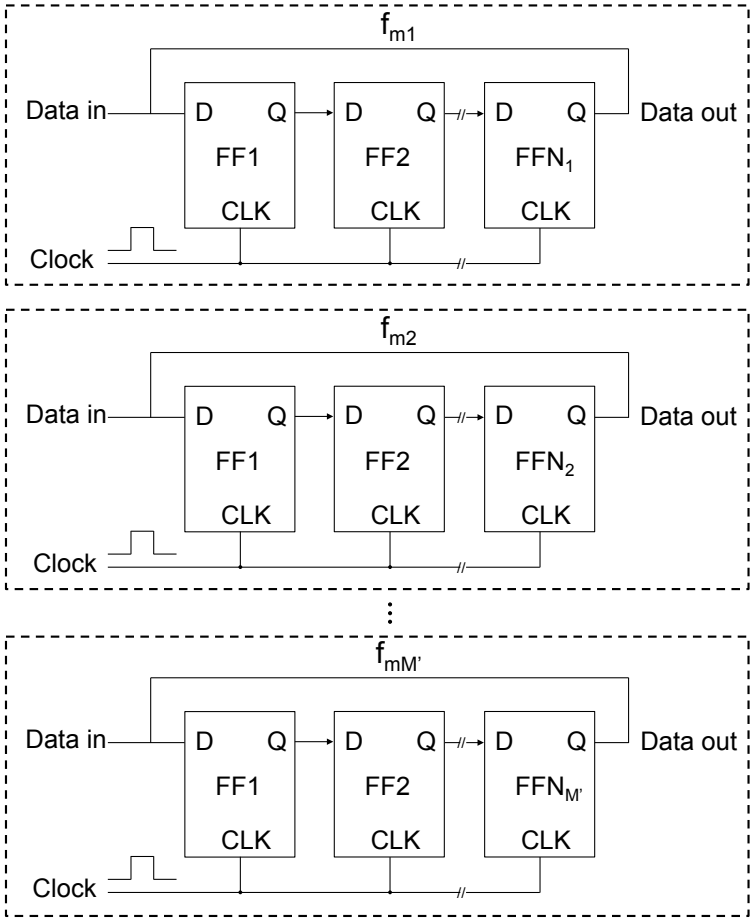

Figure 75: Building blocks of the multi-bit RFID tag. M' is the number of total shift registers (bits). $N_{M'}$ is the number of total configured flip-flops in the M'^{th} shift register. $f_{mM'}$ is the modulating frequency of the M'^{th} shift register.

8.3 Measurement Setup

An Agilent MXG N5183A Signal Generator with input power of 15 dBm (31.6 mW) is used as a signal source and an Agilent MXA N9020A Vector Signal Analyzer is used to record the signals. An Altera DE0-Cyclone V FPGA board is used as the RFID tag as shown in Fig. 68 (a). For interrogation, we use double ridge horn antennas (Com-Power AH-118) shown in Fig. 76 (a) for 5.8 GHz measurements. The double ridge horn antenna operates from 0.7 GHz to 18 GHz with average isotropic gain of 10 dBi. Fig. 76 (c) shows the measurement setup with WR-62 standard gain horn antennas (PE9854/SF-20) operating from 12.4 GHz to 18 GHz with average isotropic gain of 20 dBi that is used for the 17.46

GHz measurement. The measurement setup for the 26.5 GHz measurement is described in Chapter 7.2.1 and Fig. 68 (b). Finally, the 300 GHz measurement setup is presented in Fig. 76 (c), where the same VDI Tx210 and Rx148 THz transceivers introduced in Chapter 3.2 are used. Note that in Figs. 76 (a) and (b), a 3-mm thick plastic case is placed between the Tx/Rx and the FPGA board to demonstrate that the proposed RFID tag can be potentially integrated into electronic devices with plastic enclosures, e.g., laptops, smartphones, tablets, etc. Note that we use different horn antennas because none of them covers all frequencies of interest, i.e., 5.8 GHz, 17.46 GHz, 26.5 GHz, and 300 GHz.

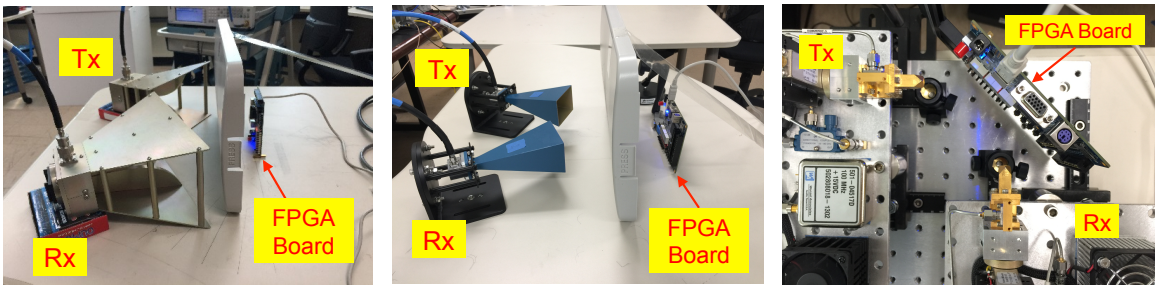

(a) (b) (c)

Figure 76: (a) Altera Cyclone V FPGA board; measurement setup for the (b) 5.8 GHz, (c) 17.46 GHz, (d) 26.5 GHz measurements.

8.3.1 Interrogation Frequency, Distance, and Power Consumption

This section investigates the optimal carrier frequency to interrogate the proposed RFID tag and the maximum distance at which the signal can be received. We use the measurement setup in Fig. 76 (b) with P_t=15 dBm and f_m=900 kHz. After sweeping carrier frequencies from 1 GHz to 18 GHz, we have found that the highest SNR is around 40 dB in the frequency range between 17 and 18 GHz. To test how far away we can receive backscattered signal, we have configured an 1 bit RFID with 100 % logic utilization in order to maximize the SNR and to achieve longer distance. Fig. 77 shows the measured backscatter signal at a distance of 2 m. It is observed that the sideband appears at $f_{carrier}$ + 900 kHz with SNR around 5 dB. Empirically, we have determined that a minimum 2.7 % of total logic resources is needed to provide one observable sideband (bit) with SNR around 3 dB

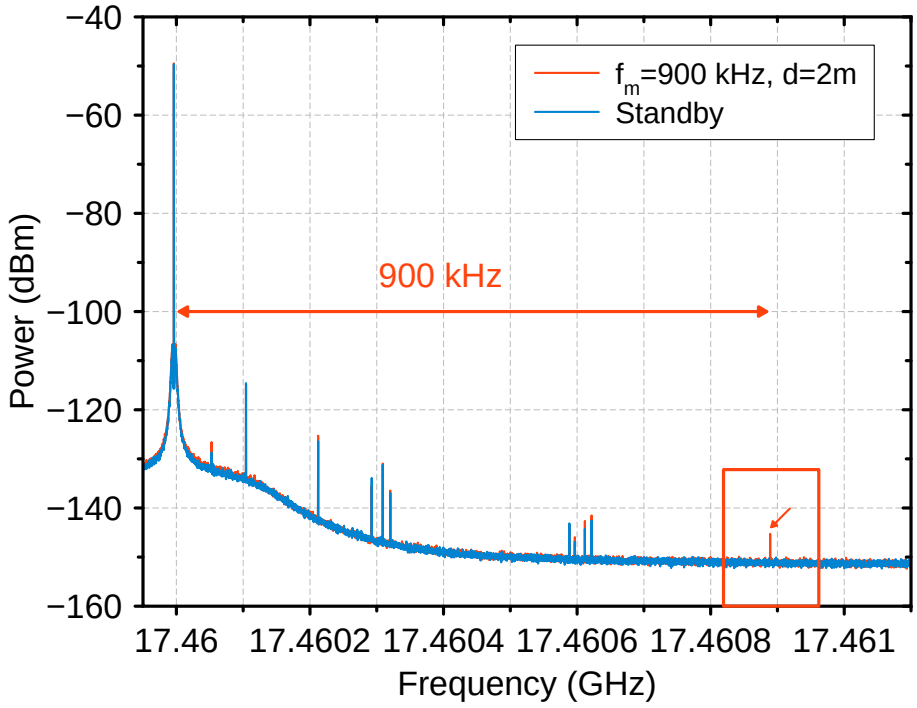

Figure 77: Measurement results of the proposed 1-bit RFID with 100 % logic resources. Distance is set at 2 m. $f_{carrier}$ is set at 17.46 GHz and f_m is set at 900 kHz.

at Tx/Rx-to-tag distance=20 cm. This implies that an FPGA chip can be used for multiple tasks, i.e., enable an RFID tag without interrupting the normal function of the FPGA chip. For example, if an FPGA is configured for intense data processing, we can reduce the number of bits and logic utilization of each bit, e.g., an 1-bit RFID allocated with 8 % of total logic resources, leaving 92 % of free logic resources for data processing; if an FPGA chip is mainly idle, we can increase the number of bits and logic utilization of each bit, e.g., an 8-bit RFID with each bit assigned with 10 % of total logic resources for higher SNR and data rate, leaving 20 % of free logic resources for non-RFID activities, e.g., computing, DSP, etc. Therefore, there is great design flexibility while still supporting normal functionality of an FPGA-based system. Regarding power consumption, given an Altera Cyclone V FPGA configured at 100 % logic utilization, a typical DC current consumption is 8.1 mA with a supply voltage of 1.1 V, which leads to a maximum power consumption of 9.5 dBm (8.91 mW) [128].

8.4 RFID Applications

This section demonstrates that the proposed RFID tag can be used for several different applications across various interrogating frequencies at 5.8 GHz, 17.46 GHz, 26.5 GHz, and 300 GHz: 1) static IDs with 4, 6, 12, and 36 bits; 2) dynamic multi-bit communications; 3) high data rate communications.

8.4.1 Static Multi-Bit IDs

The first application is the static ID with 4 bits, 6 bits, 12 bits, and 36 bits, respectively. The "static" term means that the designed bit pattern does not change over time. Information stored on the tag depends on total number of bits. We use multiple shift registers design described in Fig. 75 to configure multi-bit RFID design. The Tx/Rx-to-tag distance is 20 cm for the 5.8 GHz, 17.46 GHz, and 26.5 GHz measurement, and 10 cm for the 300 GHz measurement.

For the design of 4-bit, 6-bit, 12-bit, and 36-bit RFIDs, f_m is set in a range of 1.39 MHz–2.08 MHz, 860 kHz–1.04 MHz, 700 kHz–1.04 MHz, and 300 kHz–1.04 MHz and 25 %, 15 %, 8.3 %, and 2.7 % of logic resources are assigned to each bit, which contributes a total logic utilization of 100 %, 90 %, 99.7 %, and 97.2 % and a corresponding power consumption of 9.5 dBm (8.91 mW), 9.04 dBm (8.02 mW), 9.49 dBm (8.88 mW), and 9.38 dBm (8.66 mW) [128], respectively. Each bit can be turned on and off individually to generate binary signals 1s and 0s with up to 68.7 billion (2^{36}) combinations of unique IDs. We demonstrate the 4-bit, 6-bit, 12-bit static IDs at 300 GHz, 5.8 GHz, and 26.5 GHz, respectively. The more bits are configured, the less logic resources are assigned to each bit, which requires higher antenna gain to accommodate the lower SNR. As a result, we were able to observe signals for a 36-bit static ID only at 17.46 GHz because it had the highest SNR.

Measurement results are shown in Figs. 78–79. It can be observed that all bits are

clearly identified and separated at least 15 kHz apart with SNRs ranging from 10 dB to 20 dB, providing sufficient margins for signal detection. Our designs demonstrate flexible carrier frequency selection and bits configuration. Note that in Fig. 78 (b), due to attenuation, harmonics of lower sidebands do not cause observable interference to the higher sidebands. The plastic enclosure as obstruction between the tag and the Tx/Rx (shown in

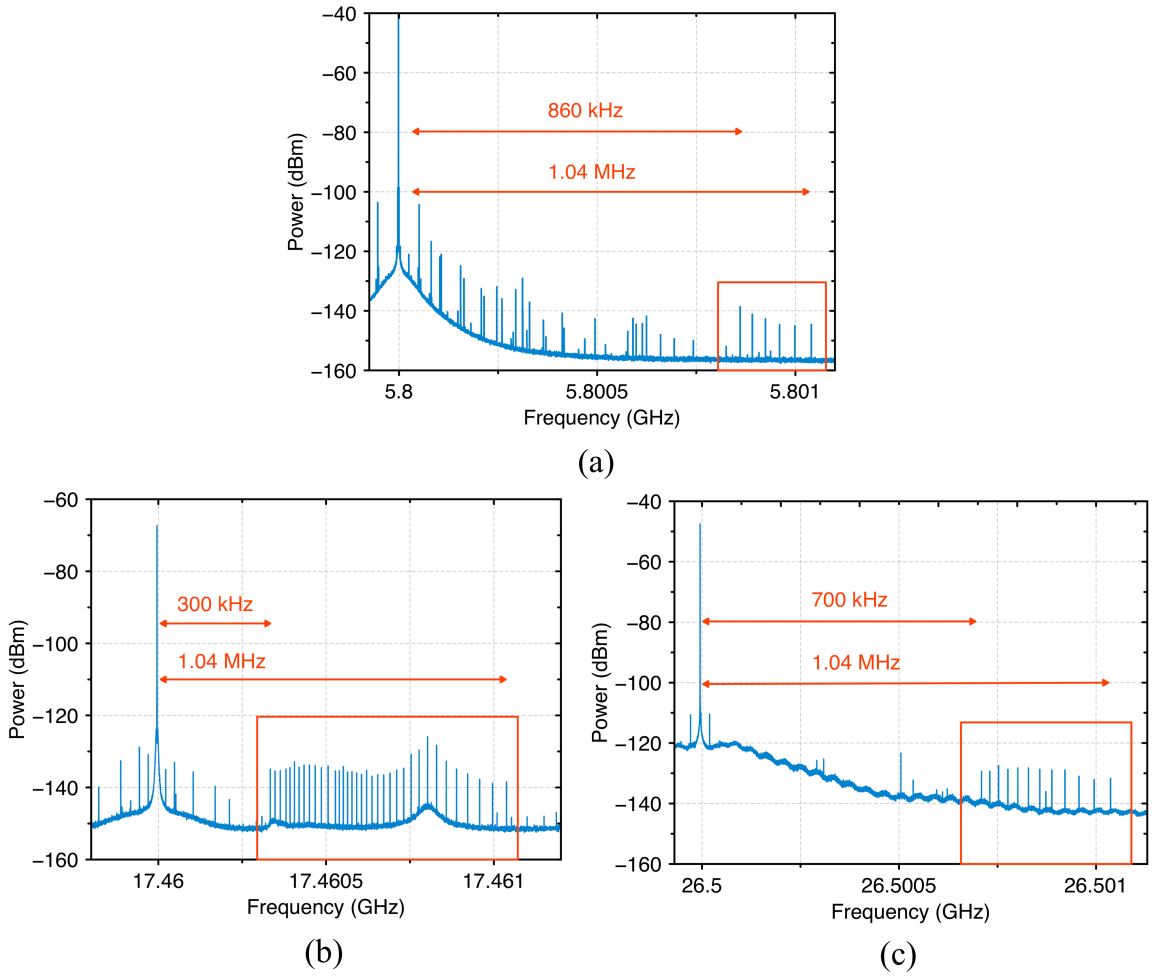

Figure 78: Measurement results of the (a) 5.8 GHz 6-bit static ID with 16% of logic resources assigned to each bit and f_m ranging from 860 kHz to 1.04 MHz; (b) 17.46 GHz 36-bit static ID with 2.7% of logic resources assigned to each bit and f_m ranging from 300 kHz to 1.04 MHz; (c) 26.5 GHz 12-bit static ID with 8% of logic resources assigned to each bit and f_m ranging from 700 kHz to 1.04 MHz.

Figs. 76 (a) and (b)) can cause an extra 1 to 2 dB attenuation. The measurement results shown in Figs. 78–79 are without obstruction for better SNR demonstration.

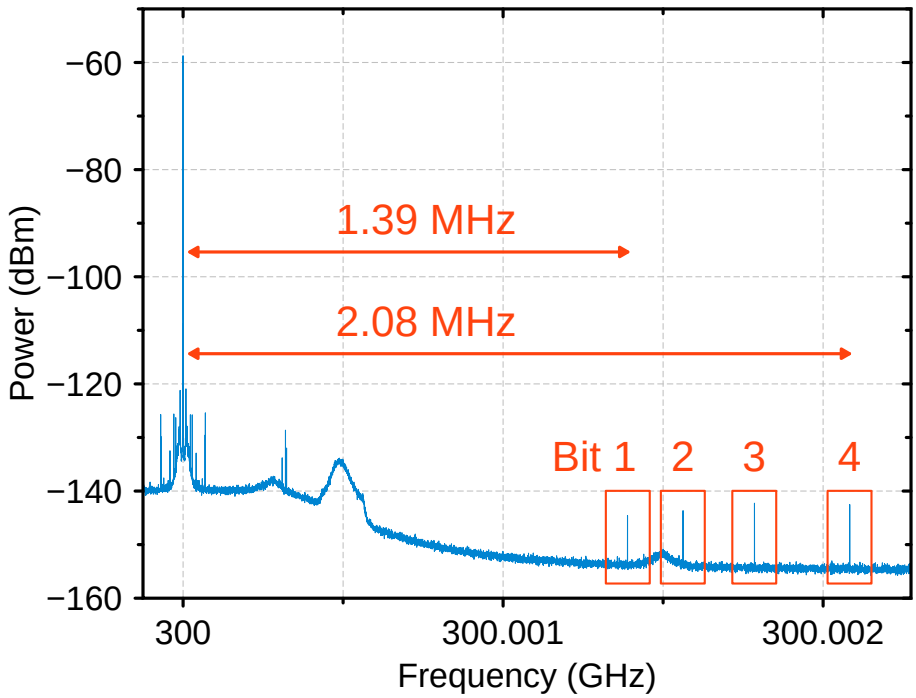

Figure 79: Measurement results of the THz 4-bit static ID with 25% of logic resources assigned to each bit. f_m ranges from 1.39 to 2.08 MHz.

8.4.2 Dynamic Multi-Bit Communications

The second application is dynamic multi-bit communications. The "dynamic" term means the designed bit pattern changes over time. Compared to the static IDs in Section 8.4.1, here an individual bit is turned on and off over time at a switching frequency (f_s) to transmit information. As a result, information stored on the tag is not limited by the total number of bits but depends on f_s and the total transmitting time. We use the design with multiple shift registers described in Fig. 75 to configure the multi-bit RFID design.

We demonstrate the dynamic multi-bit ID at 17.46 GHz and 300 GHz by transmitting specific symbols and showing that the exact symbols are successfully detected at the receiver. For the 17.46 GHz 4-bit, 8-bit, and 12-bit dynamic ID designs, each bit is allocated with 8 % of logic resources and f_s is set at 100 Hz. Consequently, the 4-, 8-, and 12-bit designs have a total logic utilization of 32 %, 64 %, and 96 %, a corresponding data rate

of 400 bits/sec, 800 bits/sec, and 1.2 kbits/sec, and a corresponding power consumption of 4.55 dBm (2.85 mW), 7.56 dBm (5.7 mW), and 9.32 dBm (8.55 mW), respectively. The Tx/Rx-to-tag distance is 20 cm. For the 300 GHz 4-bit dynamic ID design, 25% of logic resources are assigned to each bit, which contributes a total logic utilization of 100% and a maximum power consumption of 9.5 dBm (8.91 mW). f_m is set in a range of 1.67 to 2.5 MHz and f_s is set at 4 Hz, which contributes to a data rate at 16 bits/sec. The Tx/Rx-to-tag distance is 10 cm.

Figure 80 presents symbol patterns measured at the receiver for the 17.46 GHz 4-bit design. Data symbols are designed in the following patterns: (1111), (1000), (1010), (0101), (0011), (0111). The f_m ranges from 1 MHz to 1.14 MHz to accommodate all 4 bits. Measurement results show that all the symbols are successfully detected and match the designed signal patterns. In the 17.46 GHz 8-bit and 12-bit designs, the f_m ranges from 1 MHz to 1.39 MHz and from 1 MHz to 1.79 MHz, respectively. The 8-bit design has symbol patterns of (11111111), (00000000), (10011100), (10000011) and the 12-bit design has symbol patterns of (111111111111), (000000000000), (100000011100), (100000000011). Similarly, all symbols of the 8-bit and 12-bit RFID are successfully detected as shown in Figs. 81 and 82. Note that the plastic enclosure as obstruction between the tag and the Tx/Rx (shown in Fig. 76 (b)) can cause an extra 1 to 2 dB attenuation. The measurement results shown in Figs. 80–82 are without obstruction for better SNR demonstration. Measurement results of the 300 GHz 4-bit dynamic ID is presented in Fig. 83. Data symbols are designed in the following patterns: (1000), (1010), (0101), (0011), (0111). The f_m ranges from 1.67 MHz to 2.5 MHz to accommodate all 4 bits. Measurement results show that all the symbols are successfully detected and match the designed signal patterns.

8.4.3 Dynamic Single-Bit Communications With Maximum Data Rate

The third application provides high data rate communication between the interrogator and the tag. We have designed a 1 bit RFID with 100 % logic utilization and maximum power

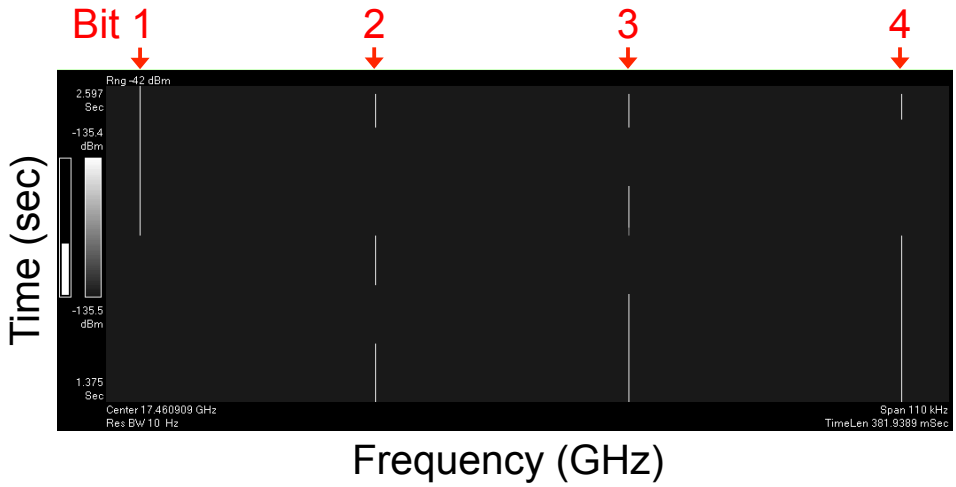

Figure 80: Measurement results of 17.46 GHz 4-bit RFID for dynamic communications. f_m ranges from 1 MHz to 1.14 MHz. Symbol patterns: (1111), (1000), (1010), (0101), (0011), (0111).

consumption of 9.5 dBm (8.91 mW) to maximize SNR. The f_m is set at 1.92 MHz and the f_s is set at 100 kHz, providing a data rate of 100 kbits/sec. The interrogation frequency is 17.46 GHz and the Tx/Rx-to-tag distance is 20 cm. In order to estimate the bit error rate (BER), we use the VSA with a sampling rate of 2.56 MHz to record more than 1 million transmitting bits (1091227 bits) for around 11 seconds. The RFID tag modulates the carrier signals with a testing symbol pattern of (111010). Fig. 84 presents the measured signal strength of the transmitted symbols. The solid curve is the modulated backscatter signal measured by the VSA, while red circles are post-measurement signal processing sampled signals. In order to detect bit 0 and bit 1, a threshold value of -81 dBm is chosen since it provides the lowest BER. Our signal processing results show that only 2 errors are detected among all 1091227 transmitted bits, that is, our proposed RFID tag achieves a BER of 0.00000183 (10^{-6}) at a data rate of 100 kbits/sec. Note that the plastic enclosure as obstruction between the tag and the Tx/Rx (shown in Fig. 76 (b)) can cause extra 1 to 2 dB attenuation. The measurement results shown in Fig. 84 are without obstruction for better SNR demonstration.

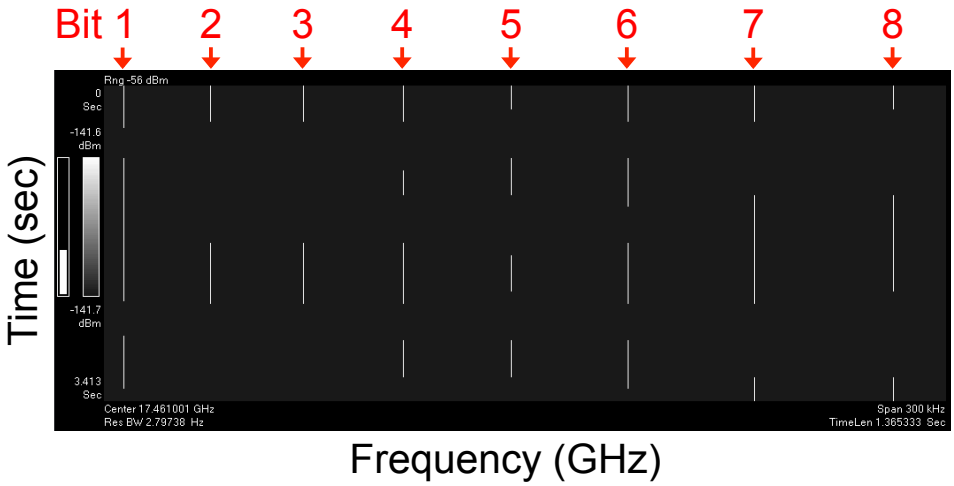

Figure 81: Measurement results of 17.46 GHz 8-bit RFID for dynamic communications. f_m ranges from 1 MHz to 1.39 MHz. Symbol patterns: (11111111), (00000000), (10011100), (10000011).

8.5 Summary

This chapter introduces the design methodology of the antenna-less RFID tags. The proposed RFID tag can be interrogated at a wide frequency range from 5.8 GHz up to 300 GHz. The proposed RFID applications demonstrate flexible bit configurations, such as static IDs with 4, 6, 12, and 36 bits, which provide up to 68.7 billion (2^{36}) combinations of unique IDs, and multi-bit (4-, 8-, and 12-bit) dynamic RFIDs for communications. A maximum data rate of 100 kbits/sec with a bit error rate (BER) of 0.00000183 (10^{-6}) is achieved.

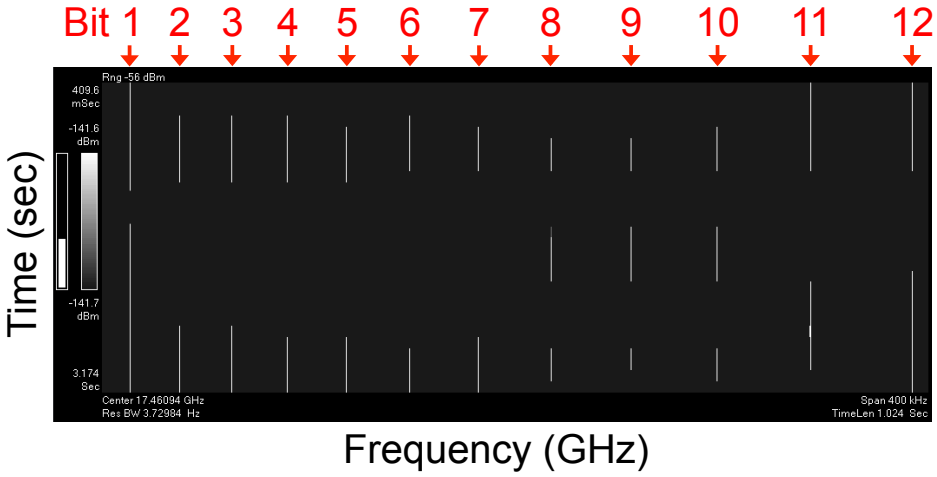

Figure 82: Measurement results of 17.46 GHz 12-bit RFID for dynamic communications. f_m ranges from 1 MHz to 1.79 MHz. Symbol patterns: (111111111111), (000000000000), (100000011100), (100000000011).

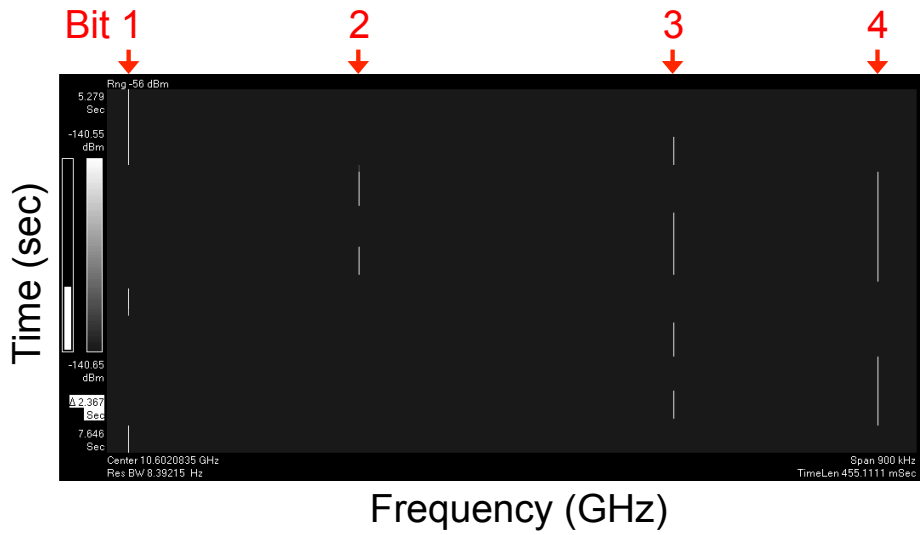

Figure 83: Measurement results of the THz 4-bit dynamic ID with f_m ranging from 1.67 to 2.5 MHz. A center frequency of 10.6 GHz presented in the figure is the $\mathrm{R_x}$ output frequency down converted from the interrogating frequency at 300 GHz. Symbol patterns: (1000), (1010), (0101), (0011), (0111), (1000), (0010), (0001), (0011).

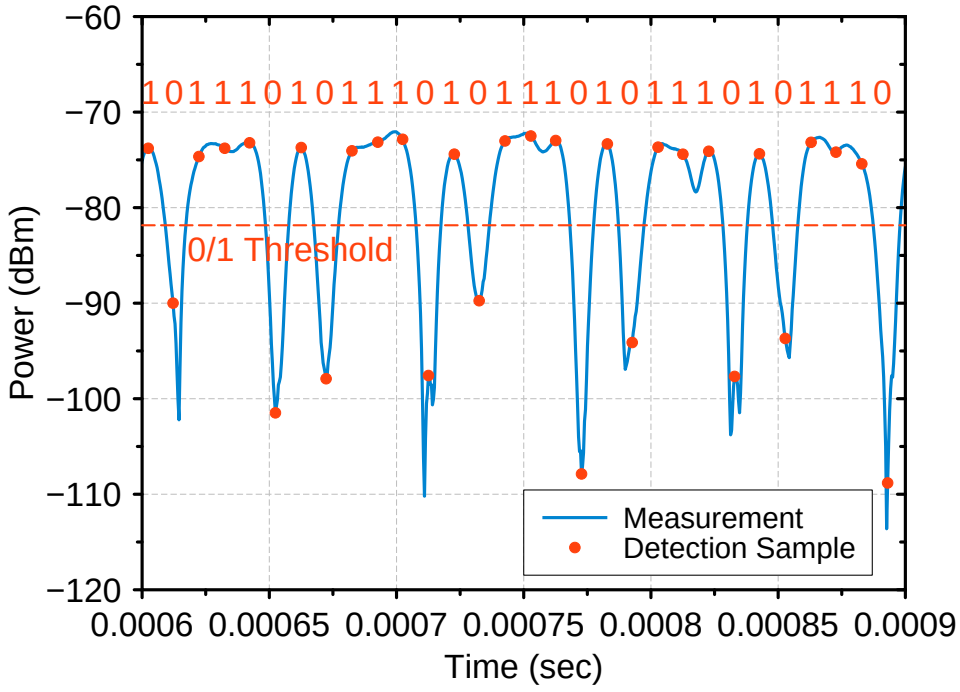

Figure 84: Measured signal strength of the transmitted symbols. The solid curve is the modulated backscatter signal while red circles are the post-measurement signal processing sampled signals. A threshold value is set at -81 dBm to detect a symbol pattern of (111010).

CHAPTER 9

RESEARCH CONTRIBUTIONS AND FUTURE RESEARCH DIRECTIONS

9.1 Research Contributions

The ever-growing demand on the capacity of wireless communication indicates that data rates will reach Terabit-per-second (Tbps) in the coming years. Terahertz (THz) bands (300 GHz–10 THz) provide abundant unregulated bandwidth to realize Tbps high speed links. This thesis addresses two problems needed to be solved to enable Tbps data rates: 1) characterize and model wireless channels in data centers and 2) design THz antenna-less RFID tags that can further reduce the device size by not using antennas and have potential to attain ultra high data rates. The contributions of our research are summarized as follows.

- The development of THz wireless system in data centers would require the characterization and modeling of the propagation channel in which such a device will operate. To understand the THz propagation channel in a data center environment, channel sounding in a mock-up data center model has been conducted as a starting point, which allows for more flexibility exploring a variety of potential propagation scenarios. Detailed characterization of 300 GHz channels has been conducted in a mock-up data center model for wireless R2R and B2B communications. Measurements are performed in R2R LoS, R2R OLoS, R2R RNLoS, R2R ORNLoS, B2B RNLoS, B2B ORNLoS, and B2B LoS scenarios, which evaluate the impact of Tx/Rx misalignment and obstructions such as cables, metal cabinets, and mesh structures on THz propagation, as well as possibility of using existing metal objects as reflectors that guide waves for NLoS type of links. For the R2R LoS scenario, the channel with optical lenses acts as a waveguide with a PLE of 1.48 and the optical lenses provide additional gain of more than 25 dB. PDPs reveal that optical lenses can cause additional

multiple reflections. When obstructions of cables are present, ORNLoS link outperforms OLoS link with 2.5 dB lower shadowing gain and weaker multipath. For the B2B scenario, a dual-reflector THz transceiver rack system has been proposed to enable wireless links across vertically stacked servers and allow easy maintenance and repair of servers. The measured path loss approximates the Friis values in the LoS link and in the RNLoS link with hollow vertical ground plane. Hollow rack structure is preferred over solid metal due to its minimum reflection interference. When obstructions of cables are present, the ORNLoS link experiences 5–10 dB higher path loss and on average 0.25 GHz lower B_c than the RNLoS link. Measured statistical channel properties show that the shadowing gain caused by cable clusters follows the log-normal distribution. Furthermore, Doppler shift in THz bands due to the effect of cooling airflow turbulence, which causes cables to vibrate has also been measured. Consequently, a 2-D geometrical propagation model that includes moving scatterers is introduced for modeling the Doppler shift. From the 2-D model, the corresponding DPS is derived and validated with measured data. Results show that a maximum Doppler frequency is observed as 56.1 Hz. [51, 52, 53, 28, 54, 55].

- Inside a data center, high performance computing servers with metal enclosures are vertically stacked up in metallic server racks, and rows of server racks are arranged in parallel separated by aisles. Each server rack has a movable door with mesh structure that allows for circulation of the cooling airflow. Exposed cable clusters, e.g., power cables and auxiliary cables, exist between the server racks and server machines. This constitutes a unique propagation channel, whose properties need to be explored. Therefore, a THz channel measurement campaign has been conducted in a realistic data center environment. Various propagation scenarios such as LoS, NLoS, OLoS, and ONLoS links have been studied. Channel properties such as pathloss, PDP, and delay spread have been analyzed. It has been found that optical lenses can provide additional gain of 29.3 dB in the LoS link at d $=$ 175 cm, and 12.6 dB in

the NLoS link at a path length of 282 cm, respectively. It has also been found that cables and mesh structure can cause additional attenuation of about 20 dB and 6 dB, respectively. Existing objects in data centers, e.g., Server-rack frames/pillars, serve as ideal reflectors for the NLoS type of link. Furthermore, the Tx/Rx misalignment tolerance range is found to approximate the diameter of the lens, and the impact of cooling airflow on THz propagation can be overlooked. Towards diversity reasons, a 4×4 *virtual* MIMO uniform linear array (ULA) has been applied for the characterization of a 4×4 MIMO channel with cables serving as obstruction. The statistics of amplitude fading in the MIMO channel have been investigated with results showing an m-Nakagami distribution fit and a linear dependency on delay bins. [56, 55].

- From the measurement campaign conducted in a data center, it can be observed that multipath components (MPCs) naturally group into clusters in some of the measurement scenarios. Therefore, a cluster-based propagation model for THz propagation in a data center environment has been proposed in such scenarios. Cluster-based models have been widely used for indoor propagation channels across a wide range of frequency spectra, from microwave (cellular), ultra-wideband (UWB), mm-wave, up to THz bands. Clustering in the delay domain directly affects the delay spread, which is important in determining the need for employing channel protection techniques, e.g., channel equalization, channel coding, or channel diversity to overcome the dispersive effects of multipaths. Regardless of such wide applicability and the aforementioned importance, no cluster-based model has been developed for THz propagation channels in data center environments. This thesis presents a cluster-based propagation model for THz propagation in a data center environment. The proposed model is validated with measured data, where the average numbers of clusters and rays are estimated as 3 and 4, respectively, and the average inter-arrival time of clusters ($1/\Lambda$) and rays ($1/\lambda$) are estimated as 4.4 ns and 0.24 ns, respectively. [56].

- Traditional backscatter communication refers to a radio channel where a reader sends a continuous carrier wave (CW) signal to a tag and retrieves information from a modulated wave scattered back from the tag. During backscatter operation, the input impedance of a tag antenna is intentionally mismatched by two-state RF loads (Z_0 and Z_1) to vary the tag's reflection coefficient and radar cross section (RCS) and to modulate the incoming CW. However, the form factor of existing RFID tags have limited room for further miniaturization since they all need to use antennas, which are the largest parts of the tag. To further miniaturize the backscatter communication systems and enhance the coding capacity, a new backscatter architecture that can operate without antennas and is compatible with a wide range of interrogating carrier frequencies is needed. This thesis introduces the THz antenna-less RFID tag based on a new backscatter radio generated from switching of transistors in digital electronics, which does not need to use antennas or any RF front-end circuits thereby further reducing the device's form factor. Moreover, the proposed antenna-less RFID tags are compatible with a wide range of interrogating carrier frequencies from sub-6 GHz up to 300 GHz, and can be implemented on existing electronics without additional cost. Since this is a new type of backscatter communication, the backscatter mechanism needs to be addressed. Therefore, a circuit impedance model that explains the modulation mechanism of the new backscatter radio and describes the relation between the total input impedance and the logic resources of the digital circuits has been developed. The procedure of estimating the impedance (resistance and reactance) of the antenna-less RFID tag is also presented. [57].

- A complete propagation model for traditional backscatter radio systems is required to assess the link budget, which is important for evaluating the feasibility and reliability of a wireless link. However, the existing backscatter propagation model does not provide the estimation of the modulation loss resulting from the switching activity of the digital electronics, and thus cannot be directly applied to the proposed

antenna-less backscatter radio link. To address this need, this thesis introduces a new propagation model for the antenna-less RFID tag. The proposed propagation model consists of a modulation loss factor (due to the switching of transistors) that is derived from the proposed circuit impedance model, and can be used to estimate a link budget. Detailed derivation of the proposed backscattered power model and validation with measurements are provided. The shadowing gain for the carrier power and the backscattered power has also be characterized. Results show that the backscattered channel can provide a more reliable link that is resistant to the constructive and destructive interference from the multipaths as compared to the carrier link.

- A design methodology of the antenna-less RFID tags has been introduced and the applications of the proposed static and dynamic multi-bit IDs across various interrogating frequencies have been presented. To demonstrate that the proposed RFID tag is compatible with a wide range of carrier frequencies, the following interrogating frequencies have been tested: 1) 5.8 GHz, a frequency typically used for RFID communications, 2) 17.46 GHz, a frequency that we have identified to have the highest signal-to-noise ratio (SNR), 3) 26.5 GHz, a frequency that can be used for 5G wireless communications, and 4) 300 GHz, a frequency that belongs to the IEEE 802.15.3d standard for THz communication proposes. Additionally, we have designed a variety of RFID applications to demonstrate the proposed RFID tag's flexible bit-configurations, including *static IDs with 4, 6, 12, and 36 bits*, *multi-bit (4, 8, and 12 bit) dynamic RFID tag*, and *single-bit dynamic RFID tag*. The proposed static ID configurations can transmit up to 36 bits simultaneously and provide up to 68.7 billion (2^{36}) combinations of unique IDs, whereas existing traditional RFID tags with computational chips can only transmit 1 bit simultaneously. The bit number and bit pattern of the proposed RFID tags are fully re-configurable. This flexible bit design does not occupy additional space on the printed circuit board of the FPGA as the number of bits increases. The proposed dynamic RFID tags with 4 bits, 8 bits,

and 12 bits were implemented and all bits were successfully detected. A single-bit dynamic RFID tag with maximum data rate has also been tested. By transmitting one bit of information at a time to have better SNR, the proposed RFID tag can achieve a data rate of 100 kbits/sec with a bit error rate (BER) of 0.00000183 (10^{-6}). [57, 58].

9.2 Future Research Directions

In this thesis, we have developed a cluster-based propagation model for THz propagation in a data center environment. The proposed model has been validated with measured data. Although the measurement designs and results provided in this thesis are the starting point for realistic performance evaluations and designs of THz communication systems in a data center environment, to acquire a more generalized statistical characterization of the clustering model, complementary measurements in other data centers with multiple Tx/Rx positions would be required to validate how much the model parameters change from data center to data center. Hence, the future research efforts may be devoted to generalizing the clustering model by expanding the measurement campaign to multiple data centers. Furthermore, in this thesis, channel properties of THz propagation in a data center have been analyzed from a physical point of view in terms of pathloss exponent, shadowing gain, and RMS delay spread. Another possible enhancement is to conduct channel characterization from a communication perspective with transmission of real modulated data packets through various scenarios such as the LoS, OLoS, NLoS, and ONLoS links, and to provide evaluation on modulation schemes and estimation of channel capacity, peak data rate, and BER.

This thesis has also proposed a THz antenna-less RFID tag that can be interrogated with carrier frequencies from sub-6 GHz up to 300 GHz. To fully utilize this new antenna-less backscatter radio in the THz frequencies and achieve high data rate, the SNR of the backscattered signal needs to be enhanced. Our preliminary work in [57] proposed that specialized circuits, e.g., application specific integrated circuits (ASICs), can be fabricated to further optimize the impedance difference between inverter's high output and low out-

put state to enhance backscattered signal strength. However, [57] only provided simulation results, while the ASIC is not fabricated and measurement results are not available. Therefore, the future research efforts may be directed toward investigating the possibility of implementing the proposed antenna-less RFID tags on ASICs to enhance backscattered signal strength. Moreover, all of the proposed RFID applications are demonstrated using the Altera Cyclone V FPGA board. Another possible extension of our work is to explore the possibility of implementing the proposed antenna-less RFID tags on other types and models of microprocessors.

REFERENCES

[1] T. Rappaport, *Wireless Communications: Principles and Practice*, 2nd. Upper Saddle River, NJ, USA: Prentice Hall PTR, 2001, ISBN: 0130422320.

[2] A. Singh, J. Ong, A. Agarwal, G. Anderson, A. Armistead, R. Bannon, S. Boving, G. Desai, B. Felderman, P. Germano, and et al., "Jupiter rising: A decade of clos topologies and centralized control in googles datacenter network," *SIGCOMM Comput. Commun. Rev.*, vol. 45, no. 4, 183197, Aug. 2015.

[3] H. Vardhan, N. Thomas, S. R. Ryu, B. Banerjee, and R. Prakash, "Wireless data center with millimeter wave network," in *IEEE Global Telecommunications Conference GLOBECOM 2010*, Dec. 2010, pp. 1–6.

[4] E. Baccour, S. Foufou, R. Hamila, and M. Hamdi, "A survey of wireless data center networks," in *49th Annual Conference on Information Sciences and Systems (CISS)*, Mar. 2015, pp. 1–6.

[5] K. Ramachandran, R. Kokku, R. Mahindra, and S. Rangarajan, "60 ghz data-center networking: Wireless = worry less?" In *NEC Technical Report*, Jul. 2008.

[6] T. Chen, X. Gao, and G. Chen, "The features, hardware, and architectures of data center networks: A survey," *Journal of Parallel and Distributed Computing*, vol. 96, pp. 45–74, Oct. 2016.

[7] W. Zhang, X. Zhou, L. Yang, Z. Zhang, B. Y. Zhao, and H. Zheng, "3d beamforming for wireless data centers," in *Proceedings of the 10th ACM Workshop on Hot Topics in Networks*, ser. HotNets-X, Cambridge, Massachusetts: ACM, Nov. 2011, 4:1–4:6, ISBN: 978-1-4503-1059-8.

[8] X. Zhou, Z. Zhang, Y. Zhu, Y. Li, S. Kumar, A. Vahdat, B. Y. Zhao, and H. Zheng, "Mirror mirror on the ceiling: Flexible wireless links for data centers," in *Proceedings of the ACM SIGCOMM Conference on Applications, Technologies, Architectures, and Protocols for Computer Communication*, ser. SIGCOMM '12, Helsinki, Finland: ACM, Aug. 2012, pp. 443–454, ISBN: 978-1-4503-1419-0.

[9] C. Zhang, F. Wu, X. Gao, and G. Chen, "Free talk in the air: A hierarchical topology for 60 ghz wireless data center networks," *IEEE/ACM Transactions on Networking*, vol. 25, no. 6, pp. 3723–3737, Dec. 2017.

[10] D. Halperin, S. Kandula, J. Padhye, P. Bahl, and D. Wetherall, "Augmenting data center networks with multi-gigabit wireless links," *SIGCOMM Comput. Commun. Rev.*, vol. 41, no. 4, pp. 38–49, Aug. 2011.

[11] J. Y. Shin, E. G. Sirer, H. Weatherspoon, and D. Kirovski, "On the feasibility of completely wireless datacenters," in *ACM/IEEE Symposium on Architectures for Networking and Communications Systems (ANCS)*, Oct. 2012, pp. 3–14.

[12] Y. Cui, H. Wang, X. Cheng, and B. Chen, "Wireless data center networking," *IEEE Wireless Communications*, vol. 18, no. 6, pp. 46–53, Dec. 2011.

[13] A. Davy, L. Pessoa, C. Renaud, E. Wasige, M. Naftaly, T. Kürner, G. George, O. Cojocari, N. O. Mahony, and M. A. G. Porcel, "Building an end user focused thz based ultra high bandwidth wireless access network: The terapod approach," in *9th International Congress on Ultra Modern Telecommunications and Control Systems and Workshops (ICUMT)*, Nov. 2017, pp. 454–459.

[14] B. Peng and T. Kürner, "A stochastic channel model for future wireless thz data centers," in *International Symposium on Wireless Communication Systems (ISWCS)*, Aug. 2015, pp. 741–745.

[15] *Compare cables that are tangled together and cables organized beautifully like art*, `https://gigazine.net/gsc_news/en/20081020_dirty_clean_cable/`, Gigazine, 2008.

[16] A. S. Hamza, J. S. Deogun, and D. R. Alexander, "Wireless communication in data centers: A survey," *IEEE Communications Surveys Tutorials*, vol. 18, no. 3, pp. 1572–1595, 2016.

[17] "Ieee standard for high data rate wireless multi-media networks–amendment 2: 100 gb/s wireless switched point-to-point physical layer," *IEEE Std 802.15.3d-2017 (Amendment to IEEE Std 802.15.3-2016 as amended by IEEE Std 802.15.3e-2017)*, pp. 1–55, Oct. 2017.

[18] I. F. Akyildiz, C. Han, and S. Nie, "Combating the distance problem in the millimeter wave and terahertz frequency bands," *IEEE Communications Magazine*, vol. 56, no. 6, pp. 102–108, Jun. 2018.

[19] N. Khalid and O. B. Akan, "Experimental throughput analysis of low-thz mimo communication channel in 5g wireless networks," *IEEE Wireless Communications Letters*, vol. 5, no. 6, pp. 616–619, Dec. 2016.

[20] S. Mollahasani and E. Onur, "Evaluation of terahertz channel in data centers," in *NOMS 2016 - 2016 IEEE/IFIP Network Operations and Management Symposium*, Apr. 2016, pp. 727–730.

[21] V. Petrov, J. Kokkoniemi, D. Moltchanov, J. J. Lehtomäki, Y. Koucheryavy, and M. J. Juntti, "Last meter indoor terahertz wireless access: Performance insights and implementation roadmap," *IEEE Communications Magazine*, vol. 56, no. 6, pp. 158–165, Jun. 2018.

[22] N. Boujnah, S. Ghafoor, and A. Davy, "Modeling and link quality assessment of thz network within data center," in *2019 European Conference on Networks and Communications (EuCNC)*, Jun. 2019, pp. 57–62.

[23] J. M. Eckhardt, T. Doeker, S. Rey, and T. Kürner, "Measurements in a real data centre at 300 ghz and recent results," in *2019 13th European Conference on Antennas and Propagation (EuCAP)*, Mar. 2019, pp. 1–5.

[24] T. Kürner, G. M. Ke, A. F. Molisch, A. Bo, H. Ruisi, L. Guangkai, T. Li, D. Jianwu, and Z. Zhangdui, "Millimeter wave and thz propagation channel modeling for high-data rate railway connectivity—status and open challenges," in *ZTE Commun.*, vol. 14, Dec. 2016.

[25] S. Kim and A. Zajić, "Characterization of 300-ghz wireless channel on a computer motherboard," *IEEE Transactions on Antennas and Propagation*, vol. 64, no. 12, pp. 5411–5423, Dec. 2016.

[26] S. Kim and A. G. Zajić, "Statistical characterization of 300-ghz propagation on a desktop," *IEEE Transactions on Vehicular Technology*, vol. 64, no. 8, pp. 3330–3338, Aug. 2015.

[27] S. Kim and A. Zajić, "Statistical modeling and simulation of short-range device-to-device communication channels at sub-thz frequencies," *IEEE Transactions on Wireless Communications*, vol. 15, no. 9, pp. 6423–6433, Sep. 2016.

[28] C.-L. Cheng, S. Kim, and A. Zajić, "Comparison of path loss models for indoor 30 ghz, 140 ghz, and 300 ghz channels," in *11th European Conference on Antennas and Propagation (EUCAP)*, Mar. 2017, pp. 716–720.

[29] J. Fu, P. Juyal, and A. Zajić, "300 ghz channel characterization of chip-to-chip communication in metal enclosure," in *2019 13th European Conference on Antennas and Propagation (EuCAP)*, Mar. 2019, pp. 1–5.

[30] A. A. M. Saleh and R. Valenzuela, "A statistical model for indoor multipath propagation," *IEEE Journal on Selected Areas in Communications*, vol. 5, no. 2, pp. 128–137, Feb. 1987.

[31] S. Sangodoyin, V. Kristem, A. F. Molisch, R. He, F. Tufvesson, and H. M. Behairy, "Statistical modeling of ultrawideband mimo propagation channel in a warehouse

environment," *IEEE Transactions on Antennas and Propagation*, vol. 64, no. 9, pp. 4049–4063, Sep. 2016.

[32] S. Sangodoyin, V. Kristem, C. U. Bas, M. Käske, J. Lee, C. Schneider, G. Sommerkorn, C. J. Zhang, R. Thomä, and A. F. Molisch, "Cluster characterization of 3-d mimo propagation channel in an urban macrocellular environment," *IEEE Transactions on Wireless Communications*, vol. 17, no. 8, pp. 5076–5091, Aug. 2018.

[33] F. Fuschini, S. Häfner, M. Zoli, R. Müller, E. M. Vitucci, D. Dupleich, M. Barbiroli, J. Luo, E. Schulz, V. Degli-Esposti, and R. S. Thomä, "Analysis of in-room mm-wave propagation: Directional channel measurements and ray tracing simulations," *Journal of Infrared, Millimeter, and Terahertz Waves*, vol. 38, no. 6, pp. 727–744, Jun. 2017.

[34] S. Salous, V. Degli Esposti, F. Fuschini, D. Dupleich, R. Müller, R. S. Thomä, K. Haneda, J.-M. Molina Garcia-Pardo, J. Pascual Garcia, D. P. Gaillot, M. Nekovee, and S. Hur, "Millimeter-wave propagation: Characterization and modeling toward fifth-generation systems. [wireless corner]," *IEEE Antennas and Propagation Magazine*, vol. 58, no. 6, pp. 115–127, Dec. 2016.

[35] C. Gustafson, K. Haneda, S. Wyne, and F. Tufvesson, "On mm-wave multipath clustering and channel modeling," *IEEE Transactions on Antennas and Propagation*, vol. 62, no. 3, pp. 1445–1455, Mar. 2014.

[36] N. Iqbal, J. Luo, R. Müller, G. Steinböck, C. Schneider, D. A. Dupleich, S. Häfner, and R. S. Thomä, "Multipath cluster fading statistics and modeling in millimeter-wave radio channels," *IEEE Transactions on Antennas and Propagation*, vol. 67, no. 4, pp. 2622–2632, Apr. 2019.

[37] S. Priebe, M. Jacob, and T. Kürner, "Aoa, aod and toa characteristics of scattered multipath clusters for thz indoor channel modeling," in *17th European Wireless 2011 - Sustainable Wireless Technologies*, Apr. 2011, pp. 1–9.

[38] S. Priebe and M. Jacob and T. Kürner, "Angular and rms delay spread modeling in view of thz indoor communication systems," *Radio Science*, vol. 49, no. 3, pp. 242–251, Mar. 2014.

[39] Y. Choi, "Performances and feasibility of thz indoor communication for multi-gigabit transmission," in *2013 1st International Conference on Artificial Intelligence, Modelling and Simulation*, Dec. 2013, pp. 446–450.

[40] H. Asplund, A. A. Glazunov, A. F. Molisch, K. I. Pedersen, and M. Steinbauer, "The cost 259 directional channel model-part ii: Macrocells," *IEEE Transactions on Wireless Communications*, vol. 5, no. 12, pp. 3434–3450, Dec. 2006.

[41] H. Stockman, "Communication by means of reflected power," *Proceedings of the IRE*, vol. 36, no. 10, pp. 1196–1204, Oct. 1948.

[42] J. D. Griffin and G. D. Durgin, "Complete link budgets for backscatter-radio and rfid systems," *IEEE Antennas and Propagation Magazine*, vol. 51, no. 2, pp. 11–25, Apr. 2009.

[43] P. Pursula, T. Vaha-Heikkila, A. Muller, D. Neculoiu, G. Konstantinidis, A. Oja, and J. Tuovinen, "Millimeter-wave identification–a new short-range radio system for low-power high data-rate applications," *IEEE Transactions on Microwave Theory and Techniques*, vol. 56, no. 10, pp. 2221–2228, Oct. 2008.

[44] P. Pursula, F. Donzelli, and H. Seppä, "Passive rfid at millimeter waves," *IEEE Transactions on Microwave Theory and Techniques*, vol. 59, no. 8, pp. 2151–2157, Aug. 2011.

[45] J. G. D. Hester and M. M. Tentzeris, "A mm-wave ultra-long-range energy-autonomous printed rfid-enabled van-atta wireless sensor: At the crossroads of 5g and iot," in *2017 IEEE MTT-S International Microwave Symposium (IMS)*, Jun. 2017, pp. 1557–1560.

[46] P. F. Freidl, M. E. Gadringer, D. Amschl, and W. Bcõsch, "Mm-wave rfid for iot applications," in *2017 Integrated Nonlinear Microwave and Millimetre-wave Circuits Workshop (INMMiC)*, Apr. 2017, pp. 1–3.

[47] C. Carlowitz, A. Strobel, T. Schäfer, F. Ellinger, and M. Vossiek, "A mm-wave rfid system with locatable active backscatter tag," in *2012 IEEE International Conference on Wireless Information Technology and Systems (ICWITS)*, Nov. 2012, pp. 1–4.

[48] M. El-Absi, A. Alhaj Abbas, A. Abuelhaija, F. Zheng, K. Solbach, and T. Kaiser, "High-accuracy indoor localization based on chipless rfid systems at thz band," *IEEE Access*, vol. 6, pp. 54 355–54 368, Sep. 2018.

[49] M. Hamdi, F. Garet, L. Duvillaret, P. Martinez, and G. Eymin-Petot-Tourtollet, "New approach for chipless and low cost identification tag in the thz frequency domain," in *2012 IEEE International Conference on RFID-Technologies and Applications (RFID-TA)*, Nov. 2012, pp. 24–28.

[50] E. Perret, M. Hamdi, G. E. P. Tourtollet, R. Nair, F. Garet, A. Delattre, A. Vena, L. Duvillaret, P. Martinez, S. Tedjini, and Y. Boutant, "Thid, the next step of chipless rfid," in *2013 IEEE International Conference on RFID (RFID)*, Apr. 2013, pp. 261–268.

[51] C.-L. Cheng and A. Zajić, "Characterization of propagation phenomena relevant for 300 ghz wireless data center links," *IEEE Transactions on Antennas and Propagation*, vol. 68, no. 2, pp. 1074–1087, Feb. 2020.

[52] C.-L. Cheng, S. Sangodoyin, and A. Zajić, "Thz mimo channel characterization for wireless data center-like environment," in *2019 IEEE International Symposium on Antennas and Propagation and USNC-URSI Radio Science Meeting*, Jul. 2019, pp. 2145–2146.

[53] C.-L. Cheng and A. Zajić, "Characterization of 300 ghz wireless channels for rack-to-rack communications in data centers," in *2018 IEEE 29th Annual International Symposium on Personal, Indoor, and Mobile Radio Communications (PIMRC)*, Sep. 2018.

[54] C.-L. Cheng, S. Kim, and A. Zajić, "Study of diffraction at 30 ghz, 140 ghz, and 300 ghz," in *2018 IEEE International Symposium on Antennas and Propagation USNC/URSI National Radio Science Meeting*, Jul. 2018, pp. 1553–1554.

[55] C.-L. Cheng, S. Sangodoyin, and A. Zajić, "Thz mimo fading analysis and doppler modeling in a data center environment," in *14th European Conference on Antennas and Propagation (EUCAP)*, Mar. 2020.

[56] ——, "Thz cluster-based modeling and propagation characterization in a data center environment," *IEEE Access*, (under revision).

[57] C.-L. Cheng, L. N. Nguyen, M. Prvulovic, and A. Zajić, "Exploiting switching of transistors in digital electronics for rfid tag design," *IEEE Journal of Radio Frequency Identification*, vol. 3, no. 2, pp. 67–76, Jun. 2019.

[58] ——, "Exploiting switching of transistors in digital electronics for rfid tag design," in *2018 IEEE International Conference on RFID (RFID)*, Apr. 2018.

[59] A. Zajić, *Mobile-to-Mobile Wireless Channels*. Norwood, MA, USA: Artech House, Inc., 2013, ISBN: 1608074951, 9781608074952.

[60] G. L. Stüber, *Principles of Mobile Communication (2nd ed.)* Norwell, MA, USA: Kluwer Academic Publishers, 2001, ISBN: 0-7923-7998-5.

[61] J. P. Rossi, "Influence of measurement conditions on the evaluation of some radio channel parameters," *IEEE Transactions on Vehicular Technology*, vol. 48, pp. 1304–1316, Jul. 1999.

[62] Y. Ai, M. Cheffena, and Q. Li, "Power delay profile analysis and modeling of industrial indoor channels," in *2015 9th European Conference on Antennas and Propagation (EuCAP)*, Apr. 2015, pp. 1–5.

[63] G. Chen, H. Chen, M. Haurylau, N. A. Nelson, D. H. Albonesi, P. M. Fauchet, and E. G. Friedman, "On-chip copper-based vs. optical interconnects: Delay uncertainty, latency, power, and bandwidth density comparative predictions," in *International Interconnect Technology Conference*, Jun. 2006, pp. 39–41.

[64] L. Popa, S. Ratnasamy, G. Iannaccone, A. Krishnamurthy, and I. Stoica, "A cost comparison of datacenter network architectures," in *Proceedings of the 6th International Conference*, ser. Co-NEXT '10, Philadelphia, Pennsylvania: ACM, 2010, 16:1–16:12, ISBN: 978-1-4503-0448-1.

[65] L. A. Barroso, J. Clidaras, and U. Höelzle, *The Datacenter as a Computer: An Introduction to the Design of Warehouse-Scale Machines, Second Edition*, 2nd. Morgan and Claypool Publishers, 2013, ISBN: 9781627050104.

[66] *Cisco unified computing system site planning guide: Data center power and cooling*, `https://www.cisco.com/c/en/us/solutions/collateral/data-center-virtualization/unified-computing/white_paper_c11-680202.pdf`, Cisco Systems, Inc., San Jose, CA, USA, 2017.

[67] J. M. Jornet and I. F. Akyildiz, "Channel modeling and capacity analysis for electromagnetic wireless nanonetworks in the terahertz band," *IEEE Transactions on Wireless Communications*, vol. 10, no. 10, pp. 3211–3221, Oct. 2011.

[68] H. Elayan, O. Amin, R. M. Shubair, and M. Alouini, "Terahertz communication: The opportunities of wireless technology beyond 5g," in *2018 International Conference on Advanced Communication Technologies and Networking (CommNet)*, Apr. 2018, pp. 1–5.

[69] B. Peng, S. Rey, D. M. Rose, S. Hahn, and T. Kürner, "Statistical characteristics study of human blockage effect in future indoor millimeter and sub-millimeter wave wireless communications," in *IEEE 87th Vehicular Technology Conference (VTC Spring)*, Jun. 2018, pp. 1–5.

[70] R. Piesiewicz, C. Jansen, D. Mittleman, T. Kleine-Ostmann, M. Koch, and T. Kürner, "Scattering analysis for the modeling of thz communication systems," *IEEE Transactions on Antennas and Propagation*, vol. 55, no. 11, pp. 3002–3009, Nov. 2007.

[71] C. Jansen, S. Priebe, C. Moller, M. Jacob, H. Dierke, M. Koch, and T. Kürner, "Diffuse scattering from rough surfaces in thz communication channels," *IEEE Transactions on Terahertz Science and Technology*, vol. 1, no. 2, pp. 462–472, Nov. 2011.

[72] A. Costanzo, S. Bartolini, L. Benini, E. Farella, D. Masotti, B. Milosevic, L. D. Stefano, A. Franchi, T. S. Cinotti, S. Mattarozzi, and V. Nannini, "Merging rfid, visual and gesture recognition technologies to generate and manage smart environments,"

in *2011 IEEE International Conference on RFID-Technologies and Applications*, Sep. 2011, pp. 521–526.

[73] L. Yang, A. Rida, R. Vyas, and M. M. Tentzeris, "Rfid tag and rf structures on a paper substrate using inkjet-printing technology," *IEEE Transactions on Microwave Theory and Techniques*, vol. 55, no. 12, pp. 2894–2901, Dec. 2007.

[74] S.-J. Wu and T.-G. Ma, "A passive uhf rfid meandered tag antenna with tuning stubs," in *2006 Asia-Pacific Microwave Conference*, Dec. 2006, pp. 1486–1492.

[75] S. Lemey, S. Agneessens, P. V. Torre, K. Baes, J. Vanfleteren, and H. Rogier, "Wearable flexible lightweight modular rfid tag with integrated energy harvester," *IEEE Transactions on Microwave Theory and Techniques*, vol. 64, no. 7, pp. 2304–2314, Jul. 2016.

[76] K. Finkenzeller, *RFID Handbook: Fundamentals and Applications In Contactless Smart Cards and Identification*, 3rd. Hobeken, NJ, USA: John Wiley and Sons, 2005, ISBN: 978-0-470-69506-7.

[77] A. Hasan, A. F. Peterson, and G. D. Durgin, "Reflected electro-material signatures for self-sensing passive rfid sensors," in *2011 IEEE International Conference on RFID*, Apr. 2011, pp. 62–69.

[78] F. Pebay-Peyroula, J. Reverdy, E. Crochon, and T. Thomas, "Very high data rate contactless air interface: An innovative solution for card to reader link," in *2010 IEEE International Conference on RFID (IEEE RFID 2010)*, Apr. 2010, pp. 203–209.

[79] N. Pillin, N. Joehl, C. Dehollain, and M. J. Declercq, "High data rate rfid tag/reader architecture using wireless voltage regulation," in *2008 IEEE International Conference on RFID*, Apr. 2008, pp. 141–149.

[80] J. Besnoff, M. Abbasi, and D. S. Ricketts, "High data-rate communication in near-field rfid and wireless power using higher order modulation," *IEEE Transactions on Microwave Theory and Techniques*, vol. 64, no. 2, pp. 401–413, Feb. 2016.

[81] S. Tedjini, N. Karmakar, E. Perret, A. Vena, R. Koswatta, and R. E-Azim, "Hold the chips: Chipless technology, an alternative technique for rfid," *IEEE Microwave Magazine*, vol. 14, no. 5, pp. 56–65, Jul. 2013.

[82] P. Chan and V. Fusco, "Bi-static 5.8ghz rfid range enhancement using retrodirective techniques," in *2011 41st European Microwave Conference*, Oct. 2011, pp. 976–979.

[83] W. G. Yeoh, Y. B. Choi, L. H. Guo, A. P. Popov, K. Y. Tham, B. Zhao, and X. Chen, "A 2.45-ghz rfid tag with on-chip antenna," in *IEEE Radio Frequency Integrated Circuits (RFIC) Symposium, 2006*, Jun. 2006, 4 pp.–.

[84] I. Vaisband and E. G. Friedman, "Stability of distributed power delivery systems with multiple parallel on-chip ldo regulators," *IEEE Transactions on Power Electronics*, vol. 31, no. 8, pp. 5625–5634, Aug. 2016.

[85] S. Preradovic and N. C. Karmakar, "Design of fully printable planar chipless rfid transponder with 35-bit data capacity," in *2009 European Microwave Conference (EuMC)*, Sep. 2009, pp. 013–016.

[86] M. Pöpperl, J. Adametz, and M. Vossiek, "Polarimetric radar barcode: A novel chipless rfid concept with high data capacity and ultimate tag robustness," *IEEE Transactions on Microwave Theory and Techniques*, vol. 64, no. 11, pp. 3686–3694, Nov. 2016.

[87] F. Amato, C. W. Peterson, M. B. Akbar, and G. D. Durgin, "Long range and low powered rfid tags with tunnel diode," in *2015 IEEE International Conference on RFID Technology and Applications (RFID-TA)*, Sep. 2015, pp. 182–187.

[88] F. Amato, H. M. Torun, and G. D. Durgin, "Rfid backscattering in long-range scenarios," *IEEE Transactions on Wireless Communications*, vol. 17, no. 4, pp. 2718–2725, Apr. 2018.

[89] *Custom transmitters*, `http://vadiodes.com/en/products/custom-transmitters`, Virginia Diodes, Inc., Charlottesville, VA, USA.

[90] *Phase Locked Dielectric Resonator Oscillators*, Ultra Electronics, Herley, Lancaster, PA, USA.

[91] *Frequency Multiplier - 33 to 50 GHz*, Norden Millimeter, Placerville, CA, USA.

[92] *Multipliers - VDI Model: WR6.5x3*, `https://www.vadiodes.com/en/frequency-multipliers/10-products/165-wr65x3`, Virginia Diodes, Inc., Charlottesville, VA, USA.

[93] *Mixers - VDI Model: WR2.8SHM*, `https://www.vadiodes.com/index.php/en/12-product/126-wr28shm12`, Virginia Diodes, Inc., Charlottesville, VA, USA.

[94] *Nominal Horn Specifications*, , Virginia Diodes, Inc., Charlottesville, VA, USA.

[95] *Plano-convex ptfe lens*, `https://www.thorlabs.com/thorproduct.cfm?partnumber=LAT075`, Thorlabs, Inc., Newton, NJ, USA.

[96] *1u, 2u, 3u, 4u, 5u, 6u, and 7u*, `https://www.computerhope.com/jargon/num/1u.htm`, Nov. 2018.

[97] S. J. Howard and K. Pahlavan, "Doppler spread measurements of indoor radio channel," *Electronics Letters*, vol. 26, no. 2, pp. 107–109, Jan. 1990.

[98] J. B. Andersen, J. O. Nielsen, G. F. Pedersen, G. Bauch, and G. Dietl, "Doppler spectrum from moving scatterers in a random environment," *IEEE Transactions on Wireless Communications*, vol. 8, no. 6, pp. 3270–3277, Jun. 2009.

[99] S. Thoen, L. Van der Perre, and M. Engels, "Modeling the channel time-variance for fixed wireless communications," *IEEE Communications Letters*, vol. 6, no. 8, pp. 331–333, Aug. 2002.

[100] A. Zajić, "Impact of moving scatterers on vehicle-to-vehicle narrow-band channel characteristics," *IEEE Transactions on Vehicular Technology*, vol. 63, no. 7, pp. 3094–3106, Sep. 2014.

[101] M. O. Al-Nuaimi and A. G. Siamarou, "Coherence bandwidth characterisation and estimation for indoor rician multipath wireless channels using measurements at 62.4ghz," *IEE Proceedings - Microwaves, Antennas and Propagation*, vol. 149, no. 3, pp. 181–187, Jun. 2002.

[102] R. Wang, B. Deng, Y. Qin, H. Wang, and X. Li, "Study of scattering characteristics for metallic spheres at terahertz frequencies," *Journal of Electromagnetic Waves and Applications*, vol. 28, no. 14, pp. 1786–1797, Jul. 2014.

[103] S. Bhardwaj, N. K. Nahar, and J. L. Volakis, "All electronic propagation loss measurement and link budget analysis for 350 ghz communication link," *Microwave and Optical Technology Letters*, vol. 59, no. 2, pp. 415–423, Feb. 2017.

[104] T. Jenserud and S. Ivansson, "Measurements and modeling of effects of out-of-plane reverberation on the power delay profile for underwater acoustic channels," *IEEE Journal of Oceanic Engineering*, vol. 40, no. 4, pp. 807–821, Oct. 2015.

[105] A. Abdi, J. A. Barger, and M. Kaveh, "A parametric model for the distribution of the angle of arrival and the associated correlation function and power spectrum at the mobile station," *IEEE Transactions on Vehicular Technology*, vol. 51, no. 3, pp. 425–434, May 2002.

[106] C.-L. Cheng, S. Sangodoyin, and A. Zajić, "Thz mimo channel characterization for wireless data center-like environment," in *2019 IEEE International Symposium on Antennas and Propagation USNC/URSI National Radio Science Meeting*, Jul. 2019.

[107] N. Czink, P. Cera, J. Salo, E. Bonek, J. Nuutinen, and J. Ylitalo, "A framework for automatic clustering of parametric mimo channel data including path powers," in *IEEE Vehicular Technology Conference*, Sep. 2006, pp. 1–5.

[108] M. Toeltsch, J. Laurila, K. Kalliola, A. F. Molisch, P. Vainikainen, and E. Bonek, "Statistical characterization of urban spatial radio channels," *IEEE Journal on Selected Areas in Communications*, vol. 20, no. 3, pp. 539–549, Apr. 2002.

[109] A. F. Molisch, J. R. Foerster, and M. Pendergrass, "Channel models for ultrawideband personal area networks," *IEEE Wireless Communications*, vol. 10, no. 6, pp. 14–21, Dec. 2003.

[110] J. Karedal, S. Wyne, P. Almers, F. Tufvesson, and A. F. Molisch, "A measurement-based statistical model for industrial ultra-wideband channels," *IEEE Transactions on Wireless Communications*, vol. 6, no. 8, pp. 3028–3037, Aug. 2007.

[111] S. M. Ross, *Simulation*. New York, NY, USA: Academic, 2013, ISBN: 9780124158252.

[112] S. Sangodoyin and A. F. Molisch, "Impact of body mass index on ultrawideband mimo ban channels-measurements and statistical model," *IEEE Transactions on Wireless Communications*, vol. 17, no. 9, pp. 6067–6081, Sep. 2018.

[113] *Rayleigh distribution*, `https://en.wikipedia.org/wiki/Rayleigh_distribution`, Wikipedia.

[114] *D flip flip cmos implementation*, `https://electronics.stackexchange.com/questions/245695/dual-edge-triggered-d-flip-flip-cmos-implementation-less-than-20-transistor`.

[115] J. M. Rabaey, A. Chandrakasan, and B. Nikolic, *Digital Integrated Circuits*, 3rd. Upper Saddle River, NJ, USA: Prentice Hall Press, 2008, ISBN: 0132219107, 9780132219105.

[116] P. V. Nikitin, K. V. S. Rao, and R. D. Martinez, "Differential rcs of rfid tag," *Electronics Letters*, vol. 43, no. 8, pp. 431–432, Apr. 2007.

[117] *22nm ptm low power model*, `http://ptm.asu.edu/latest.html`.

[118] W. Wolf, *FPGA-Based System Design*, ser. Prentice Hall Modern Semicondutor. Prentice Hall PTR, 2004, ISBN: 9780137033485.

[119] A. B. Sachid, P. Paliwal, S. Joshi, M. Shojaei, D. Sharma, and V. Rao, "Circuit optimization at 22nm technology node," in *2012 25th International Conference on VLSI Design*, Jan. 2012, pp. 322–327.

[120] S. Khademi, S. P. Chepuri, Z. Irahhauten, G. J. M. Janssen, and A. J. van der Veen, "Channel measurements and modeling for a 60 ghz wireless link within a metal cabinet," *IEEE Transactions on Wireless Communications*, vol. 14, no. 9, pp. 5098–5110, Sep. 2015.

[121] S. Kim and A. Zajić, "Characterization of 300-ghz wireless channel on a computer motherboard," *IEEE Transactions on Antennas and Propagation*, vol. 64, no. 12, pp. 5411–5423, Dec. 2016.

[122] A. Fricke, T. Kürner, M. Achir, and P. L. Bars, "A model for the reflection of terahertz signals from printed circuit board surfaces," in *2017 11th European Conference on Antennas and Propagation (EUCAP)*, Mar. 2017, pp. 711–715.

[123] D. Wu, M. J. Hussain, S. Li, and L. Lu, "R2: Over-the-air reprogramming on computational rfids," in *2016 IEEE International Conference on RFID (RFID)*, May 2016, pp. 1–8.

[124] D. D. Donno, L. Catarinucci, A. D. Serio, and L. Tarricone, "A long-range computational rfid tag for temperature and acceleration sensing applications," in *Progress In Electromagnetics Research C*, vol. 45, 2013, pp. 223–235.

[125] R. Colella, D. D. Donno, L. Tarricone, and L. Catarinucci, "Unconventional uhf rfid tags with sensing and computing capabilities," in *Journal of Communications Software and Systems*, vol. 10, 2014, pp. 83–89.

[126] T. Bjorninen, M. Lauri, L. Ukkonen, R. Ritala, A. Z. Elsherbeni, and L. Sydanheimo, "Wireless measurement of rfid ic impedance," *IEEE Transactions on Instrumentation and Measurement*, vol. 60, no. 9, pp. 3194–3206, Sep. 2011.

[127] M. S. Reynolds, "A 500 degrees celsius tolerant ultra-high temperature 2.4 ghz 32 bit chipless rfid tag with a mechanical bpsk modulator," in *2017 IEEE International Conference on RFID (RFID)*, May 2017, pp. 144–148.

[128] *Cyclone v device*, Data Sheet CV-51002, Altera Corporat., San Jose, CA, USA, Dec. 2016.

VITA

Chia-Lin Cheng grew up in Taipei, Taiwan, and received the B.Sc.degree from the School of Electrical Engineering, National Taiwan University, in 2013, and the M.Sc. degree from the School of Electrical and Computer Engineering, Georgia Institute of Technology, in 2017. Since 2016, he has been a Graduate Research Assistant with the Electromagnetic Measurements in Communications and Computing (EMC^2) Lab, and pursuing the Ph.D. degree in the School of Electrical and Computer Engineering, Georgia Institute of Technology. His research interests are in applied electromagnetics, RF design, and THz wireless communications. He received the TechConnect Innovation Award at the 2019 TechConnect World Innovation Conference and Expo, the Second Best Hardware Demo Award at the 2019 IEEE International Symposium on Hardware Oriented Security and Trust (HOST), and the Best Poster Award at the 2018 IEEE International Conference on RFID.